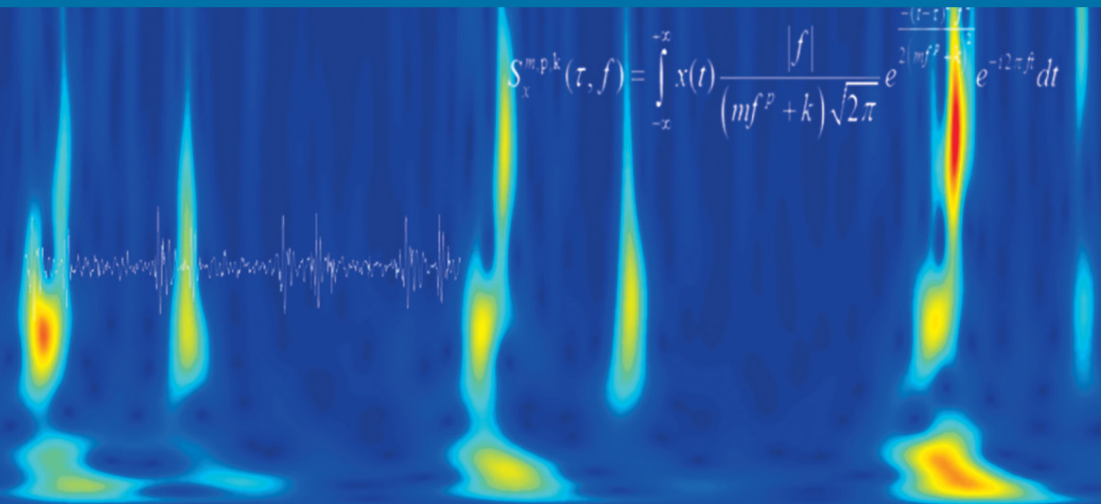


FOCUS
DIGITAL SIGNAL AND IMAGE PROCESSING SERIES



**Time–Frequency Domain for
Segmentation and Classification
of Non-stationary Signals**

*The Stockwell Transform
Applied on Bio-signals and Electric Signals*

**Ali Moukadem
Djaffar Ould Abdeslam and Alain Dieterlen**

ISTE

WILEY

Time–Frequency Domain for Segmentation and Classification of Non-stationary Signals

FOCUS SERIES

Series Editor Francis Castanié

**Time–Frequency Domain for
Segmentation and Classification
of Non-stationary Signals**

*The Stockwell Transform Applied on
Bio-signals and Electric Signals*

Ali Moukadem
Djaffar Ould Abdeslam
Alain Dieterlen

ISTE

WILEY

First published 2014 in Great Britain and the United States by ISTE Ltd and John Wiley & Sons, Inc.

Apart from any fair dealing for the purposes of research or private study, or criticism or review, as permitted under the Copyright, Designs and Patents Act 1988, this publication may only be reproduced, stored or transmitted, in any form or by any means, with the prior permission in writing of the publishers, or in the case of reprographic reproduction in accordance with the terms and licenses issued by the CLA. Enquiries concerning reproduction outside these terms should be sent to the publishers at the undermentioned address:

ISTE Ltd
27-37 St George's Road
London SW19 4EU
UK

www.iste.co.uk

John Wiley & Sons, Inc.
111 River Street
Hoboken, NJ 07030
USA

www.wiley.com

© ISTE Ltd 2014

The rights of Ali Moukadem, Djaffar Ould Abdeslam and Alain Dieterlen to be identified as the authors of this work have been asserted by them in accordance with the Copyright, Designs and Patents Act 1988.

Library of Congress Control Number: 2014930208

British Library Cataloguing-in-Publication Data
A CIP record for this book is available from the British Library
ISSN 2051-2481 (Print)
ISSN 2051-249X (Online)
ISBN 978-1-84821-613-6



Printed and bound in Great Britain by CPI Group (UK) Ltd., Croydon, Surrey CR0 4YY

Contents

Preface	ix
Chapter 1. The Need for Time–Frequency Analysis	1
1.1. Introduction	1
1.2. Stationary and non-stationary concepts	2
1.2.1. Stationarity	2
1.2.2. Non-stationarity	4
1.3. Temporal representations	5
1.4. Frequency representations of signals	6
1.4.1. Fourier transform	7
1.4.2. Mean frequency, bandwidth and frequency average	10
1.5. Uncertainty principle	12
1.6. Limitation of time analysis and frequency analysis: the need for time–frequency representation	15
1.6.1. Instantaneous frequency	15
1.7. Conclusion	18
1.8. Bibliography	19
Chapter 2. Time–Frequency Analysis: The S-Transform	21
2.1. Introduction	21
2.2. Synthetic signals	22
2.3. The STFT	22
2.4. The WT	24
2.5. The Wigner–Ville distribution	25
2.5.1. The pseudo-WVD	27
2.5.2. The smoothed PWVD	27
2.6. Cohen’s class	28
2.7. The S-transform	29

2.7.1. Properties of the S-transform	30
2.7.2. The discrete S-transform	38
2.7.3. The improvement of the S-transform energy concentration	41
2.7.4. The ST-spectrogram	51
2.8. Conclusion	56
2.9. Bibliography	56
Chapter 3. Segmentation and Classification of Heart Sounds Based on the S-Transform	61
3.1. Introduction	61
3.2. Methods and materials	64
3.2.1. Data sets	64
3.2.2. Localization and segmentation of heart sounds	65
3.2.3. Classification of heart sounds	70
3.3. Results and discussion	73
3.3.1. Localization and segmentation results	73
3.3.2. S1 and S2 classification results	77
3.3.3. Murmur detection results	80
3.4. Conclusion	82
3.5. Bibliography	83
Chapter 4. Adaline for the Detection of Electrical Events in Electrical Signals	87
4.1. Introduction	87
4.2. Electric events	88
4.2.1. Power quality	88
4.2.2. Electric events	89
4.3. Adaline	90
4.4. Adaline for frequency estimation	91
4.4.1. Adaline method	91
4.4.2. Results	94
4.5. Adaline for voltage component extraction in unbalanced system	97
4.5.1. Model of the unbalanced voltage system	98
4.5.2. Extraction of the voltage components in the DQ-space	99
4.5.3. Online estimation of the instantaneous phases θ_d and θ_i	100
4.5.4. Filtering the AC components in the DQ-space	101
4.5.5. Results	104
4.6. Adaline for harmonic current identification and compensation	108
4.6.1. Adaline method	110
4.6.2. Results	115
4.7. Conclusion	117
4.8. Bibliography	118

Chapter 5. FPGA Implementation of the Adaline	121
5.1. Introduction	121
5.2. Instantaneous power theory (IPT) in the APF	122
5.3. Adaline for the computing of the IPT in the PLL	123
5.3.1. Adaline-based PLL	123
5.3.2. A multiplexing approach for hardware consumption reduction	126
5.4. Results	129
5.4.1. Simulation	129
5.4.2. FPGA implementation results	130
5.5. Conclusion	132
5.6. Bibliography	133
Index	135

Preface

The idea behind this book has been to gather experience in signal processing by exploring time frequency tools combined with neuronal networks in order to optimize the analysis and classification process for non-stationary signals. Both abilities developed in the MIPS laboratory at the University of Haute Alsace at Mulhouse in France are not only original but they also open a wide range of applications.

Non-stationary signals are mostly to be found in nature; the relevant information is not easily described and predicted. The extraction, analysis and classification of such signals are made difficult by different types of noise. Due to the consequences of false results, the robustness of the tools in certain fields is vital.

Those principles that are related to signal feature extraction, representation and description using the Stockwell time–frequency (TF) transform and signal classification using adaptive linear neuron (Adaline) neuronal network have demonstrated their potential both in biomedical and power electric signals. The primary aim of this book is to present original methods and algorithms in order to be able to extract information from non-stationary signals such as the heart sounds and power quality signals. The proposed methods focus on the TF domain and most notably on the Stockwell transform for the feature extraction process and the identification of signatures. For the classification method, the Adaline neural network is used and compared with other classic classifiers for electrical signals. Theory enhancement, original applications and the introduction of implementation on field programmable gate array (FPGA) for real-time processing are introduced in this book.

The book consists of five chapters. Chapter 1 (The Need for Time–Frequency Analysis) introduces the prerequisites for TF analysis methods and most notably for non-stationary signals where statistical properties vary over time. The chapter

presents the stationary and non-stationary concepts and the different domains of signal representation. The limitations of time and frequency representations and the need for joint TF representations are also introduced and discussed.

After a brief presentation of some linear and bilinear TF methods, Chapter 2 (Time–Frequency Analysis: the S-Transform) explores the Stockwell transform in detail, which is a linear TF method. Mathematical properties and theoretical characteristics are discussed and new algorithms and measures for energy concentration enhancement and complexity measures in the TF domain are also discussed and compared.

Chapter 3 (Segmentation and Classification of Heart Sounds Based on the S-Transform) presents the first application of this book, which is a heart sound signal processing module. Proposing an objective signal processing method, which is able to extract relevant information from biosignals, is a great challenge in the telemedicine and auto-diagnosis fields. Heart sounds that reveal the mechanical activity of the heart are considered non-stationary signals. Original segmentation and classification methods and algorithms based on the Stockwell transform are presented and validated on real signals collected in real-life conditions.

Chapter 4 (Adaline for the Detection of Electrical Events in Electrical Signals) presents the second application of this book, which is the identification of an event in electrical signals such as current harmonics and voltage unbalance. Several original methods that aim at detecting events based on the Adaline neural network are proposed and compared in this chapter.

Chapter 5 (FPGA Implementation of Adaline) presents an implementation methodology of Adaline on FPGA. A novel multiplexing technique and architecture applied to a neural harmonics extraction method are shown and discussed in this chapter.

The advanced signal processing tools and techniques presented in this book and the originality of the authors' contributions can be very useful for those involved in engineering and research in the field of signal processing.

Since this is the first edition of the book, the authors are aware of the inevitable errors and ambiguities that might be present in this edition. Therefore, all comments and suggestions will be welcome to enhance the clarity and improve the scientific quality of the next editions.

Finally, the authors are most grateful to Dr. C. Brandt, from the Centre Hospitalier Universitaire at Strasbourg and doctor in cardiology specialized in PCG analysis, for his indispensable expertise in validating the tools developed for heart

sound segmentation and classification (see Chapter 3). Many thanks also go to Dr. S. Schmidt, from the Department of Health Science and Technology at Aalborg University, for providing a heart sound database of subjects under cardiac stress tests. The authors would also like to thank C. Bach, professor of English, for his availability and reviewing help.

Ali MOUKADEM
Djaffar OULD ABDESLAM
Alain DIETERLEN
January 2014

The Need for Time–Frequency Analysis

Most real signals are non-stationary where the frequency can vary with time. The classic Fourier transform analyzes the frequency content of the signal without any time information. It emphasizes the importance of time–frequency transforms designed to detect the frequency changes of the signal over time. Moreover, it allows extracting relevant features to classify signal signatures. This chapter presents the stationary and non-stationary concepts and the representations of the signal in time or frequency domains. The limitations of these representations and the need of the time–frequency domain are also introduced and discussed.

1.1. Introduction

From a theoretical point of view, signals can be divided into two main groups: deterministic and random. Deterministic signals are well known mathematically (analytically describable), so the future values of the signal can be calculated from the past values with complete certainty. However, random signals cannot be described as a mathematical expression and cannot be predicted with a total certainty, which leads to the study of their statistical properties (average, variance, covariance, etc.) in order to have an idea about their structure.

In a deterministic or random framework, a signal as an abstraction of physical quantities of a process can be classified intuitively into two main classes: stationary and non-stationary signals. This qualitative classification is based mainly on information variation of a signal over time. In the case of random signals, for example, the stationary signals have constant statistical properties over time while non-stationary signals are characterized by the variation of their statistical properties during the interval of observation. In a deterministic framework, stationary signals can be defined as a sum of discrete sinusoids that have an invariant frequency over time, otherwise they are considered as non-stationary.

Most real-life signals are non-stationary and contain random components that can be caused by the measurement instruments (random noise, spike, etc.) and/or by the nature of the physical process under study. For example, in the acquisition of the heart sound signal, which is a non-stationary signal by nature, several factors affect the quality of the acquired signal: the type of electronic stethoscope, the patient's position during auscultation and the surrounding noises. Moreover, the heart sound as an abstraction of the mechanical activity of the heart contains by nature random components such as murmurs. Another example is the power quality signals and their disturbances that have negative impacts on power systems and make the electric signal random and non-stationary. These two examples of non-stationary signals will be the main applications in this book (Chapters 3 and 4).

The aim of this chapter is to present the stationary and non-stationary concepts briefly. The different signal representations will be introduced and the limitations of time or frequency representations in the case of non-stationary signals will be shown. This will lead us to introduce some essential concepts such as the uncertainty principle and the instantaneous frequency (IF) measure.

1.2. Stationary and non-stationary concepts

1.2.1. *Stationarity*

1.2.1.1. *Deterministic signal*

A deterministic signal is said to be stationary if it can be written as a sum of sinusoidal components [AUG 05]. In other words, the signal is stationary if it has a constant instantaneous amplitude and frequency over time. Let us consider a deterministic signal $x(t)$ that can be written as:

$$x(t) = \sum_k A_k \cos(2\pi f_k t + \varphi_k) \quad [1.1]$$

where A_k , f_k and φ_k are real constant¹ coefficients that correspond to the amplitude, frequency and phase of $x(t)$, respectively.

EXAMPLE 1.1.– Consider an example of a multicomponent sinusoidal signal:

$$x(t) = \sin(2\pi f_1 t) + 0.7 \sin(2\pi f_2 t)$$

where $f_1 = 10$ Hz and $f_2 = 20$ Hz.

¹ If one of these coefficients is random, then the signal becomes random.

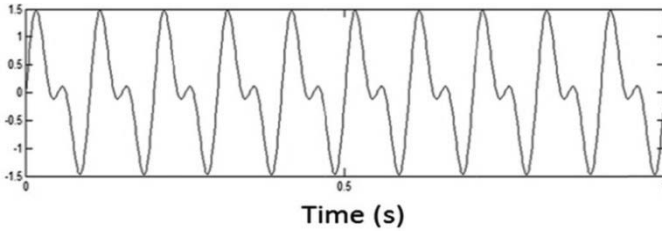


Figure 1.1. Example of deterministic signal: sum of two sinusoidal signals

It is clear that it is possible to know the future values of the signal from the past values with complete certainty since its mathematical equation is well known.

1.2.1.2. Random (stochastic) signal

A stochastic signal $x(t)$ is said to be stationary if its expectation is independent of time and its autocorrelation function $E[x(t_1)x^*(t_2)]$ depends only on the time difference $t_2 - t_1$:

$$\forall t, T : E[x(t)] = E[x(t+T)] = m_x \quad [1.2]$$

where m_x is a constant,

and

$$\forall t_1, t_2, T : E[x(t_1)x^*(t_2)] = E[x(t_1+T)x^*(t_2+T)] \quad [1.3]$$

EXAMPLE 1.2.– An example of a stationary random signal is white Gaussian noise (Figure 1.2).

In this case, we cannot describe the signal using an analytical equation. However, the signal can be characterized by a probability density function (pdf), which is a normal (Gaussian) distribution in this example (see Figure 1.3).

On the other hand, the signal is said to be stationary because its statistical properties are unchanged during the time of observation.

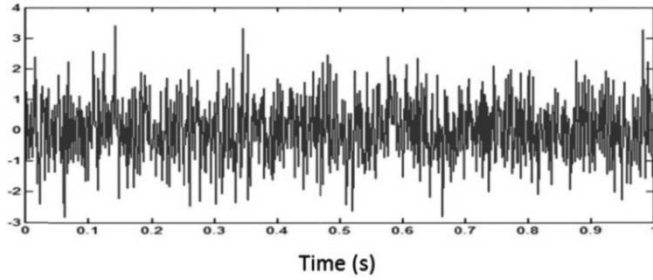


Figure 1.2. Example of stationary random signal:
white Gaussian noise

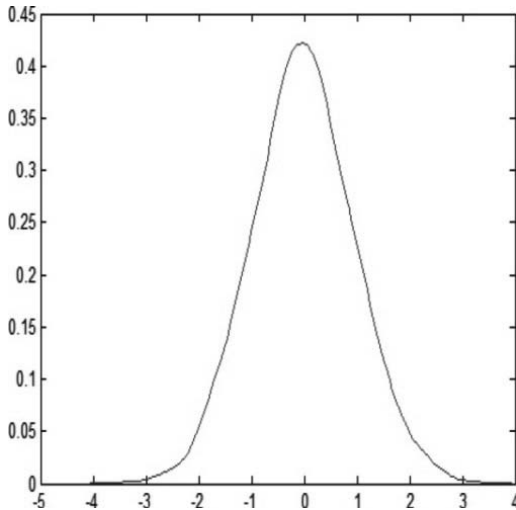


Figure 1.3. The pdf estimated from the signal in Figure 1.2

1.2.2. Non-stationarity

Non-stationarity as a “non-property” is validated if the assumptions of stationarity are no longer valid [AUG 05]. In other words, a signal is considered to be non-stationary if its frequency and statistical properties vary during the time of observation. A linear chirp and a multitone sine wave (Example 1.3) are familiar synthetic examples of non-stationary signals. Otherwise, most real signals such as human speech and biomedical signals are non-stationary.

EXAMPLE 1.3.– Let us consider a multicomponent sinusoidal signal composed of four components. Let the signal be composed of one component with frequency

$f_1 = 10$ Hz in the first interval, two components with frequency f_1 and $f_2 = 50$ Hz in the second interval, three components with frequency f_1 , f_2 and $f_3 = 100$ Hz in the third interval and finally one component with frequency $f_4 = 20$ Hz in the last interval. The signal $x(t)$ described above can mathematically be given as:

$$\begin{cases} x(t) = \cos(2\pi f_1 t) & 0 \leq t \leq 200 \text{ ms} \\ x(t) = \cos(2\pi f_1 t) + \cos(2\pi f_2 t) & 200 \leq t \leq 400 \text{ ms} \\ x(t) = \cos(2\pi f_1 t) + \cos(2\pi f_2 t) + \cos(2\pi f_3 t) & 400 \leq t \leq 600 \text{ ms} \\ x(t) = \cos(2\pi f_4 t) & 600 \leq t \leq 800 \text{ ms} \end{cases}$$

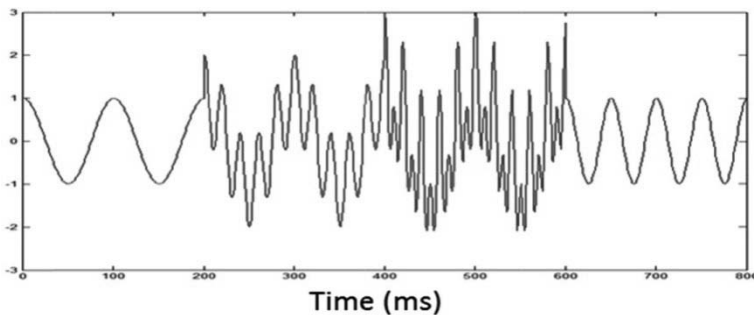


Figure 1.4. Non-stationary sinusoidal signal composed of frequencies 10, 20, 50 and 100 Hz

Unlike Example 1.1, such a signal (Figure 1.4) can be considered as non-stationary since its frequency varies over time.

1.3. Temporal representations

Signals can be represented in many different ways. The temporal representations of signals are the most natural representation that gives information about the instance durations and the energy of the different components. The duration of the first and the second heart sounds, for example, (see Example 1.4) can be an accurate feature to distinguish between some pathological cases and normal cases. Also the energy of murmurs can be an indicator of the severity of the pathology. Another example is the duration and energy of disturbances in electrical signals, which gives an idea of the nature of disturbance and the quality of the electrical

network. Many real signals are produced by a time-varying process: heart sounds, electrical signals, speech signals, electromagnetic fields, etc.

The total energy of a signal defined by how much energy the signal has or how much energy it takes to be produced [COH 95] is obtained by integrating the instantaneous power $|x(t)|^2$ as follows:

$$E_x = \int_{-\infty}^{+\infty} |x(t)|^2 dt \quad [1.4]$$

The two other features that can be calculated based on time domain are the first- and second-order moments. Respectively, they reveal the average time instant where the energy of the signal is localized and the dispersion of the signal around which this time is constituted [AUG 08]. If we consider that $|x(t)|^2$ is a density in time, the first moment or the average time of the signal $x(t)$ can be given as:

$$t_x = \frac{1}{E_x} \int_{-\infty}^{+\infty} t |x(t)|^2 dt \quad [1.5]$$

and the second-order moment (time spreading) can be given as:

$$\begin{aligned} (\Delta t_x)^2 &= \frac{1}{E_x} \int_{-\infty}^{+\infty} (t - t_x)^2 |x(t)|^2 dt \\ &= \frac{1}{E_x} \int_{-\infty}^{+\infty} t^2 |x(t)|^2 dt - t_x^2 \end{aligned} \quad [1.6]$$

where the standard deviation is:

$$\Delta t_x = \sqrt{\frac{1}{E_x} \int_{-\infty}^{+\infty} (t - t_x)^2 |x(t)|^2 dt} \quad [1.7]$$

1.4. Frequency representations of signals

Another domain for the representation of signals is the frequency domain. It gives an idea of the repetition of an event in the signal that is not accessible in the time domain. The concept of frequency is based on the sinusoidal waves. The

essential mathematical analysis tool of the frequency domain is the Fourier transform.

1.4.1. Fourier transform

The objective of this transform is to change the basis of the signal into sinusoidal basis vectors. The Fourier transform $X(f)$ of signal $x(t)$ is given as:

$$X(f) = \int_{-\infty}^{+\infty} x(t) e^{-j2\pi ft} dt \quad [1.8]$$

The inverse Fourier transform is given as:

$$x(t) = \frac{1}{2\pi} \int_{-\infty}^{+\infty} X(f) e^{j2\pi ft} df \quad [1.9]$$

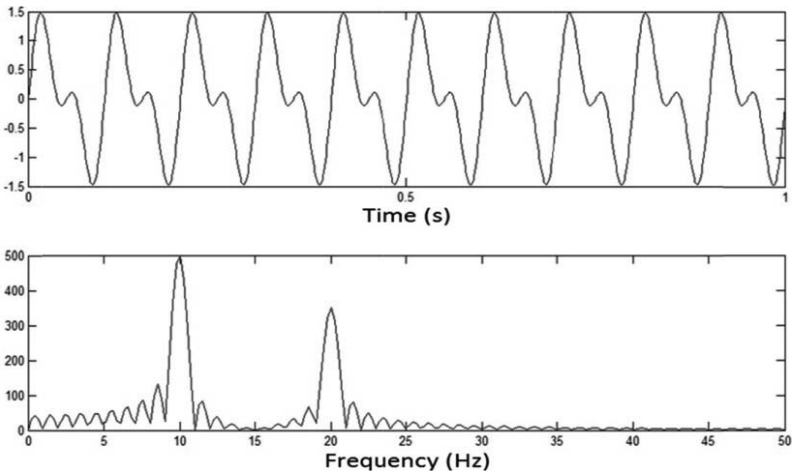


Figure 1.5. Multicomponent signal with a) temporal representation and b) frequency representation

The Fourier transform is a complex transform where its amplitude is called the magnitude spectrum, its phase is known as the phase spectrum and the square of the magnitude is the energy spectral density, which describes how the energy of the

signal is distributed over frequencies. Thus, the total signal energy is obtained by integrating the energy spectral density $|X(f)|^2$ over frequency:

$$E_x = \int_{-\infty}^{+\infty} |X(f)|^2 df \quad [1.10]$$

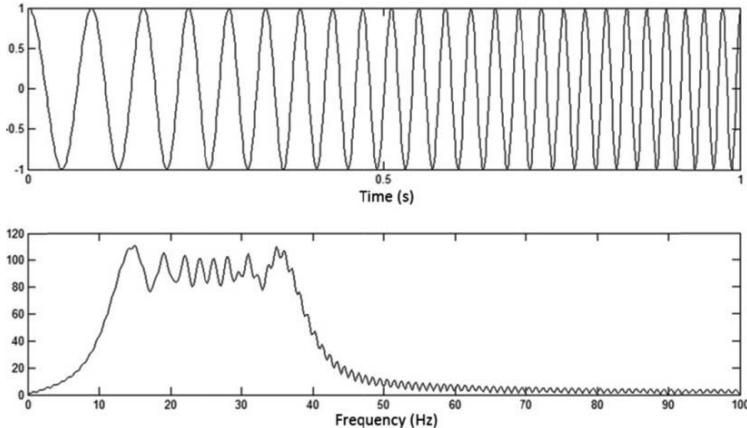


Figure 1.6. Chirp signal in a) temporal domain and
b) frequency domain

Some of the mathematical properties of the Fourier transform are described as follows:

– *Linearity*

The Fourier transform of a linear combination of signals is equal to the linear combination of their Fourier transforms:

$$TF\{\alpha x(t) + \beta y(t)\} = \alpha TF\{x(t)\} + \beta TF\{y(t)\} \quad [1.11]$$

$$\begin{aligned} \int_{-\infty}^{+\infty} (\alpha x(t) + \beta y(t)) e^{-j2\pi f t} dt &= \alpha \int_{-\infty}^{+\infty} x(t) e^{-j2\pi f t} dt + \beta \int_{-\infty}^{+\infty} y(t) e^{-j2\pi f t} dt \\ &= \alpha X(f) + \beta Y(f) \end{aligned}$$

– *Time shift*

Shifting the signal $x(t)$ by t_0 in the time domain results in multiplying the Fourier transform with a phase factor:

$$\int_{-\infty}^{+\infty} x(t - t_0) e^{-j2\pi ft} dt = X(f) e^{-j2\pi f t_0} \quad [1.12]$$

– *Frequency shift*

Modulating the signal with a complex exponential function shifts the Fourier transform $X(f)$ along the frequency axis:

$$\int_{-\infty}^{+\infty} (x(t) e^{j2\pi f_0 t}) e^{-j2\pi f t} dt = \int_{-\infty}^{+\infty} x(t) e^{j2\pi (f_0 - f)t} dt = X(f - f_0) \quad [1.13]$$

– *Convolution*

The Fourier transform of convolution of two functions $x(t)$ and $y(t)$ is equal to the product of the Fourier transforms of the individual signals:

$$TF\{x(t) * y(t)\} = X(f)Y(f) \quad [1.14]$$

On the other hand, the Fourier transform of the product of two signals equals the convolution of their Fourier transforms:

$$TF\{x(t).y(t)\} = X(f)*Y(f) \quad [1.15]$$

– *Derivation*

The Fourier transform of the derivative of function $x(t)$ is equal to the product of the Fourier transform $X(f)$ by $2j\pi f$:

$$TF\{x'(t)\} = 2j\pi f X(f) \quad [1.16]$$

– Parseval’s theorem

The total energy calculated from the energy spectral density should be equal to the total energy calculated directly from the time domain signal (instantaneous power energy):

$$E_x = \int_{-\infty}^{+\infty} |x(t)|^2 dt = \int_{-\infty}^{+\infty} |X(f)|^2 df \quad [1.17]$$

PROOF.–

$$\begin{aligned} \int_{-\infty}^{+\infty} |X(f)|^2 df &= \int_{-\infty}^{+\infty} X(f) X(f)^* df \\ &= \int_{-\infty}^{+\infty} \left\{ \int_{-\infty}^{+\infty} x(t) e^{-j2\pi f t} dt \right\} \cdot \left\{ \int_{-\infty}^{+\infty} x^*(u) e^{j2\pi f u} du \right\} df = \iiint_{\infty} x(t) x^*(u) e^{j2\pi f(u-t)} dudfdt \\ &= \iint_{\infty} x(t) x^*(u) \delta(t-u) dudt \\ &= \int_{-\infty}^{+\infty} x(t) x^*(t) dt \end{aligned}$$

where:

$$\int_{-\infty}^{+\infty} e^{2\pi f(u-t)} df = \delta(t-u)$$

1.4.2. Mean frequency, bandwidth and frequency average

As for the time domain, a signal can be characterized by its average frequency and the frequency band that it occupies. The average frequency can be given as:

$$f_x = \frac{1}{E_x} \int_{-\infty}^{+\infty} f |X(f)|^2 df \quad [1.18]$$

and the frequency band or the frequency spreading as:

$$\begin{aligned} (\Delta f_x)^2 &= \frac{1}{E_x} \int_{-\infty}^{+\infty} (f - f_x)^2 |X(f)|^2 df \\ &= \frac{1}{E_x} \int_{-\infty}^{+\infty} f^2 |X(f)|^2 df - f_x^2 \end{aligned}$$

Then:

[1.19]

$$\Delta f_x = \sqrt{\frac{1}{E_x} \int_{-\infty}^{+\infty} (f - f_x)^2 |X(f)|^2 df}$$

To calculate the average of frequency of signal $x(t)$ without calculating the Fourier transform $X(f)$, we can use the equality [COH 95]:

$$\begin{aligned} f_x &= \frac{1}{E_x} \int_{-\infty}^{+\infty} f |X(f)|^2 df \\ &= \frac{1}{E_x} \int_{-\infty}^{+\infty} x^*(t) \frac{1}{j} x'(t) dt \end{aligned} \quad [1.20]$$

PROOF.—

$$\begin{aligned} f_x &= \frac{1}{E_x} \iiint_{\infty} f x^*(t) x(u) e^{j2\pi(t-u)f} df du dt \\ &= \frac{1}{E_x 2\pi j} \iiint_{\infty} x^*(t) x(u) \frac{\partial}{\partial t} e^{j2\pi(t-u)f} df du dt \\ &= \frac{1}{E_x j} \iint_{\infty} x^*(t) \frac{\partial}{\partial t} \delta(t-u) x(u) du dt \\ &= \frac{1}{E_x} \int_{-\infty}^{+\infty} x^*(t) \frac{1}{j} \frac{\partial}{\partial t} x(t) dt \\ &= \frac{1}{E_x} \int_{-\infty}^{+\infty} x^*(t) \frac{1}{j} x'(t) dt \end{aligned}$$

EXAMPLE 1.4.— For the Gaussian signal $x(t)$:

$$x(t) = e^{-\alpha^2 t^2}$$

The average localization in time and frequency is given as:

$$\Delta t_x = \frac{1}{\alpha}$$

and

$$\Delta f_x = \frac{\alpha}{2\pi}$$

In addition the inequality related to the uncertainty principle can be calculated as (section 1.5, also see Figure 1.7):

$$\Delta t_x \cdot \Delta f_x = \frac{1}{4\pi}$$

The inequality becomes equality in the case of Gaussian signals. It can be shown that the Gaussian signal is the only signal for which the equality holds [GAB 46].

1.5. Uncertainty principle

The uncertainty principle in signal processing shows that a narrow waveform yields a wide spectrum and a wide waveform yields a narrow spectrum and both the time waveform and frequency spectrum cannot be made arbitrarily small simultaneously [GRÖ 01]. In other words, the more a signal is localized in time, the less it is in frequency and vice versa (see Figure 1.7). When talking about the uncertainty principle in signal processing, several elements have to be taken into consideration: the signal concerned $x(t)$ and its spectrum $X(f)$, the density in time $|x(t)|^2$, the density in frequency $|X(f)|^2$ and the standard deviations of time and frequency, Δt_x and Δf_x , respectively. The uncertainty principle is given by the inequality [1.21]:

$$\Delta t_x \cdot \Delta f_x \geq \frac{1}{4\pi} \quad [1.21]$$

PROOF.– If we take a signal with a zero mean time and a zero mean frequency (so $t_x = 0$ and $f_x = 0$), this does not affect the generality because the standard

deviation of the dispersion around these means is independent of their values. So in this case, by using equation [1.5]:

$$\Delta t_x = \frac{1}{\sqrt{E_x}} \int_{-\infty}^{+\infty} |t x(t)| dt$$

Then:

$$(\Delta t_x)^2 = \frac{1}{E_x} \int_{-\infty}^{+\infty} |t x(t)|^2 dt$$

and (by using equation [1.19]):

$$\Delta f_x = \frac{1}{\sqrt{E_x}} \int_{-\infty}^{+\infty} |f X(f)| df$$

Then:

$$(\Delta f_x)^2 = \frac{1}{E_x} \int_{-\infty}^{+\infty} |f X(f)|^2 df$$

Moreover, by using integration by parts, we obtain:

$$\int_{-\infty}^{+\infty} x^2(t) dt = -2 \int_{-\infty}^{+\infty} t x(t) x'(t) dt$$

$$\left| \int_{-\infty}^{+\infty} x(t)^2 dt \right| = 2 \int_{-\infty}^{+\infty} |t x(t) x'(t)| dt$$

The Cauchy–Schwarz inequality (which is a special case of Hölder’s inequality) for two functions $f(x)$ and $g(x)$ is given as follows:

$$\int_{-\infty}^{+\infty} |f(x) g^*(x)| dx \leq \left(\int_{-\infty}^{+\infty} |f(x)|^2 dx \right)^{\frac{1}{2}} \cdot \left(\int_{-\infty}^{+\infty} |g(x)|^2 dx \right)^{\frac{1}{2}}$$

Let $f(t) = tx(t)$ and $g(t) = x'(t)$, we obtain:

$$\int_{-\infty}^{+\infty} |x(t)|^2 dt \leq 2 \left(\int_{-\infty}^{+\infty} |tx(t)|^2 dt \right)^{\frac{1}{2}} \cdot \left(\int_{-\infty}^{+\infty} |x'(t)|^2 dt \right)^{\frac{1}{2}}$$

$$E_x \leq 2\sqrt{E_x} \Delta t_x \cdot \left(\int_{-\infty}^{+\infty} |x'(t)|^2 dt \right)^{\frac{1}{2}}$$

To evaluate the term $\left(\int_{-\infty}^{+\infty} |x'(t)|^2 dt \right)^{\frac{1}{2}}$:

$$\int_{-\infty}^{+\infty} |x'(t)|^2 dt = \iint_{\infty} |x'(t)(x'(t))^*| dt$$

By using equation [1.16]:

$$\begin{aligned} \int_{-\infty}^{+\infty} |x'(t)|^2 dt &= (2j\pi)^2 \iiint_{\infty} fX(f) \omega X^*(\omega) e^{j2\pi(f-\omega)t} d\omega df dt \\ &= (2j\pi)^2 \iint_{\infty} fX(f) \omega X^*(\omega) \delta(f-\omega) d\omega df \\ &= |2j\pi|^2 \int_{-\infty}^{+\infty} |fX(f)|^2 df \\ &= |2j\pi|^2 E_x (\Delta f_x)^2 \end{aligned}$$

and

$$\left(\int_{-\infty}^{+\infty} |x'(t)|^2 dt \right)^{\frac{1}{2}} = 2\pi\sqrt{E_x} \Delta f_x$$

The inequality becomes:

$$E_x \leq 4\pi \Delta t_x E_x \Delta f_x$$

$$\text{So finally: } \Delta t_x \Delta f_x \geq \frac{1}{4\pi}$$

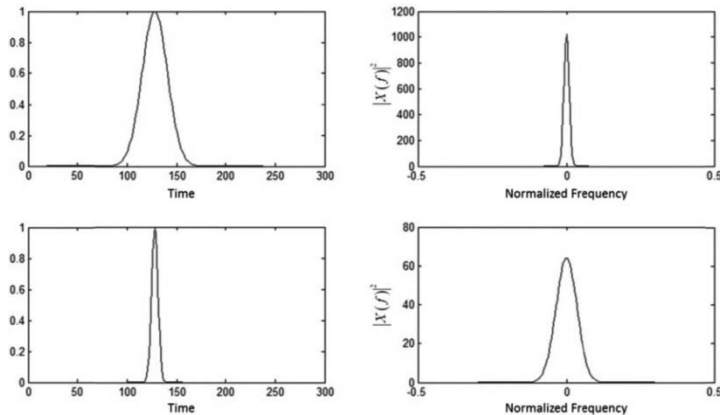


Figure 1.7. Two different Gaussian signals in the time domain (left) and the frequency domain (right): wide waveforms yield a narrow spectrum and narrow waveforms yield a wide spectrum

1.6. Limitation of time analysis and frequency analysis: the need for time–frequency representation

Figure 1.8 shows an example of two different chirp signals with the same frequency density content. The Fourier transform integrates the frequency component over time, so the final result will not contain any information about the time localization of the signal. This is a serious limitation in the case of non-stationary signals where following the frequency changes over time become crucial.

A first intuitive solution is to track the frequency instantaneously. This will be presented by the IF concept in the following section.

1.6.1. Instantaneous frequency

IF is one of the basic signal descriptors, which provides information about the time-varying spectral changes in non-stationary signals. It can be viewed as the first and most simple solution to deal with the limitations of time or frequency representations. To calculate the IF, we have to define the analytic signal, which is a more advanced illustration of the real signal. The analytic signal gives an idea about amplitude and phase. It can be given as:

$$x_a(t) = A_x e^{j\varphi(t)} \quad [1.22]$$

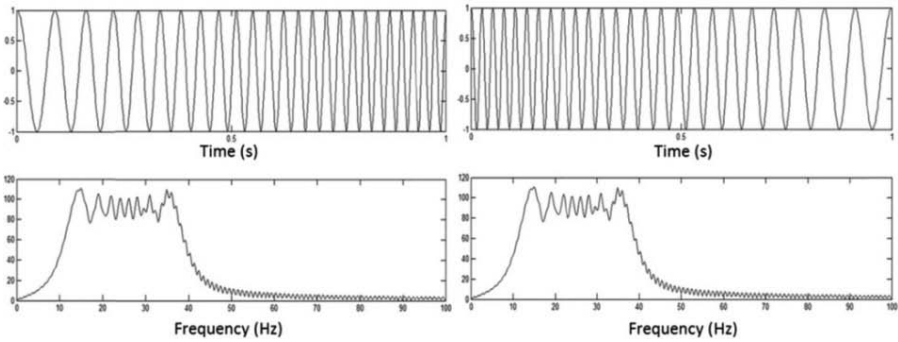


Figure 1.8. Showing two different signals with the same spectral content

The complex value associated with the real value can be calculated using the Hilbert transform:

$$x_a(t) = x(t) + jH\{x(t)\} \quad [1.23]$$

where $H\{x(t)\}$ is the Hilbert transform of signal $x(t)$, which can be calculated as follows:

$$H[x(t)] = x(t) * \frac{1}{\pi t} = \frac{1}{\pi} \int_{-\infty}^{+\infty} \frac{x(\tau)}{\tau - t} d\tau \quad [1.24]$$

The Hilbert transform of $x(t)$ can be viewed as a convolution of $x(t)$ with the signal $\frac{1}{\pi t}$. It is the response to $x(t)$ of a linear time-invariant filter having impulse response $\frac{1}{\pi t}$.

Ville [VIL 48] defined the IF $f(t)$ of real signal $x(t)$ as the derivation of phase of its analytic signal $x_a(t)$:

$$f(t) = \frac{1}{2\pi} \frac{\partial}{\partial t} \varphi(t) \quad [1.25]$$

and the instantaneous amplitude as:

$$A_x(t) = \sqrt{x(t)^2 + H[x(t)]^2} \quad [1.26]$$

From a spectral point of view, the relationship between the analytic signal and the real signal is given as follows:

$$\begin{cases} X_a(f) = 0 & \text{if } f < 0 \\ X_a(f) = X(f) & \text{if } f = 0 \\ X_a(f) = 2X(f) & \text{if } f > 0 \end{cases}$$

where $X_a(f)$ is the spectrum of the analytic signal and $X(f)$ is the spectrum of real signal.

The negative frequencies are suppressed in the analytic signal. This does not alter the information content of the signal since we have:

$$X(-f) = X^*(f) \quad [1.27]$$

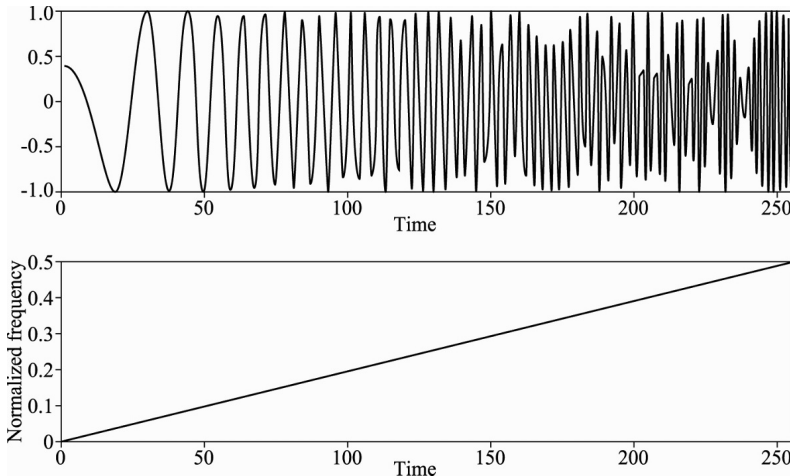


Figure 1.9. a) Linear chirp in time domain and
b) the estimation of its instantaneous frequency

An example of the IF estimation is shown in Figure 1.9. The major problem with the IF estimation occurs with a multicomponent non-stationary signal where the

local spectrum is averaged. This is considered as a serious limitation of IF especially if we want to extract relevant features from each component signature (see Figure 1.10). Hence, a higher dimension is needed to represent the signal more accurately. This can be done by a joint time–frequency representation, which will be the main subject of Chapter 2

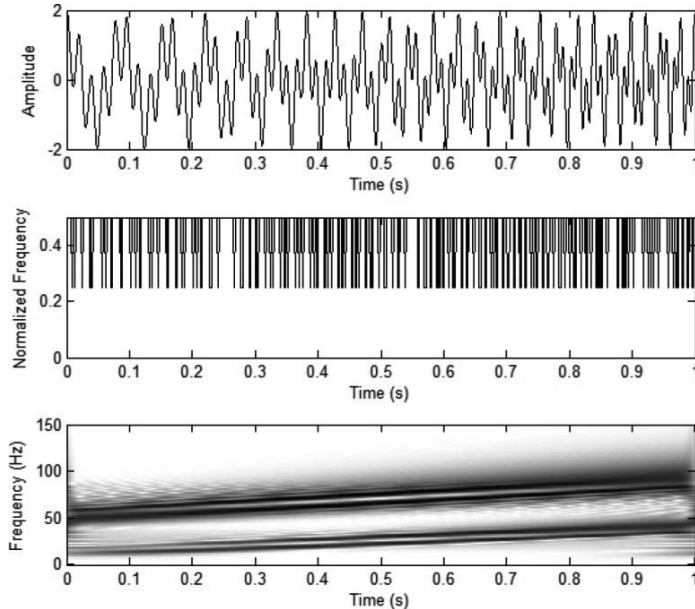


Figure 1.10. Sum of two linear chirps a), the IF b) and the joint time–frequency (the Stockwell transform) representation c)

1.7. Conclusion

In this chapter, some concepts of signal theory, such as the stationary and non-stationary processes, have been presented: first, the representation of signals in time or frequency domains, and second, the related mathematical concepts and proofs.

The main objective of this chapter was to show the limitation of time or frequency representation, most notably in the case of multicomponent and non-stationary signals. The need of time–frequency representation is proved by showing the limitations of instantaneous frequency measure. This can be considered as a primary introduction to Chapter 2, which concerns the time–frequency analysis by using the Stockwell transform [STO 96].

1.8. Bibliography

- [AHL 08] AHLSTROM C., Non linear phonocardiographic signal processing, PhD Thesis, Linköping University, Sweden, April 2008.
- [AUG 05] AUGER F., FLANDRIN P., GONÇALVÈS P., *et al.*, *Time-Frequency Toolbox*, Tutorial, CNRS (France) and Rice University (USA), 26 October 2005.
- [AUG 08] AUGER F., CHASSANDE-MOTTIN E., “Quadratic time-frequency analysis I: Cohen’s class”, in HLAWATSCH F., AUGER F. (ed.), *Time-Frequency Analysis*, Chapter 5, ISTE, London, John Wiley & Sons, New York, pp. 131–136, 2008.
- [BOA 92] BOASHASH B., “Estimating and interpreting the instantaneous frequency of a signal – part 1: fundamentals”, *Proceedings of the IEEE*, vol. 80, no. 4, pp. 540–568, April 1992.
- [GAB 46] GABOR D., “Theory of communication”, *Journal of Institute of Electrical Engineers*, vol. 93, pp. 429–457, November 1946.
- [GRÖ 01] GRÖCHENIG K., *Foundations of Time-Frequency Analysis*, Birkhäuser, Boston, MA, 2001.
- [STO 96] STOCKWELL R.G., MANSINHA L., LOWE R.P., “Localization of the complex spectrum: the S-transform”, *IEEE Transactions on Signal Processing*, vol. 44, no. 4, pp. 998–1001, 1996.
- [VIL 48] VILLE J., “Théorie et applications de la notion de signal analytique”, *Câbles et Transmissions*, vol. 2A, no. 1, pp. 61–74, 1948. [In French]. English translation: SELIN I., “Theory and applications of the notion of complex signal”, Rand Corporation Report T-92, Santa Monica, CA, August 1958.

Time–Frequency Analysis: The S-Transform

In Chapter 1, the need for time–frequency (TF) representations was shown, most notably in the case of non-stationary signals. This chapter aims at representing some TF methods briefly, together with their strengths and drawbacks. Therefore, the Stockwell transform (ST) will be presented in detail. It is a hybrid method between the short-time Fourier transform (STFT) and the wavelet transform (WT). Some algorithms related to the enhancement of the energy concentration in the TF plane generated by the S-transform will be presented. Then, we will study some mathematical properties of the ST-spectrogram and propose complexity measures based on the TF coefficients.

2.1. Introduction

TF analysis is a powerful tool to describe signals both in the time domain and in the frequency domain. It transforms a one-dimensional (1D) signal $x(t)$ into a two-dimensional (2D) function of time and frequency $T_x(t, f)$. This can be done by several approaches. The first class of solutions is called the linear TF representation¹ (TFRs) methods, which includes the famous STFT and the WT. The main concept used in this approach lies in the signal decomposition into elementary parts (atoms) and tries to localize each part in time and frequency properly and simultaneously. The second approach concerning the TF methods is the quadratic transforms, which aim at distributing the energy of the signal over the two description variables: time and frequency. Each approach has some advantages and drawbacks; while linear TFRs are intuitive, they suffer from poor TF resolution in many cases. This depends on the windows used to analyze the signal. However, the quadratic transforms (for

¹ Also known as atomic decomposition methods.

example the Wigner–Ville transform) have a high TF resolution. However, they suffer from cross-terms in multicomponent signals and may also suffer from inner interferences for monocomponent signals. There is no TF method that can be considered as optimal for all applications.

In this chapter, we will briefly present the STFT and the WT for the linear TF methods, and for the quadratic methods we will talk about the Wigner–Ville transform and Cohen’s class as a generalization of quadratic TFRs. Then, we will study the ST that can be considered as a linear TF method and present some algorithms to enhance its energy resolution in the TF plane. Next, we will consider the mathematical properties of the ST-spectrogram, which is a normal transition between the linear and the energetic (quadratic) representations. Finally, some complexity measures applied to the TF coefficients of the ST-spectrogram will be discussed and some potential related applications will be presented.

2.2. Synthetic signals

In the following sections, three synthetic signals will be used to illustrate some examples about the different TF methods presented in this chapter:

- A signal with four short-duration transients:

$$\begin{aligned}x_1(t) = & e^{-35\pi(t-0.5)^2} \cos(40\pi t) + e^{-35\pi(t-0.5)^2} \cos(160\pi t) \\& + e^{-55\pi(t-0.2)^2} \cos(100\pi t) + e^{-45\pi(t-0.8)^2} \cos(100\pi t)\end{aligned}\quad [2.1]$$

- A signal with a fast frequency variation and crossing components:

$$x_2(t) = \cos(20\pi \ln(10t+1)) + \cos(48\pi t + 8\pi t^2) \quad [2.2]$$

- A signal with three sinusoidal components:

$$\begin{cases} x_3(t) = \cos(2\pi f_1 t) & 0 \leq t \leq 80 \text{ ms} \\ x_3(t) = \cos(2\pi f_1 t) + \cos(2\pi f_2 t) & 80 \leq t \leq 220 \text{ ms} \\ x_3(t) = \cos(2\pi f_1 t) & 220 \leq t \leq 500 \text{ ms} \\ x_3(t) = \cos(2\pi f_3 t) & 500 \leq t \leq 1,000 \text{ ms} \end{cases} \quad [2.3]$$

2.3. The STFT

The short-time Fourier transform (STFT) is one of the best-known TF transforms [GAB 46]. Normally, it is the first choice to transform a 1D signal into a 2D time

and frequency plane. The STFT performs a TF analysis by using a sliding window with a constant width (monoresolution) that limits the TF resolution in certain cases. The signal inside the window is considered as stationary to manifest the fact that the signal has the same spectral information during the entire duration of observation. It can be classified as a linear TF method.

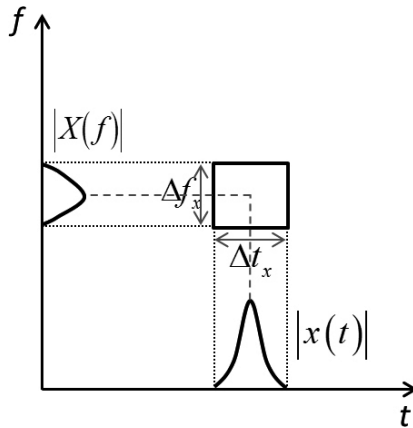


Figure 2.1. Representation of the time–frequency atom and the time–frequency localization: the temporal envelope $|x(t)|$ and the spectral envelope $|X(f)|$

We can describe the STFT of a signal $x(t)$ as follows:

$$STFT_x(\tau, f) = \int_{-\infty}^{+\infty} x(t) h^*(t - \tau) e^{-2j\pi ft} dt \quad [2.4]$$

where $h(t - \tau)$ is the sliding window.

The inverse STFT can be given as:

$$x(t) = \iint_{-\infty}^{\infty} STFT_x(t, f) h(t - \tau) e^{-2j\pi ft} dt df \quad [2.5]$$

Figure 2.2 shows the three synthetic signals (equations [2.1]–[2.3]) and their STFT representations computed with a Gaussian window.

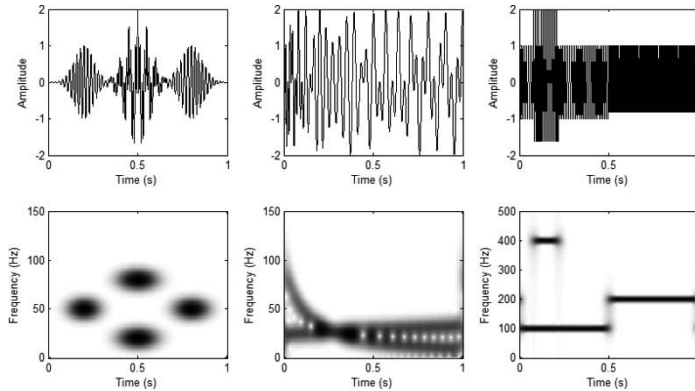


Figure 2.2. STFT with a Gaussian window of the different synthetic signals

The energy density spectrum of the STFT is called a spectrogram and it can be given as:

$$\left| \text{STFT}_x(\tau, f) \right|^2 = \left| \int_{-\infty}^{+\infty} x(t) h^*(t - \tau) e^{-2j\pi ft} dt \right|^2 \quad [2.6]$$

The spectrogram can be viewed as a normal transition between an atomic decomposition and an energy distribution.

2.4. The WT

The continuous WT (CWT) of $x(t)$ at a delay τ and a scale a is given as [MAL 99, DAU 92, VET 95]:

$$W(\tau, a) = \int_{-\infty}^{+\infty} x(t) \Phi_{\tau,a}^*(t) dt \quad [2.7]$$

where Φ^* is the complex conjugate of the mother wavelet function. The family of waveforms is obtained by translating and scaling a single wavelet by τ and a , respectively:

$$\Phi_{\tau,a}(t) = \frac{1}{\sqrt{a}} \Phi\left(\frac{t - \tau}{a}\right) \quad [2.8]$$

$\Phi_{\tau,a}(t)$ is normalized by $\frac{1}{\sqrt{a}}$ so it has the same energy at all scales.

The reconstruction formula of the WT is given by [GOU 84]:

$$x(t) = \frac{1}{C_\Phi} \iint_{-\infty}^{\infty} W(\tau, a) \frac{1}{\sqrt{a}} \Phi\left(\frac{t-\tau}{a}\right) \frac{dad\tau}{a^2} \quad [2.9]$$

where

$$C_\Phi = \int_{-\infty}^{+\infty} \frac{\hat{\Phi}(f)}{|f|} df < \infty \quad [2.10]$$

where $\hat{\Phi}$ is the Fourier transform of Φ .

The wavelet function must have a finite energy to have a compact support. So the wavelet mother function must satisfy an admissibility condition: $C_\Phi < \infty$ to guarantee the reconstruction of x without a distortion [VEN 08]. In order to satisfy [2.10], Φ must have a zero average, $\hat{\Phi}(0) = 0$, and $\hat{\Phi}(f)$ must be continuously differentiable.

An excellent summary of the historical and theoretical development of wavelets is available in [DAU 92, MAL 99].

2.5. The Wigner–Ville distribution

The Wigner-Ville distribution (WVD) is a well-known TF distribution that has been proposed by Wigner in a quantum mechanical context [WIG 32]. Ville was the first to introduce the Wigner distribution in the signal processing field [VIL 48]. WVD satisfies interesting theoretical and mathematical properties. It generates real values, satisfies the marginal properties and preserves time and frequency shifts that draw the analogy between the signal energy densities and distribution in the TF domain and the probability densities [BAR 01].

The WVD of signal $x(t)$ can be given as:

$$W_x(t, f) = \int_{-\infty}^{+\infty} x(t + \tau/2)x^*(t - \tau/2)e^{-j2\pi f\tau} d\tau \quad [2.11]$$

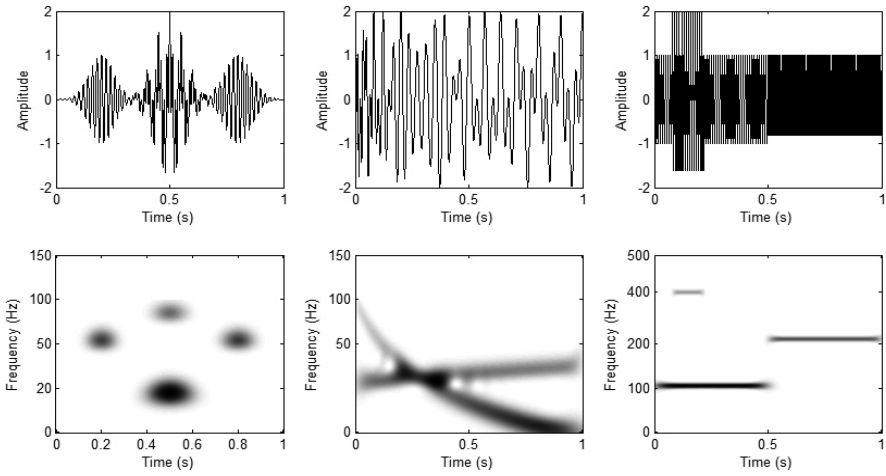


Figure 2.3. The Morlet wavelet of the different synthetic signals

The WVD can be understood as the Fourier transform of the instantaneous autocorrelation function of $x(t)$. However, the distribution suffers from the problem of interference terms, which is a classic problem in bilinear transforms. If we consider another signal $y(t)$, the WVD of the sum of the two signals ($x+y$) can be written as:

$$W_{x+y}(t, f) = W_x(t, f) + W_y(t, f) + 2\Re\{W_{x+y}(t, f)\} \quad [2.12]$$

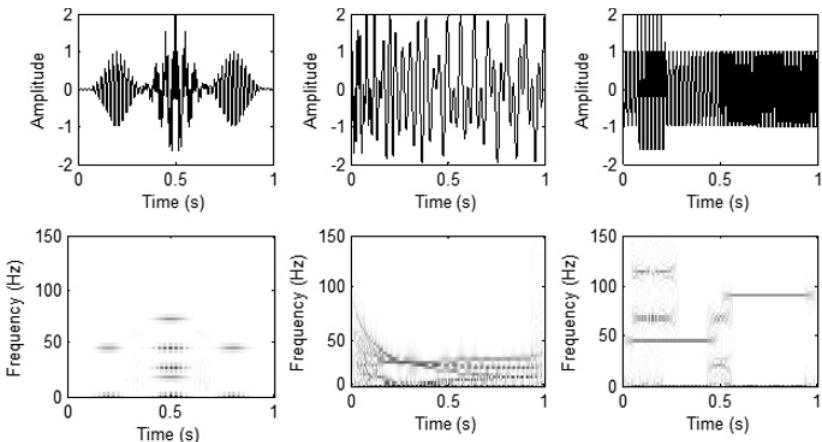


Figure 2.4. WVD of the different synthetic signals

The interference terms (third term in equation) make the image generated by the WVD difficult to interpret and this can be considered as a serious limitation in any feature extraction and classification algorithm based on the WVD.

2.5.1. The pseudo-WVD

The pseudo-WVD (PWVD) consists of applying a window to the standard WVD. The WVD is highly non-local and the effect of the windowing is to reduce it [COH 95]. The PWVD can be given as:

$$PW_x(t, f) = \int_{-\infty}^{+\infty} h(\tau) x(t + \tau/2) x^*(t - \tau/2) e^{-j2\pi f\tau} d\tau \quad [2.13]$$

where $h(t)$ is a regular window. The windowing operation is equivalent to a frequency smoothing of the WVD:

$$PW_x(t, f) = \int_{-\infty}^{+\infty} H(f - \alpha) W_x(t, \alpha) d\alpha \quad [2.14]$$

where $H(f)$ is the Fourier transform of $x(t)$. Thus, because of their oscillating nature, the interferences will be attenuated in the PWVD compared to the WVD. However, the consequence of this improved readability is that many properties of the WVD are lost: the marginal properties, the unitarity and also the frequency-support conservation; on the other hand, the frequency widths of the auto-terms are increased by this operation [AUG 96].

2.5.2. The smoothed PWVD

To add a degree of freedom to the PWVD, the smoothed PWVD (SPWVD) allows independent time and frequency smoothing as follows:

$$SPW_x(t, f) = \int_{-\infty}^{+\infty} h(\tau) \int_{-\infty}^{+\infty} g(u - t) x(u + \tau/2) x^*(u - \tau/2) du e^{-j2\pi f\tau} d\tau \quad [2.15]$$

The SPWVD has a separable smoothing kernel $g(t)$ and $H(f)$ that provides an independent control of the time and frequency resolutions. For a zero-time resolution, i.e. $g(t) = \delta(t)$, the calculated SPWVD has no time smoothing. Thus, the resulting TF distribution is the PWVD. Smoothing the TF distribution affects the

TF localization of the signal content. Therefore, a trade-off between interference attenuation and TF localization occurs to ensure a good TFR [CHO 89a, COH 89b].

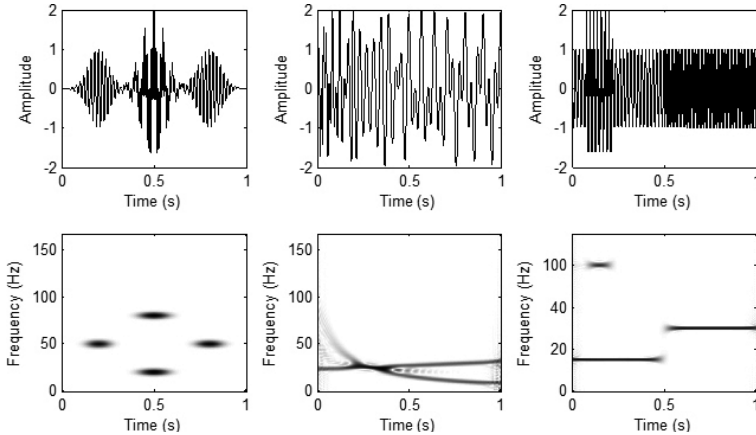


Figure 2.5. SPWVD of the different synthetic signals

2.6. Cohen's class

Cohen proposed to characterize the TFRs by a kernel function [COH 66]. Cohen's class generalizes the bilinear TF methods mathematically. The properties of the representation are determined by the constraints applied to the kernel function [COH 95].

Cohen's class can be written as:

$$C_x(t, f) = \frac{1}{4\pi^2} \iiint_{-\infty}^{+\infty} x(u + \tau/2)x^*(u - \tau/2)\phi(\theta, \tau)e^{-j\theta t - j\tau f + j\theta u}dud\tau d\theta \quad [2.16]$$

where $\phi(\theta, \tau)$ is the kernel function that determines the distribution and its properties. For example, if $\phi(\theta, \tau) = 1$, the WVD is retrieved. The spectrogram can be retrieved when:

$$\phi(\theta, \tau) = \int_{-\infty}^{+\infty} h(u + \tau/2)h^*(u - \tau/2)e^{-j\theta u}du \quad [2.17]$$

where $h(t)$ is the window function used to compute the spectrogram.

Cohen's class can be rewritten in terms of an ambiguity function $A(\theta, \tau)$. The ambiguity function can be considered as a joint TF autocorrelation function. It can be given as follows:

$$A_x(\theta, \tau) = \int_{-\infty}^{+\infty} x(u + \tau/2)x^*(u - \tau/2)e^{j\theta u} du \quad [2.18]$$

Thus, Cohen's class can be rewritten as follows:

$$C_x(t, f) = \frac{1}{4\pi^2} \iint A(\theta, \tau)\phi(\theta, \tau)e^{-j\theta t - j\tau f} d\tau d\theta \quad [2.19]$$

This reformulation provides an easier understanding of the auto- and cross-terms location [SEJ 09]. All auto-terms are located along and around the ambiguity domain axis, and hence the maximum occurs around the origin. For the non-overlapping components, the cross-terms are dislocated further from the axis [HLA 92]. Extensive review of the properties of the different proposed kernels is beyond the scope of this book. For more detail, readers may refer to [WIL 89, JEO 92].

2.7. The S-transform

The S-transform (ST) is a TF transform proposed by Stockwell [STO 96] and can be considered as a hybrid method between the STFT and the WT. It can be viewed as a frequency-dependent STFT or a phase-corrected WT. The frequency-dependent window allows a frequency-dependent resolution with narrower windows at higher frequencies and wider windows at lower frequencies [SIM 07]. Contrary to the WT, the phase information provided by the S-transform is linked to the time origin by using the Fourier kernel, which is not possible with the CWT where the phase information is locally referenced. For these reasons, the S-transform is becoming a valuable tool applied to many signals and domains such as cardiovascular [MOU], electroencephalography (EEG) signals [PIN 09], geophysics [STO 01, PIN 03b], power system engineering [DAS 03, RED 12], medical imaging [ASO 06, AND 01], etc. In addition, it has gained popularity in the signal processing community because of its easy interpretation and fast computation [CHE 10].

The S-transform of a time-varying signal $x(t)$ is defined by [STO 96]:

$$S_x(\tau, f) = \int_{-\infty}^{+\infty} x(t)w(t - \tau, f)e^{-2\pi jft} dt \quad [2.20]$$

where the window function $w(\tau - t, f)$ is chosen as:

$$w(t, f) = \frac{1}{\sigma(f)\sqrt{2\pi}} e^{\frac{-t}{2\sigma(f)^2}} \quad [2.21]$$

and $\sigma(f)$ is a function of frequency as:

$$\sigma(f) = \frac{1}{|f|} \quad [2.22]$$

Therefore, the S-transform becomes:

$$S_x(\tau, f) = \frac{|f|}{\sqrt{2\pi}} \int_{-\infty}^{+\infty} x(t) e^{\frac{-(t-\tau)^2 f^2}{2}} e^{-i2\pi f t} dt \quad [2.23]$$

The 1D function of the time-variable τ and fixed-frequency f_1 defined by $S_x(\tau, f_1)$ is called the *voice*. The 1D function of the frequency-variable f and fixed-time τ_1 defined by $S_x(\tau_1, f)$ is called the *local spectrum* [STO 96]. The zero frequency voice is independent of time and equal to the signal average. It can be expressed as follows:

$$S_x(\tau, 0) = \lim_{T \rightarrow +\infty} \frac{1}{T} \int_{-T/2}^{+T/2} x(t) dt \quad [2.24]$$

The window is normalized as:

$$\int_{-\infty}^{+\infty} w(t, f) dt = 1 \quad \forall f \in \mathbb{R} \quad [2.25]$$

This normalization will allow the S-transform to be invertible and to have a direct relationship with the Fourier transform, which is a very important property of the ST as it will be discussed later.

2.7.1. Properties of the S-transform

2.7.1.1. Relationship with the Fourier transform

A direct relationship between the S-transform and the Fourier spectrum can be given by averaging the local spectrum over time as follows:

$$\int_{-\infty}^{+\infty} S_x(\tau, f) d\tau = X(f) \quad [2.26]$$

This gives:

$$x(t) = \int_{-\infty}^{+\infty} \left\{ \int_{-\infty}^{+\infty} S_x(\tau, f) e^{i2\pi f t} df d\tau \right\} dt \quad [2.27]$$

where $X(f)$ is the Fourier transform of $x(t)$.

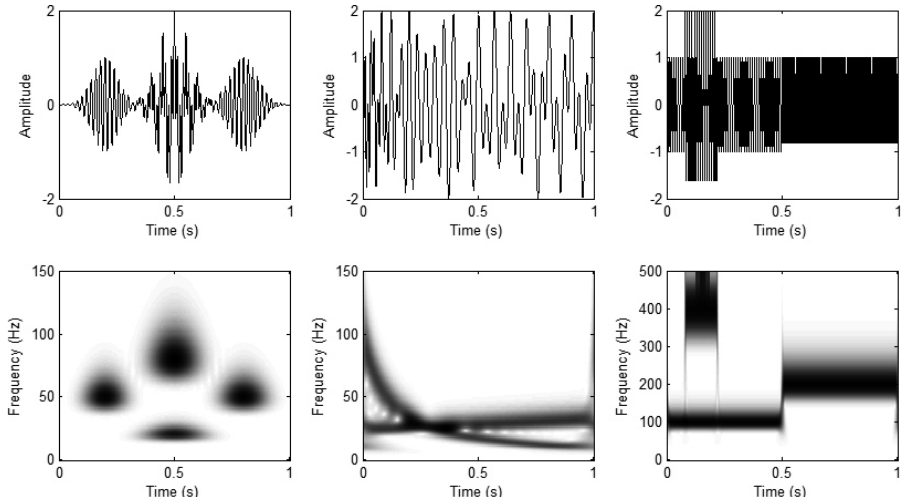


Figure 2.6. S-transform of the different synthetic signals

PROOF.–

$$\begin{aligned} \int_{-\infty}^{+\infty} S_x(\tau, f) dt &= \iint_{-\infty}^{+\infty} x(t) w(t - \tau, f) e^{-2\pi j f t} dt \\ &= \iint_{-\infty}^{+\infty} x(t) e^{-2\pi j f t} w(t - \tau, f) dt \\ &= X(f) \int_{-\infty}^{+\infty} w(t - \tau, f) dt \\ &= X(f) \end{aligned}$$

Another way to directly express the link between the S-transform and the Fourier transform is by writing the ST as a convolution as follows:

$$\begin{aligned} S_x(\tau, f) &= \int_{-\infty}^{+\infty} p(t, f) g(\tau - t, f) dt \\ &= p(\tau, f) * g(\tau, f) \end{aligned} \quad [2.28]$$

where

$$p(\tau, f) = x(\tau) e^{-i2\pi f \tau}$$

and

$$g(\tau, f) = \frac{|f|}{\sqrt{2\pi}} e^{\frac{-\tau^2 f^2}{2}}$$

By calculating the Fourier transform of $S_x(\tau, f)$, the convolution becomes a multiplication in the frequency domain:

$$\begin{aligned} F_{\tau \rightarrow \alpha} \{S_x(\tau, f)\} &= P(\alpha, f) G(\alpha, f) \\ &= X(\alpha + f) e^{\frac{-2\pi^2 \alpha^2}{f^2}} \end{aligned}$$

where α is the frequency Fourier variable related to τ .

The direct link between the S-transform and the Fourier transform can be obtained by applying the inverse Fourier transform to the above equation:

$$S(\tau, f) = \int_{-\infty}^{+\infty} X(\alpha + f) e^{\frac{-2\pi^2 \alpha^2}{f^2}} e^{i2\pi \alpha \tau} d\alpha \quad [2.29]$$

This will facilitate the implementation of the ST by using the advantages of the fast Fourier transform (FFT) algorithms. The exponential function in equation [2.28] is the frequency-dependent localizing window. This window is centered on the zero frequency and thus plays the role of a low-pass filter for each particular voice [STO 07b].

2.7.1.2. Linearity

The S-transform justifies the linearity property. This is advantageous for the case of additive noise where the noisy signal $x_n(t)$ can be written as:

$$x_n(t) = x(t) + n(t)$$

where $x(t)$ is the considered signal and $n(t)$ is the additive noise.

The S-transform of the signal $x_n(t)$ is given as:

$$ST\{x_n(t)\} = ST\{x(t)\} + ST\{n(t)\}$$

This is an advantage over the bilinear class of TF transformation where:

$$TF\{x_n(t)\} = TF\{x(t)\} + TF\{n(t)\} + 2 * TF\{x(t)\} * TF\{n(t)\}$$

2.7.1.3. Time shift

It is not difficult to show that shifting the signal $x(t)$ by t_0 in the time domain results in multiplying the S-transform with a phase factor:

$$S_y(\tau, f) = S_x(\tau, f) e^{-i2\pi f t_0}$$

where

$$y(t) = x(t - t_0)$$

PROOF.–

If we translate the time series by an amount t_0 , one can study the effect on the S-transform by making a change of variables $t \rightarrow k - t_0$. The S-transform equation becomes:

$$S_x(\tau, f) = \frac{|f|}{\sqrt{2\pi}} \int_{-\infty}^{+\infty} x(k - t_0) e^{\frac{-(k-t_0-\tau)^2 f^2}{2}} e^{-i2\pi f(k-t_0)} dk$$

By performing another change of variables $\tau \rightarrow z - t_0$, we obtain:

$$\begin{aligned} S_x(z-t_0, f) &= \frac{|f|}{\sqrt{2\pi}} \int_{-\infty}^{+\infty} x(k-t_0) e^{\frac{-(k-t_0-z+t_0)^2}{2}} e^{-i2\pi f(k-t_0)} dk \\ &= \frac{|f|}{\sqrt{2\pi}} \int_{-\infty}^{+\infty} x(k-t_0) e^{\frac{-(k-z)^2}{2}} e^{-i2\pi fk} e^{-2\pi ft_0} dk \end{aligned}$$

Hence, the S-transform shift theorem states that if [STO 07b]:

$$x(t) \Leftrightarrow S_x(\tau, f)$$

$$x(t-t_0) \Leftrightarrow S_x(\tau, f) e^{-i2\pi ft_0}$$

2.7.1.4. Relation with STFT

By applying a window $g(t)$ to the signal $x(t)$, the resulting spectrum can be given as:

$$X(f) = \int_{-\infty}^{+\infty} x(t) g(t) e^{-2\pi i ft} dt$$

The S-transform can be found by defining a normalized Gaussian window and by allowing the Gaussian to be a function of translation τ and dilation σ :

$$g(t) = \frac{1}{\sigma\sqrt{2\pi}} e^{\frac{-(t-\tau)^2}{2\sigma^2}}$$

The STFT can be found by fixing the value of σ . However, for the S-transform, σ is a function of frequency that gives the multiresolution characteristic for the transform:

$$\sigma(f) = \frac{1}{|f|}$$

2.7.1.5. The S-transform from a wavelet point of view

As shown in [STO 96] and [GIB 06], the S-transform can be expressed in terms of a CWT as follows:

$$S_x(\tau, f) = \sqrt{|f|} e^{-2\pi i ft} W(\tau, a) \quad [2.30]$$

where $W(\tau, a)$ is the CWT that is given as:

$$W(\tau, a) = \int_{-\infty}^{+\infty} x(t) \frac{1}{\sqrt{|a|}} \Phi^* \left(\frac{t-\tau}{a} \right) dt$$

and the mother wavelet $\Phi(t)$ is the modulated Gaussian or the complex Morlet wavelet [DAU 92]:

$$\Phi(t) = \frac{1}{\sqrt{2\pi}} e^{-\frac{t^2}{2}} e^{2\pi i t}$$

PROOF.–

Let us go back to equation [2.22] of the S-transform:

$$S_x(\tau, f) = \frac{|f|}{\sqrt{2\pi}} \int_{-\infty}^{+\infty} x(t) e^{\frac{-(t-\tau)^2 f^2}{2}} e^{-i2\pi f t} dt$$

Letting $a = \frac{1}{f}$ and extracting a phase modulation $e^{-2\pi if\tau}$ and amplitude $\sqrt{|f|}$

from the integral in the last equation [GIB 06], $S_x(\tau, f)$ becomes:

$$\begin{aligned} S_x(\tau, f) &= \sqrt{|f|} e^{-2\pi if\tau} \int_{-\infty}^{+\infty} x(t) \sqrt{\frac{|f|}{2\pi}} e^{\frac{-(t-\tau)^2 f^2}{2}} e^{-2\pi if(t-\tau)} dt \\ &= \sqrt{|f|} e^{-2\pi if\tau} \int_{-\infty}^{+\infty} x(t) \frac{1}{\sqrt{a} \sqrt{2\pi}} e^{\frac{-(t-\tau)^2}{2a^2}} e^{\frac{-2\pi i(t-\tau)}{a}} dt \\ &= \sqrt{|f|} e^{-2\pi if\tau} \int_{-\infty}^{+\infty} x(t) \frac{1}{\sqrt{a}} \phi^* \left(\frac{t-\tau}{a} \right) dt \\ &= \sqrt{|f|} e^{-2\pi if\tau} W(\tau, a) \end{aligned}$$

The S-transform can be considered as a special case of the CWT with the Morlet mother wavelet [VEN 08], with the linear frequency scale features and the absolutely referenced phase in contrast with the classic wavelet. Strictly speaking, the wavelet function does not satisfy the admissibility condition because of its non-zero mean. However, this mean is too small and can be negligible for all practical purposes [GIB 06].

2.7.1.6. Phase information

In many applications, only the amplitude of the transforms is observed since it is more intuitive. However, the phase information in the complex transforms can be useful for feature extraction and classification schemes [MEI 12, PIN 09]. A key feature of the S-transform is that it uniquely combines a frequency-dependent resolution of the TF space with absolutely referenced local phase information in contrast to the CWT [STO 07b].

The CWT provides time resolution by translating its whole analyzing function (the wavelet) along the time axis. The S-transform is different because only the amplitude envelope of the analyzing function (the Gaussian window) translates; the oscillations are given by the fixed Fourier sinusoid that does not depend on τ [PIN 04].

2.7.1.7. Amplitude-conservative

The S-transform does not satisfy the energy conservation property contrary to the wavelet or the STFT transforms. However, the S-transform can be considered as an amplitude-conservative transform in which the average amplitude of the signal is kept [VEN 08].

Figure 2.7 shows a comparison between a Morlet wavelet and the S-transform for a decreasing chirp of constant amplitude. The figure clearly shows that the amplitude of the Morlet wavelet increases as the frequency decreases. However, the S-transform preserves the amplitude of the signal independently of the analyzed frequency.

2.7.1.8. S-transform and instantaneous frequency

A particular voice of the S-transform can be written as:

$$S_x(\tau, f_1) = A(\tau, f_1) e^{i\phi(\tau, f_1)}$$

where the amplitude $A(\tau, f_1)$ can be written as:

$$A(\tau, f_1) = \sqrt{\Re\{S_x(\tau, f_1)\}^2 + \Im\{S_x(\tau, f_1)\}^2}$$

and the phase $\phi(\tau, f_1)$ is given as:

$$\phi(\tau, f_1) = \arctan\left(\frac{\Im\{S_x(\tau, f_1)\}}{\Re\{S_x(\tau, f_1)\}}\right)$$

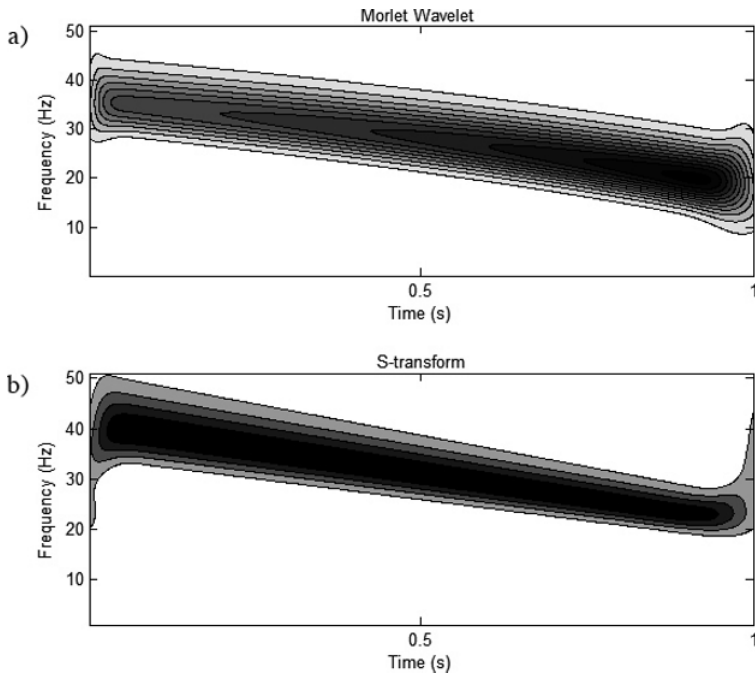


Figure 2.7. a) The Morlet wavelet and
b) the S-transform for a decreasing chirp of constant amplitude

The phase can be used to determine the instantaneous frequency as follows:

$$IF(\tau, f_i) = \frac{1}{2\pi} \frac{\partial}{\partial \tau} \{2\pi f_i + \phi(\tau, f_i)\}$$

2.7.1.9. Inverse S-transform

There are two ways to compute the inverse S-transform based on different philosophies; the frequency inverse S-transform and the time inverse S-transform [SIM 07].

– Frequency inverse S-transform

As has been shown before, the Fourier transform is obtained by summing the S-transform over time:

$$\int_{-\infty}^{+\infty} S_x(\tau, f) d\tau = X(f)$$

Therefore, the original signal can be obtained by summing over all frequencies:

$$\iint_{-\infty}^{\infty} S_x(\tau, f) e^{2i\pi f t} d\tau df = x(t)$$

– *Time inverse S-transform*

A time–time function of the windowed signal $x(t)$ is proposed by Schimmel and Gallart [SCH 05]:

$$z(\tau, t) = x(t) e^{-\frac{f^2(\tau-t)^2}{2k^2}}$$

For any frequency f , the function $z(\tau, t)$ reduces to $x(t) = z(t, t)$ at $\tau = t$. After the Fourier transform of the function z , the function becomes:

$$z(\tau, f) = \frac{k\sqrt{2\pi}}{|f|} S(\tau, f)$$

and therefore, the original signal $x(t)$ can be retrieved from the weighted S-spectrum through the “diagonal elements” of the time–time representation obtained with the following back transformation [SCH 05]:

$$x(t) = k\sqrt{2\pi} \int_{-\infty}^{+\infty} \frac{S(\tau, f)}{|f|} e^{i2\pi f t} d\tau \quad [2.31]$$

The inverses differ due to their different strategies. However, the main drawback of the frequency inverse version is that it obliges the calculation of a number of frequency voices equal to time samples, which can be considered a serious problem when dealing with big data. The time approach may often be the better choice if we are interested in time domain postprocessing or interpretations. Conversely, the frequency inverse transform can be an advantage whenever frequency separation is more important than time separation [SIM 07].

2.7.2. The discrete S-transform

Let $x[n] = x(nT)$, $n = 0, \dots, N-1$ denote the discrete time series, corresponding to $x(t)$, with a time sampling interval of T . Let $f_s = 1/T$ be the sampling frequency and f_0 be the frequency step, $M = f_0/f_s$ and $m = -M/2, \dots, M/2-1$ is the index of frequency range. Thus, the discrete S-transform can be written as:

$$S[p, m] = \sum_{n=0}^{N-1} x[n] \frac{|m|}{kM\sqrt{2\pi}} e^{-\frac{1}{2}\left(\frac{m(p-n)}{Mk}\right)^2} e^{-2i\pi \frac{nm}{M}}$$

with $p = 0, \dots, N-1$ being the time index.

Normally, the direct relationship between the S-transform and the Fourier transform is used to compute the discrete S-transform:

$$S[p, m] = \sum_{n=-M/2}^{M/2-1} X\left[\frac{m+n}{M}\right] e^{-2\left(\frac{\pi nk}{m}\right)^2} e^{2i\pi \frac{np}{M}} \quad [2.32]$$

where $X\left[\frac{m}{M}\right]$ is the discrete Fourier transform of $x[n]$.

2.7.2.1. The S-transform algorithm flowchart

As mentioned before, the direct relationship between the S-transform and the Fourier transform facilitates the implementation of the ST using the advantages of the FFT algorithm. The Fourier transform of the input signal needs to be calculated only once. For each required value of the frequency m , the spectrum can be shifted in the negative frequency direction by m . The Gaussian window $G[n, m]$ can then be evaluated and the S distribution is calculated using the inverse Fourier transform.

The implementation algorithm can be illustrated as follows.

2.7.2.2. The discrete orthonormal S-transfom (DOST)

A drawback of the S-transform is the redundant representation of the TF space and the consumption of computing resources it requires (a characteristic it shares with the CWT, the STFT and Cohen's class of generalized TF distributions) [STO 07a]. Stockwell introduced an orthogonal set of basis functions that localizes the spectrum and retains the advantageous phase properties of the S-transform. These basis functions are defined by phase characteristics that are directly related to the phase of the Fourier transform spectrum, and are both compact in frequency and localized in time.

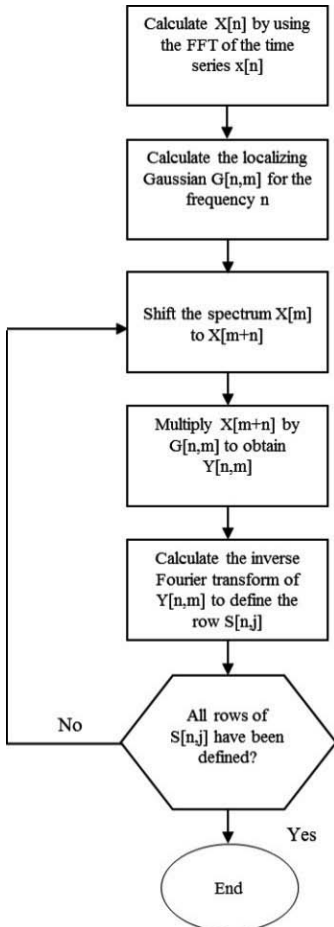


Figure 2.8. The S-transform algorithm flowchart

The efficient representation of the S-transform can be defined as the inner products between a time series $x[kT]$ and the basis functions defined as a function of these products, with the parameters ν (a frequency variable indicative of the center of a frequency band), β (indicating the width of the frequency band) and τ (a time variable indicating the time localization) [STO 07a].

$$S\{x[kT]\} = S\left(\tau T, \frac{f}{NT}\right) = \sum_{k=0}^{k=N-1} S_{\{\nu, \beta, \tau\}}[kT]$$

The basis function $S_{\{\nu, \beta, \tau\}}[kT]$ is written as:

$$S_{\{\nu, \beta, \tau\}}[kT] = \frac{1}{\sqrt{\beta}} \sum_{f=\nu-\beta/2}^{\nu+\beta/2-1} e^{i2\pi\frac{k}{N}f} e^{-i2\pi\frac{\tau}{\beta}f} e^{-i2\pi\frac{N}{2NT}\tau T} \quad [2.33]$$

where $1/\sqrt{\beta}$ is a normalization factor to ensure the orthonormality of the basis functions. Hence, the basis functions for the DOST of voice frequency ν , bandwidth β and time index τ can be given as:

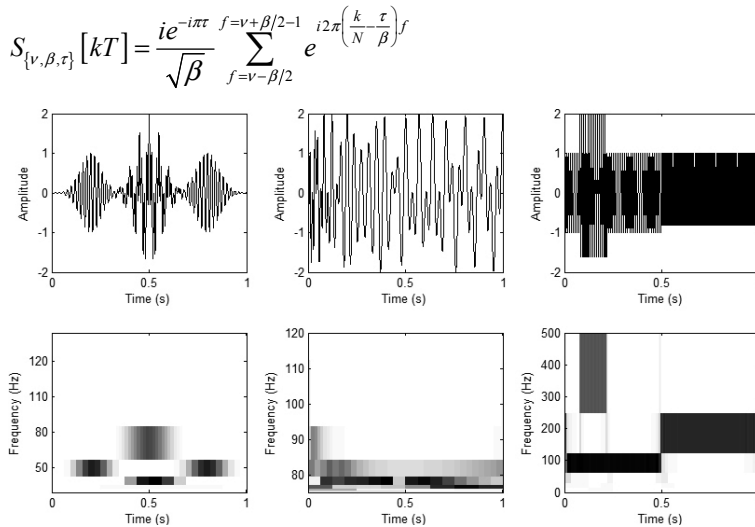


Figure 2.9. The DOST calculated for the synthetic signals

2.7.3. The improvement of the S-transform energy concentration

In some cases, the S-transform can suffer from poor energy concentration in the TF domain; it provides good concentration at lower frequencies, but poor concentration at higher frequencies. Many studies tried to improve the TFR of the S-transform [MCF 99, PIN 03a, PIN 03b]. The main study in the literature focused on optimizing the energy concentration directly in the TF domain was the Sejdic's paper [SEJ 08], i.e. to minimize the spread of the energy beyond the actual signal components. As is well known, the ideal TF transformation should only be distributed along frequencies for the duration of signal components. So, the neighboring frequencies would not contain any energy and the energy contribution of each component would not exceed its duration [GRO 01]. It has been shown that the original S-transform uses a Gaussian window, whose standard deviation varies

over frequency. Whatever the analyzed signal, the width of the Gaussian window will decrease as the frequency increases. This produces a higher frequency resolution at lower frequencies and a higher time resolution at lower frequencies. However, this strategy can be considered as a limitation since it does not take the nature of the analyzed signal into consideration. It would be more appropriate to adapt the window to the signal in order to maximize the resolution of the S-transform.

The energy concentration in the TF domain is a very important parameter for the algorithms that aim at detecting the duration of any given events in a signal or extracting the relevant features from the TF domain. Hence, an energy concentration optimization process is important to improve the segmentation and the classification of non-stationary signals.

2.7.3.1. Ideal energy concentration in the TF plane

Before introducing the energy concentration enhancement algorithms, a brief introduction to the ideal energy concentration in the TF plane is needed.

The ideal TFR should only be distributed along frequencies for the duration of signal components. The neighboring frequencies would not contain any energy and the energy contribution of each component would not exceed its duration [GRO 01]. To clarify this concept, let us consider two examples [SEJ 08] of signals:

Signal $x(t)$ can be written as follows:

$$x(t) = A_x e^{j\phi(t)}$$

where $|dA(t)/dt| \ll |d\phi(t)/dt|$ and the instantaneous frequency of $x(t)$ is given as:

$$f(t) = \frac{1}{2\pi} \frac{\partial}{\partial t} \phi(t)$$

The second signal has a Fourier transform as follows:

$$X(f) = G(f) e^{j\phi(f)}$$

where the spectrum is slowly varying in comparison to phase $|dG(f)/df| \ll |d\phi(f)/df|$. The ideal TFRs of these signals are given, respectively, as [STA 94]:

$$ITFR_{x(t)}(t, f) = 2\pi A(t)\delta(f - \frac{1}{2\pi} \frac{d\phi(t)}{dt}) \quad [2.34]$$

$$ITFR_{X(f)}(t, f) = 2\pi G(f)\delta(t + \frac{d\phi(f)}{df}) \quad [2.35]$$

The two representations are ideally concentrated along the instantaneous frequency. A sinusoidal signal and a Dirac signal can be considered as examples of the models given above. Figure 2.10 shows the difference between the ideal TFRs and the S-transform representations where the frequencies surrounding 50 Hz in the sinusoidal signal have a robust contribution and the frequencies surrounding the time instant of the Dirac also have a frequency with a strong contribution.

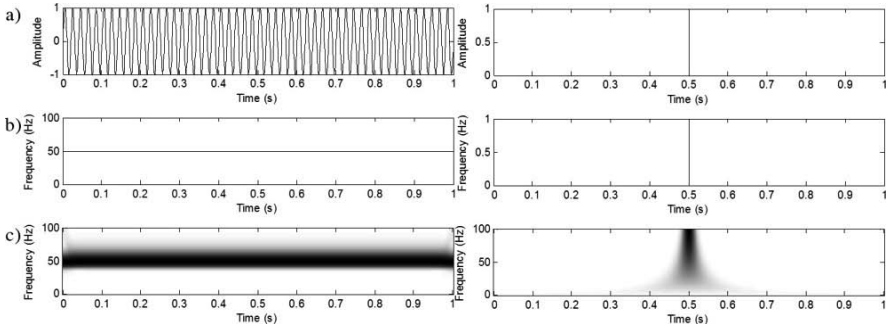


Figure 2.10. a) Time representation of sinusoidal and Dirac signals, b) their ideal time–frequency representation and c) their S-transform representations (bottom)

2.7.3.2. Window width dependent algorithm

The main approach used in [SEJ 08] was to optimize the width of the window used in the S-transform. The width of the Gaussian window can be controlled by several methods by adding a new parameter to the window equation. In section 2.7.3.3, the concept of optimizing the energy concentration of the S-transform by controlling the width of the analyzed windows is presented. Thus, several windows proposed in the literature and the different ways to control the Gaussian window are explored and a new Gaussian window is proposed and compared with the existing methods. The choice of parameters that control and modulate the window is also discussed.

First, let us return to the equation of the Gaussian window of the S-transform:

$$w(t, f) = \frac{1}{\sigma(f)\sqrt{2\pi}} e^{\frac{-t}{2\sigma(f)^2}}$$

where $\sigma(f)$ can be an arbitrary function that controls the width of the Gaussian window.

$$S_x(\tau, f) = \int_{-\infty}^{+\infty} x(t) \frac{1}{\sqrt{2\pi}\sigma(f)} e^{\frac{-(t-\tau)^2 f^2}{2[\sigma^2(f)]}} e^{-i2\pi ft} dt \quad [2.36]$$

2.7.3.3. The different ways to control the Gaussian window width

2.7.3.3.1. Parameter α

To better control the resolution of the S-transform, McFadden *et al.* [MCF 99] and later Pinnegar and Mansinha [PIN 03a, PIN 03b] introduced the generalized S-transform with a set of parameters that determine the shape and properties of the window. For the Gaussian window, the parameter α is introduced as follows:

$$w(\tau-t, f, \alpha) = \frac{|f|}{\alpha\sqrt{2\pi}} e^{\frac{-f^2(\tau-t)}{2\alpha^2}} \quad [2.37]$$

The parameter α controls the width of the Gaussian window as follows [MAN 97]:

$$\sigma(f) = \frac{\alpha}{|f|}$$

The S-transform related to parameter α can be written as:

$$S_x^\alpha(\tau, f) = \int_{-\infty}^{+\infty} x(t) \frac{|f|}{\sqrt{2\pi}\alpha} e^{\frac{-(t-\tau)^2 f^2}{2\alpha^2}} e^{-i2\pi ft} dt \quad [2.38]$$

The parameter f/α represents the number of cycles (periods) of a frequency that can be contained within one standard deviation σ of the Gaussian window.

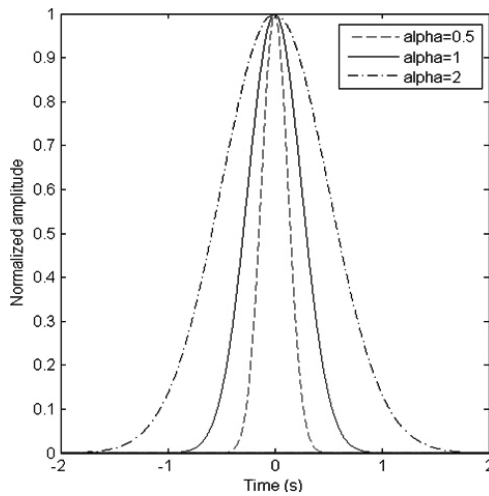


Figure 2.11. Normalized Gaussian window for different values of α

2.7.3.3.2. Parameter p

The parameter p proposed by Sejdic *et al.* [SEJ 08] to control the width of the Gaussian window is given as:

$$\sigma(f) = \frac{1}{|f|^p}$$

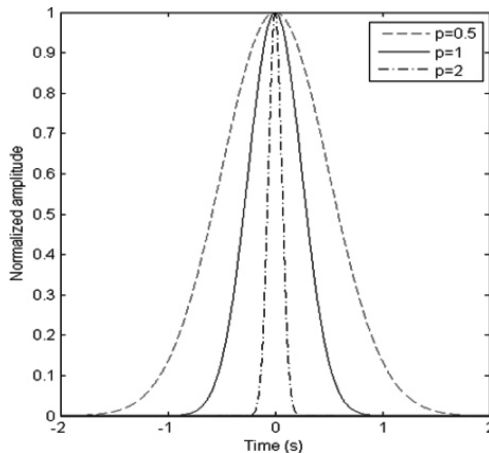


Figure 2.12. Normalized Gaussian window for different values of p

The S-transform related to the parameter p can be calculated as:

$$S_x^p(\tau, f) = \int_{-\infty}^{+\infty} x(t) \frac{|f|^p}{\sqrt{2\pi}} e^{\frac{-(t-\tau)^2 f^{2p}}{2}} e^{-i2\pi ft} dt \quad [2.39]$$

2.7.3.3.3. Progressive windows control (parameters m and k)

Another way to control the Gaussian window is to linearly vary the standard deviation of the window with the frequency to get better progressive control of the width [ASO 12]:

$$\gamma = mf + k$$

$$S_x^{m,k}(\tau, f) = \int_{-\infty}^{+\infty} x(t) \frac{|f|}{(mf+k)\sqrt{2\pi}} e^{\frac{-(t-\tau)^2 f^2}{2(mf+k)^2}} e^{-i2\pi ft} dt \quad [2.40]$$

The parameter $f/(mf+k)$ represents the number of cycles (periods) of a frequency that can be contained within one standard deviation σ of the Gaussian window. Hence, $\sigma(f)$ gives a progressive improved resolution in this case [ASO 12]. When too small, the Gaussian window retains very few cycles of the sinusoid and the frequency resolution degrades at low frequencies. In contrast, if it is too large, the window retains more cycles within it and, as a consequence, the time resolution degrades at high frequencies [ASO 12].

2.7.3.3.4. Proposed window

We propose to introduce a new parameter p to the version proposed by Assous *et al.* as follows:

$$\gamma = mf^p + k$$

Thus, the modified Gaussian window can be given as:

$$w(\tau-t, f, \gamma) = \frac{|f|}{(mf^p + k)\sqrt{2\pi}} e^{\frac{-(t-\tau)^2 f^2}{2(mf^p + k)^2}} \quad [2.41]$$

The parameter $f/(mf^p + k)$ represents the number of cycles (periods) of a frequency that can be contained within one standard deviation σ of the Gaussian

window. The introduced parameter p gives more flexibility to the Gaussian window than the version proposed in [ASO 12].

The modified S-transform becomes:

$$S_x^{m,p,k}(\tau, f) = \int_{-\infty}^{+\infty} x(t) \frac{|f|}{(mf^p + k)\sqrt{2\pi}} e^{\frac{-(t-\tau)^2 f^2}{2(mf^p + k)^2}} e^{-i2\pi f t} dt \quad [2.42]$$

The new window satisfies the normalization condition for the original S-transform window, which ensures the invertibility of the modified S-transform:

$$\int_{-\infty}^{+\infty} \frac{|f|}{(mf^p + k)\sqrt{2\pi}} e^{\frac{-(t-\tau)^2 f^2}{2(mf^p + k)^2}} dt = 1 \quad [2.43]$$

2.7.3.3.5. Choice of parameters

A crucial question is how to choose the parameters of the Gaussian window. Assous *et al.* empirically select the values of k that equal $1/N$, where N is the number of signal samples, and m equals four times the variance of the signal [ASO 12]. However, this cannot be generalized on all signals (see Figure 2.13). It will be more adequate to automatically generate adaptive parameters that respect the nature of the analyzed signal. Sejdic *et al.* introduced a parameter called p to the Gaussian window and this parameter varies between 0 and 1. Finally, for each value of p , the S-transform is calculated and the p , which gives the maximum energy concentration, is selected. In the method proposed in this chapter, the Gaussian window is modulated with three parameters rather than one parameter. We propose to apply a genetic algorithm (GA) to select the parameters m , p and k automatically (see Figure 2.13).

The GA based on the mechanisms of natural selection and genetics has been developed since 1975 [HOL 75]. GA has been proven to be very efficient and stable in searching for global optimum solutions. Usually, a simple GA is mainly composed of three operations: selection, genetic operation and replacement [KUM 10]. A summary of implementing GA can be given as follows [TAN 96]:

- 1) Randomly generate an initial population: $X(0) = \{x(1), x(2) \dots x(N)\}$.
- 2) Compute the fitness function $F(x_i)$ for each chromosome $x(i)$ in the population $X(t)$.

3) Create new chromosomes $X_r(t)$ by coupling current chromosomes, applying mutation and recombination as the parent chromosome mates.

4) Create the fitness of $X_r(t)$.

5) After a number of iterations, return the best chromosome that has the optimal fitness.

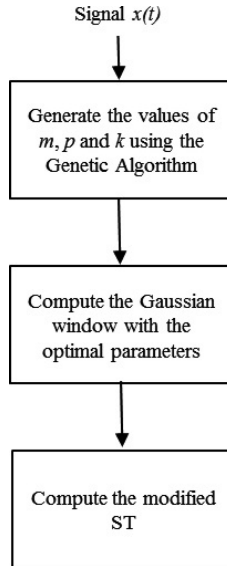


Figure 2.13. The proposed optimization module

The fitness function used in this chapter is the energy concentration measure proposed in [SEJ 08, STA 01]. By applying this measure to the proposed S-transform, we obtain:

$$CM(m, p, k) = \frac{1}{\int_{-\infty}^{+\infty} \int_{-\infty}^{+\infty} \left| \overline{S_x^{m,p,k}}(t, f) \right| dt df} \quad [2.44]$$

where

$$\overline{S_x^{m,p,k}}(t, f) = \frac{S_x^{m,p,k}(t, f)}{\sqrt{\int_{-\infty}^{+\infty} \int_{-\infty}^{+\infty} \left| S_x^{m,p,k}(t, f) \right|^2 dt df}} \quad [2.45]$$

The optimization problem can be expressed as follows:

$$\arg \max_{m, p, k} \left(\int_{-\infty}^{+\infty} \int_{-\infty}^{+\infty} \left(1 / \left| S_x^{m, p, k}(t, f) \right| \right) dt df \right) \quad [2.46]$$

where m, k and $p \in]0, 3]$. The population size of the GA is 20, the cross-over rate is 0.8, the mutation rate is 0.05 and the chromosome length is 3 (three variables m, p and k).

2.7.3.3.6. Application on synthetic signals

This section presents a comparison study between the proposed method and the methods referred to above [ASO 12, SEJ 08]. The GA is applied to the method proposed by Assous *et al.*, since it contains two parameters (m and k) to control the Gaussian width. This will allow us to evaluate the contribution of the newly introduced parameter p in this study.

We propose to compare the three synthetic signals used in this chapter.

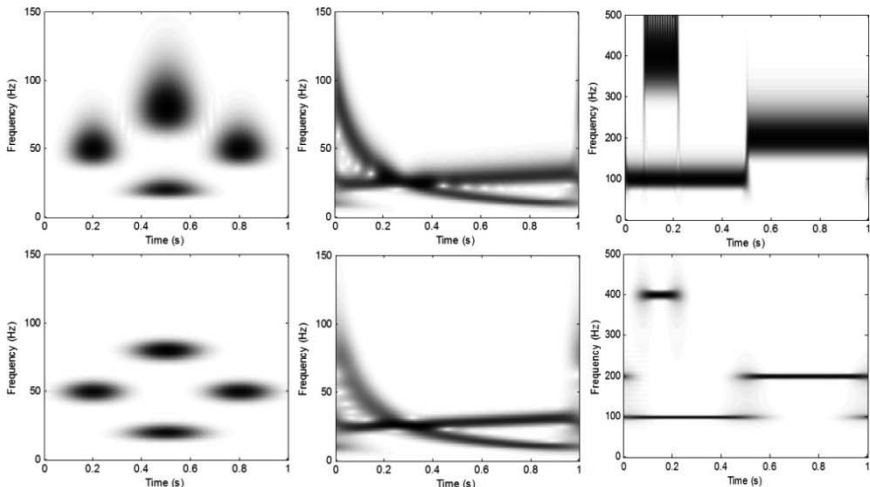


Figure 2.14. Comparison between the standard S-transform (top) and the proposed method with the parameters (m, p and k) selected with the GA (below)

Figure 2.15 shows the advantages of applying the GA to generate the Gaussian window parameters.

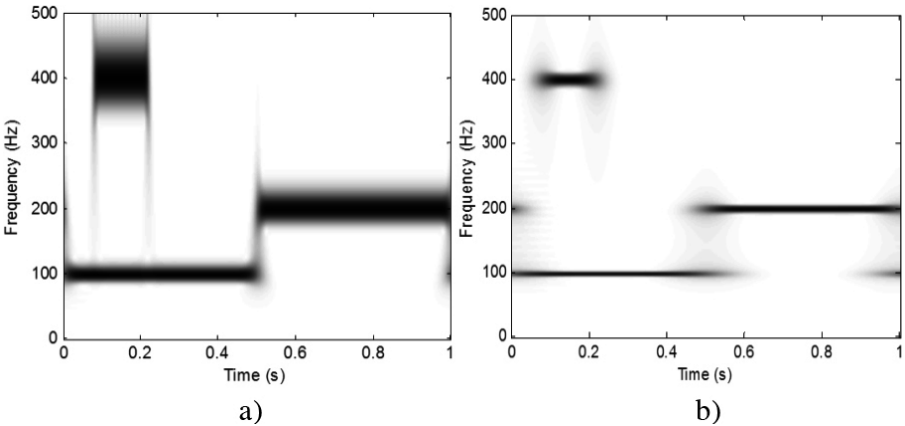


Figure 2.15. The Assous *et al.* window with the mentioned empirical parameters (without GA optimization) on $x_1(t)$: $m = 2.28$ equal to four times the variance of the signal k equals $k=1/N = 0.001$
a). The proposed method with $m = 0.98$, $p = 0.36$ and $k = 2.36$ b)

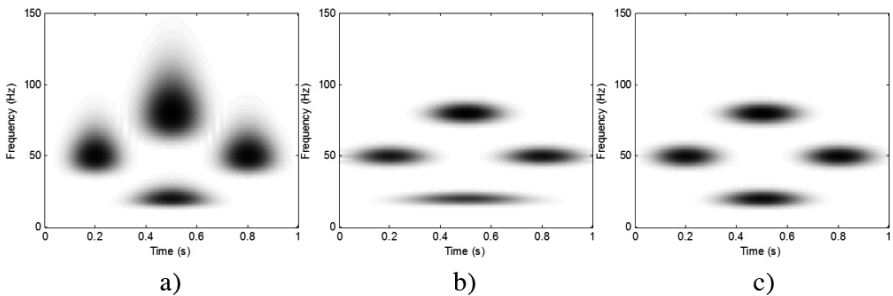


Figure 2.16. On $x_2(t)$, comparison between the standard S-transform a), Sejdic's *et al.* method with $r = 0.7$ b) and the proposed method with $m = 0.41$, $p = 0.51$ and $k = 0.029$ c)

Figure 2.16 shows the energy concentration compromise performed by the proposed method at all frequency levels, which is not the case with the standard or Sejdic's methods (poor time resolution for lower frequencies).

Figure 2.17 shows the contribution of the proposed parameter p to the enhancement of the energy concentration of S-transform. Compared to Assous *et al.*'s method, this provides more flexibility and can be considered more suitable for signals that contain nonlinear frequency components.

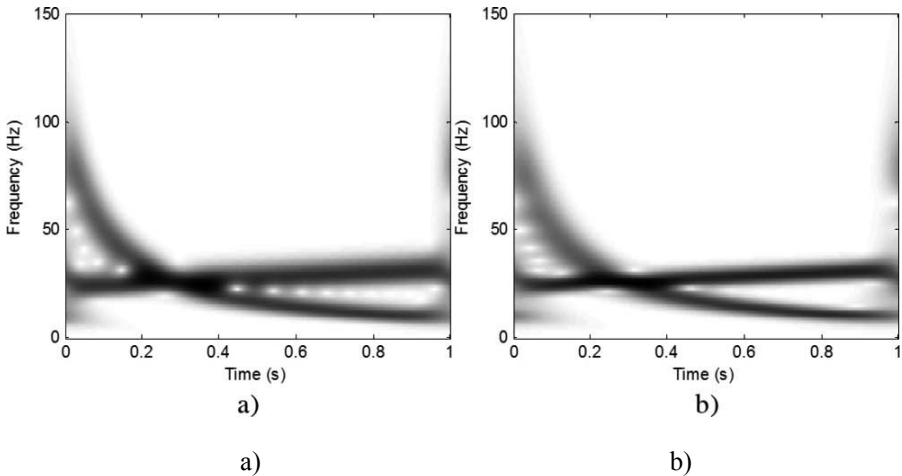


Figure 2.17. The Assous et al. window optimized with the GA on $x_3(t)$: $m = 0.025$ and $k = 0.5$ a). The proposed method with $m = 0.1$, $p = 0.72$ and $k = 0.5$ b)

The new window is more flexible hence more adaptive to the analyzed signal. The concentration energy measure clearly shows a large improvement in the case of the proposed method (Table 2.1).

CM	Standard	Sejdic et al.	Ass.+GA	Proposed
$x_1(t)$	0.0028	0.0053	0.0053	0.0053
$x_2(t)$	0.0073	0.0078	0.0078	0.008
$x_3(t)$	0.0057	0.0061	0.0061	0.0064
$x_4(t)$	0.0118	0.0118	0.0133	0.0136

Table 2.1. The concentration energy measures (CM) applied to the synthetic signals (x_1 , x_2 and x_3) and real signal (x_4) (see section 4.2) with different windows and methods proposed in the literature (standard S-transform, Sejdic’s et al. method, Assous et al. with the proposed GA optimization method (Ass.+GA) and the proposed method)

2.7.4. The ST-spectrogram

A normal transition between the ST that is a linear transform and the corresponding TF energy distribution is the square of the magnitude of the S-matrix called the ST-spectrogram [CHE 10, MOU 13], which is a quadratic transform. The

ST-spectrogram can be considered as a variation of Cohen's class distributions with a frequency-dependent kernel function [CHE 10]. It verifies the non-negativity property that is desirable for a physical interpretation and makes the famous Shannon entropy complexity measure [SHA 48] possible, which is not the case of the WVD for example.

Considering the squared modulus of the S-transform or the ST-spectrogram, the energy distribution of the signal is obtained in the TF plane. The ST-spectrogram is given as:

$$\begin{aligned} |S_x(t, f)|^2 &= \left| \int_{-\infty}^{+\infty} x(\tau) w(\tau-t) e^{-2\pi f \tau} d\tau \right|^2 \\ &= S_x(t, f) \cdot S_x^*(t, f) \end{aligned} \quad [2.47]$$

2.7.4.1. Relation with Cohen's class

The relation with Cohen' class can be given as [CHE 10]:

$$\begin{aligned} &= \iint_{-\infty}^{\infty} x(\tau) w(\tau-t) x^*(\tau) w^*(\tau-t') e^{-j2\pi f(\tau-\tau')} d\tau d\tau' \\ &= \iiint_{-\infty}^{\infty} x(u + \frac{1}{2}t) x^*(u - \frac{1}{2}t) \phi(\theta, t, f) e^{-j\theta t} e^{-jtf} e^{iu\theta} du dt d\theta \end{aligned}$$

where the frequency-dependent kernel function ϕ is given as:

$$\phi(\theta, t, f) = e^{-j\pi t \theta} \int_{-\infty}^{+\infty} w\left(\frac{u}{f}\right) w^*\left(\frac{u-\theta}{f}\right) e^{j2\pi tu} du$$

PROOF.–

$$\begin{aligned} |S_x(t, f)|^2 &= \left| \int_{-\infty}^{+\infty} x(\tau) w(\tau-t) e^{-2\pi f \tau} d\tau \right|^2 \\ &= S_x(t, f) \cdot S_x^*(t, f) \\ &= \iint_{-\infty}^{\infty} x(\tau) w(\tau-t) x^*(\tau) w^*(\tau-t') e^{-j2\pi f(\tau-\tau')} d\tau d\tau' \end{aligned}$$

Let $\tau = u + v/2$ and $\tau' = u - v/2$

$$\begin{aligned} &= \iint_{-\infty}^{\infty} x(u + v/2)x^*(u - v/2)w(u + v/2 - t)w^*(u - v/2 - t)e^{-j2\pi f} dv du \\ &= F_{v \rightarrow f} \left\{ (x(t + v/2)x^*(t - v/2)) \otimes_t (w(v/2 - t)w^*(-v/2 - t)) \right\} \\ &= F_{v \rightarrow f} \left\{ (x(t + v/2)x^*(t - v/2)) \otimes_t \Phi^{ST}(t, v; f) \right\} \end{aligned}$$

where $F_{v \rightarrow f}$ is the Fourier transform related to the variable v and \otimes_t is the convolution operator related to the variable t .

The time lag $\Phi^{ST}(t, v; f)$ is the Fourier transform of the kernel function. Hence, the kernel function $\phi(\theta, v, f)$ can be obtained as:

$$\begin{aligned} \phi^{ST}(\theta, v, f) &= F_{t \rightarrow \theta}^{-1} \left\{ \Phi^{ST}(t, v; f) \right\} \\ &= \frac{|f|}{2\sqrt{\pi}} e^{-((r^2 f^2/4) + (\pi^2 \theta^2/f^2))} \end{aligned}$$

2.7.4.2. Total energy

As for the S-transform, the ST-spectrogram can be considered as an amplitude conservative transform. However, it does not satisfy the energy-conservation property. This is due to the normalization process applied to the Gaussian window function to ensure the invertibility of the transform.

To show this mathematically, it will be appropriate to introduce the energy conservation property for the TF domain first.

A TFR that conserves the energy should verify the following equality:

$$\iint_{-\infty}^{\infty} C_x(t, f) dt df = E_x$$

where C_x are the coefficients of the TF domain. Because of Parseval's theorem, the energy of the signals can be written as:

$$E_x = \int_{-\infty}^{+\infty} |x(t)|^2 dt = \int_{-\infty}^{+\infty} |X(f)|^2 df$$

Therefore, for the ST-spectrogram, we have to calculate the $\iint_{-\infty}^{\infty} |S_x(t, f)|^2 dt df$ quantity. By decomposing the ST-spectrogram, this quantity can be written as:

$$\begin{aligned}
\iint_{-\infty}^{\infty} |S_x(t, f)|^2 dt df &= \iint_{-\infty}^{\infty} \{S_x(t, f) S_x^*(t, f)\} dt df \\
&= \int_{-\infty}^{+\infty} \dots \int_{-\infty}^{+\infty} x(\tau) w(\tau - t) x^*(\tau') w^*(\tau' - t) e^{-j2\pi f(\tau - \tau')} d\tau d\tau' dt df \\
&= \int_{-\infty}^{+\infty} \dots \int_{-\infty}^{+\infty} x(\tau) x^*(\tau') w(\tau - t) w^*(\tau' - t) \delta(\tau - \tau') d\tau d\tau' dt \\
&= \iint_{-\infty}^{\infty} |x(\tau)|^2 |w(\tau - t)|^2 d\tau dt
\end{aligned}$$

As can be seen from the above equation, the ST-spectrogram does not satisfy the energy-conservation property since:

$$\begin{aligned}
\iint_{-\infty}^{\infty} |S_x(t, f)|^2 dt df &\neq \int_{-\infty}^{+\infty} |x(t)|^2 dt \\
&\neq E_x
\end{aligned}$$

The window function must be normalized in order to have an invertible S-transform as follows:

$$\int_{-\infty}^{+\infty} w(t, f) dt = 1 \quad \forall f \in \mathbb{R}$$

However, this non-property allows the ST-spectrogram to be amplitude conservative as has been shown before.

2.7.4.3. Complexity measures

The concept of complexity takes a quantitative meaning here. Thus, signals of high complexity (and therefore high information content) must be constructed from large numbers of elementary components [BAR 01]. The TF complexity measures aim at quantifying the complexity of the signal via the TFR and not directly via the signal. In this case, the TFR plays an analogous role such as a 2D probability density function (PDF) [BAR 01]. However, not all TFRs can be considered strictly as PDF; for example, Cohen's class, which generalized all quadratic TFRs, cannot satisfy both the time marginal property and the non-negativity simultaneously [WIG 32]. Nevertheless, it does not preclude applying complexity measures based on Cohen's TFRs planes, especially when it could prove more appropriate for certain classes of signal.

As has been shown, the ST-spectrogram can be considered as a variation of Cohen's class distributions with a frequency-dependent kernel function. It verifies

the non-negativity property, which is desirable for physical interpretations, and makes the famous Shannon entropy complexity measure [SHA 48] possible, which is not the case of the WVD for example [BAR 01].

– *Normalized Shannon entropy*

The Shannon entropy is a natural candidate for measuring the complexity of a signal through TFRs. It is applicable to the ST-spectrogram coefficients (C_x) since the ST-spectrogram verifies the non-negativity condition. The Shannon entropy is defined as follows:

$$H(C_x) = - \iint_{-\infty}^{\infty} C_x(t, f) \log_2 C_x(t, f) dt df \quad [2.48]$$

To normalize the Shannon entropy, we first have to normalize the coefficients of the ST-spectrogram as follows:

$$C_x^{norm}(t, f) = \frac{C_x(t, f)}{\iint_{-\infty}^{\infty} C_x(u, v) du dv}$$

The maximum of Shannon entropy that corresponds to equiprobable events can be given as:

$$H_{\max}(C_x^{norm}) = \log_2(n \times m)$$

where n is the sample number of the signal $x(t)$, m is the number of frequency voices used to calculate the ST-spectrogram and $n \times m$ is the total number of coefficients in the $C_x^{norm}(t, f)$ distribution. Therefore, the normalized Shannon entropy can be given as [MOU 13]:

$$H_{norm}(C_x^{norm}) = \frac{H(C_x^{norm})}{\log_2(n \times m)} \quad [2.49]$$

A real application of the Shannon entropy measure based on the ST-spectrogram will be presented in Chapter 3 and consists of detecting pathologic heart sounds with systolic murmurs, which can be considered as signals with a higher complexity than the normal ones.

2.8. Conclusion

This chapter introduced some linear and bilinear TFRs, focusing on the S-transform, which is a linear transformation and can be viewed as a hybrid version between the STFT and the WT. Theoretical characteristics of the S-transform have been explored and an energy concentration enhancement strategy has been proposed and compared with existing methods in the literature. The complexity measure via the TF plane based on the ST-spectrogram (Shannon entropy) is also proposed.

This chapter will lead us to introduce the first application of this book regarding the segmentation and classification of heart sounds based on the S-transform.

2.9. Bibliography

- [AND 01] ANDINO S., MENENDEZ R., LANTZ C., *et al.*, “Nonstationary distributed source approximation: an alternative to improve localization procedures”, *Human Brain Mapping*, vol. 14, pp. 81–95, 2001.
- [ASO 06] ASSOUS S., HUMEAU A., TARTAS M., *et al.*, “S-transform applied to laser doppler flowmetry reactive hyperemia signals”, *IEEE Transactions on Biomedical Engineering*, vol. 53, pp. 1032–1037, 2006.
- [ASO 12] ASSOUS S., BOASHASH B., “Evaluation of the modified S transform for time-frequency synchrony analysis and source localization”, *EURASIP Journal on Advances in Signal Processing*, vol. 49, 2012.
- [AUG 96] AUGER F., FLANDRIN P., GONCALVÈS P., *et al.*, *Time-Frequency Toolbox*, Tutorial, CNRS (France) and Rice University (USA), 26 October 2005.
- [BAR 01] BARANIUK R.G., FLANDRIN P., JANSSEN A.J.E.M., *et al.*, “Measuring time-frequency information content using the Rényi entropies”, *IEEE Transactions on Information Theory*, vol. 47, no. 4, pp. 1391–1409, May 2001.
- [CHE 10] CHENG L., *et al.*, “Estimation of time-varying coherence and its application in understanding brain functional connectivity”, *EURASIP Journal on Advances in Signal Processing*, 2010. Doi:10.1155/2010/390910
- [COH 66] COHEN L., “Generalized phase-space distribution functions”, *Journal of Mathematical Physics*, vol. 7, no. 5, pp. 781–786, May 1966.
- [COH 95] COHEN L., *Time-Frequency Analysis*, Prentice Hall PTR, Englewood Cliffs, NJ, 1995.
- [CHO 89a] CHOI H., WILLIAMS W., “Improved time-frequency representation of multicomponent signals using exponential kernels”, *IEEE Transactions on Acoustics, Speech and Signal Processing*, vol. 37, no. 6, pp. 862–871, 1989.

- [COH 89b] COHEN L., “Time-frequency distributions – a review”, *IEEE Proceedings*, vol. 77, no. 7, pp. 941–981, 1989.
- [DAS 03] DASH P., PANIGRAHI, B., PANDA G., “Power quality analysis using S-transform”, *IEEE Transactions on Power Delivery*, vol. 18, pp. 406–411, 2003.
- [DAU 92] DAUBECHIES I., *Ten Lectures on Wavelets*, CBMS-NSF Regional Conference Series in Applied Mathematics, Academic Press, 1992.
- [GAB 46] GABOR D., “Theory of communications”, *Journal of the Institution of Electrical Engineers*, vol. 93, pp. 429–457, 1946.
- [GIB 06] GIBSON P.C., LAMOUREUX M.P., MARGRAVE G.F., “Letter to the editor: Stockwell and wavelet transforms”, *Journal of Fourier Analysis and Applications*, vol. 12, no. 6, pp. 713–721, December 2006.
- [GOU 84] GOUPILLAUD P., GROSSMANN A., MORLET J., “Cycle-octave and related transforms in seismic signal analysis”, *Geoexploration*, vol. 23, pp. 85–102, 1984.
- [GRO 01] GROCHENIG K., *Foundations of Time-Frequency Analysis*, Birkhäuser, Boston, MA, 2001.
- [HLA 92] HLAWATSCH F., BOUDREAUX-BARTELS G., “Linear and quadratic time-frequency signal representations”, *IEEE Signal Processing Magazine*, vol. 9, no. 2 pp. 21–67, 1992.
- [HOL 75] HOLLAND J.H., *Adaptation in Natural and Artificial Systems*, The University of Michigan Press, Ann Arbor, MI, 1975.
- [JEO 92] JEONG J., WILLIAMS W.J., “Kernel design for reduced interference distributions”, *IEEE Transactions on Signal Processing*, vol. 40, no. 2, pp. 402–412, 1992.
- [KUM 10] KUMSAWAT P., “A genetic algorithm optimization technique for multiwavelet-based digital audio watermarking”, *EURASIP Journal on Advances in Signal Processing*, vol. 2010, p. 10, 2010. Doi:10.1155/2010/471842.
- [LOU 94] LOUGHLIN P.J., *et al.*, “Construction of positive time-frequency distributions”, *IEEE Transactions on Signal Processing*, vol. 42, no. 10, pp. 2697–2705, October 1994.
- [MAL 99] MALLAT S., *A Wavelet Tour of Signal Processing*, Academic Press, 1999.
- [MAN 97] MANSINHA L., STOCKWELL R.G., LOWE R.P., *et al.*, “Local S-Spectrum Analysis of 1-D and 2-D Data”, *Physics of the Earth and Planetary Interiors*, vol. 103, pp. 329–36, 1997.
- [MCF 99] MCFADDEN P.D., COOK J.G., FORSTER L.M., “Decomposition of gear vibration signals by the generalized S-transform”, *Mechanical Systems and Signal Processing*, vol. 13, no. 5, pp. 691–707, 1999.
- [MEI 12] MEI C.H., SHAAMARI A.Z., BOUASHASH B., “Efficient phase estimation for the classification of digitally phase modulated signals using the cross WVD: a performance evaluation and comparison with the S-transform”, *Eurasip Journal on Advances in Signal Processing*, vol. 65, 2012.

- [MOU 12] MOUKADEM A., DIETERLEN A., BRANDT C., “A robust heart sound segmentation module based on S-transform”, *Biomedical Signal Processing and Control*, vol. 8, pp. 273–281, 10.1016/j.bspc.2012.11.008.
- [MOU 13] MOUKADEM A., DIETERLEN A., BRANDT C., “Shannon entropy based on S-transform spectrogram. Applied on the classification of heart sounds”, *IEEE Conference on Acoustics, Speech, and Signal Processing (ICASSP 2013)*, Vancouver, Canada, 26–31 May 2013.
- [PEI 10] PEI S., WANG P., “Energy concentration enhancement using window width optimization in S-transform”, *IEEE Conference on Acoustics, Speech, and Signal Processing (ICASSP 2010)*, 2010.
- [PIN 03a] PINNEGAR C.R., MANSINHA L., “The S-transform with window of arbitrary and varying shape”, *Geophysics*, vol. 68, no. 1, pp. 381–385, 2003.
- [PIN 03b] PINNEGAR C.R., MANSINHA L., “The Bi-Gaussian S transform”, *SIAM Journal on Scientific Computing*, vol. 24, no. 5, pp. 1678–1692, 2003.
- [PIN 04] PINNEGAR C.R., MANSINHA L., “Time-local Fourier analysis with a scalable, phase-modulated analyzing function: the S-transform with a complex window”, *Signal Processing*, vol. 84, pp. 1167–1176, July 2004.
- [PIN 09] PINNEGAR C.R., KHOSRAVANI H., FEDERIC P., “Time–frequency phase analysis of Ictal EEG recordings with the S-transform”, *IEEE Transactions on Biomedical Engineering*, vol. 56, no. 11, pp. 2583–2593, November 2009.
- [RED 12] REDDY M.J.B., *et al.*, “Power quality analysis using discrete orthogonal S-transform (DOST)”, *Digital Signal Processing*, vol. 23, pp. 616–626, 2012. Available at <http://dx.doi.org/10.1016/j.dsp.2012.09.013>.
- [SCH 05] SCHIMMEL M., GALLART J., “The inverse S-transform in filters with time-frequency localization”, *IEEE Transactions on Signal Processing*, vol. 53, no. 11, pp. 4417–4422, November 2005.
- [SEJ 07] SEJDIC E., *et al.*, “Selective regional correlation for pattern recognition”, *IEEE Transactions on Systems, Man, and Cybernetics—Part A: Systems and Humans*, vol. 37, no. 1, pp. 82–93, January 2007.
- [SEJ 08] SEJDIC E., DJUROVIC I., JIANG J., “A window width optimized S-transform”, *EURASIP Journal on Advances in Signal Processing*, vol. 2008, p. 13, 2008. Doi:10.1155/2008/672941.
- [SEJ 09] SEJDIC E., DJUROVIC I., JIANG J., “Time–frequency feature representation using energy concentration: an overview of recent advances”, *Digital Signal Processing*, vol. 19, pp. 153–183, 2009.
- [SHA 48] SHANNON C.E., “A mathematical theory of communication-part 1”, *Bell System Technical Journal*, vol. 27, pp. 379–423, July 1948.
- [SIM 07] SIMON C., VENTOSA S., SCHIMMEL M., *et al.*, “The S-transform and its inverses: side effects of discretizing and filtering”, *IEEE Transactions on Signal Processing*, vol. 55, no. 10, pp. 4928–4937, October 2007.

- [STA 01] STANKOVIC L., “A measure of some time-frequency distributions concentration”, *Signal Processing*, vol. 81, no. 3, pp. 621–31, 2001.
- [STO 96] STOCKWELL R.G., MANSINHA L., LOWE R.P., “Localization of the complex spectrum: the S transform”, *IEEE Transactions on Signal Processing*, vol. 44, no. 4, pp. 998–1001, 1996.
- [STO 01] STOCKWELL R., LOWE R., “Aiglow imaging of gravity waves 1. Results from a small network of OH nightglow scanning imagers”, *Journal of Geophysical Research-Atmospheres*, vol. 106, pp. 17185–17203, 2001.
- [STO 07a] STOCKWELL R., “A basis for efficient representation of the S-transform”, *Digital Signal Processing*, vol. 17, pp. 371–393, 2007.
- [STO 07b] STOCKWELL R.G., “Why use the S-transform?”, *Pseudo-Differential Operators: Partial Differential Equations and Time-Frequency Analysis, Fields Institute Communications*, vol. 52, American Mathematical Society, Providence, RI, pp. 279–309, 2007.
- [SUC 11] SUCIC V., SAULIG N., BOASHASH B., “Estimating the number of components of a multicomponent nonstationary signal using the short-term time-frequency Rényi entropy”, *EURASIP Journal on Advances in Signal Processing*, vol. 125, 2011.
- [TAN 96] TANG K.S., MAN K.F., KWONG, S., et al., “Genetic algorithms and their Applications”, *IEEE Signal Processing Magazine*, vol. 13, pp. 22–37, November 1996.
- [VEN 08] VENTOSA S., SIMON C., SCHIMMEL M., et al., “The S-transform from a wavelet point of view”, *IEEE Transactions on Signal Processing*, vol. 56, no. 7, pp. 2771–2780, July 2008.
- [VET 95] VETTERLI M., KOVACEVIC J., *Wavelets and Subband Coding*, Prentice-Hall, Englewood Cliffs, NJ, 1995.
- [VIL 48] VILLE J., “Théorie et applications de la notion du signal analytique”, *Cables et Transmissions*, vol. 2A, pp. 61–74, 1948.
- [WAN 09] WANG Y., ORCHARD J., “Fast discrete orthonormal Stockwell transform”, *SIAM Journal on Scientific Computing*, vol. 31, no. 5, pp. 4000–4012, 2009.
- [WIG 32] WIGNER E., “On the quantum correction for thermodynamic equilibrium”, *Physical Review*, vol. 40, no. 5, pp. 749–759, 1932.
- [WIL 89] WILLIAMS W.J., JEONG J., “New time-frequency distributions: theory and applications”, *Proceedings of IEEE International Symposium on Circuits and Systems*, vol. 2, Portland, OR, pp. 1243–1247, 8–11 May 1989.
- [WIL 91] WILLIAMS W.J., BROWN M.L., HERO A.O., “Uncertainty, information, and time-frequency distributions”, *Proceedings of the SPIE International Society for Optical Engineering*, vol. 1566, pp. 144–156, 1991.

Segmentation and Classification of Heart Sounds Based on the S-Transform

This chapter presents a first application of this book, which is the analysis of heart sounds. Heart sounds and auscultation are non-invasive, low cost and accurate for diagnosing some heart diseases. A new module for the segmentation of heart sounds based on the S-transform is proposed. The heart sound segmentation process divides the phonocardiogram (PCG) signal into four parts: S1 (first heart sound), systole, S2 (second heart sound) and diastole. It can be considered one of the most important phases in the auto-analysis of PCG signals. A segmentation method based on the Shannon energy (SE) of the local spectrum calculated by the S-transform is proposed. Then, the energy concentration of the S-transform is optimized to accurately detect the boundaries of the localized sounds. New features based on the energy concentration of the S-transform are proposed to classify S1 and S2, and other features based on the complexity measure via time–frequency (TF) domain are proposed to detect systolic murmurs. These methods are validated on real signals collected in real-life conditions.

3.1. Introduction

The advancement of technology has paved the way for signal processing methods to be implemented and applied in many simple tools useful in everyday life. This is most notable in the medical technology field, where contributions involving intelligent applications have boosted the quality of diagnosis. Proposing an objective signal processing method able to extract relevant information from biosignals is a great challenge in the telemedicine and autodiagnosis fields. For the cardiac system, many signals can be treated and monitored; i.e. electrocardiogram (ECG), PCG and echo/Doppler and pressure monitor.

This chapter is basically focused on PCG signals. PCG and auscultation are non-invasive, low cost and accurate for diagnosing some heart diseases. The PCG signal confirms and, mostly, refines the auscultation data, and provides further

information about the acoustic activity concerning the chronology of the pathological signs in the cardiac cycle, by locating them with respect to the normal heart sounds. The cardiac sounds are by definition non-stationary signals and are located within the low-frequency range, approximately between 10 and 750 Hz.

The analysis of the cardiac sounds, solely based on the human ear, remains insufficient for a reliable diagnosis of cardiac pathologies, and for a clinician to obtain all the qualitative and quantitative information about cardiac activity especially in the field of time intervals. All the information, such as the temporal localization of the heart sounds, the number of their internal components, their frequency content and the significance of diastolic and systolic murmurs, can be studied directly on the PCG signal. To recognize and classify cardiovascular pathologies, advanced methods and techniques of signal processing and artificial intelligence will be used. In this respect, different approaches could be considered to improve the electronic stethoscope:

- Tools providing embedded autonomous analysis, easy to use by the general public at home for autodiagnosis, monitoring and warning, if needed.
- Tools providing sophisticated analysis (coupled to a PC, Bluetooth link) for the use of professionals in order to make an in-depth medical diagnosis and to train medical students.

In the last 20 years, many studies have shown interest in the PCG signal processing field (see Figure 3.1); for the denoising of the PCG, many advanced tools of signal processing are used such as the Kalman filter [CHA 97], wavelets [MES 01] and, more recently, the empirical modal decomposition (EMD) [BEY 09]. For the TF representation (TFR) of the PCG signal, the famous short-time Fourier transform (STFT) [DJE 00], the continuous wavelet transform (CWT) [DEB 08], the S-transform [SEJ 04] and the Wigner–Ville distribution (WVD) [BOU 11, DJE 13] are used. For the segmentation process, the methods can be classified depending on the domain in which they are applied: time domain (SE [LIA 97]), frequency domain (homomorphic filter [GUP 07]), TF domain (wavelet transform [MOU 04], S-transform [MOU 13]) and nonlinear domain (radial basis function [MOU 11b]). For the classification of heart sounds, artificial neural networks (ANN) [SIN 07, LIJ 12], K-nearest neighbors (KNN) [VEP 09] and support vector machines (SVM) [MAG 09] are used.

Whatever the approach, one of the first and most important phases in the analysis of heart sounds is the segmentation of heart sounds. Heart sound segmentation partitions the PCG signals into cardiac cycles and further into S1 (first heart sound), systole, S2 (second heart sound) and diastole. Identification of the two phases of the cardiac cycle and of the heart sounds with robust differentiation between S1 and S2 even in the presence of additional heart sounds and/or murmurs is a first step in this

challenge. Then, there is a need to measure accurately S1 and S2 allowing the progression to automatic diagnosis of heart murmurs with the distinction of ejection and regurgitation murmurs. This phase of autonomous detection, without the help of ECG, is based on signal processing tools such as: SE [LIA 97], the Hilbert transform [CHO 06], high-order statistics [AHL 08] and a hidden Markov model [SCH 10].

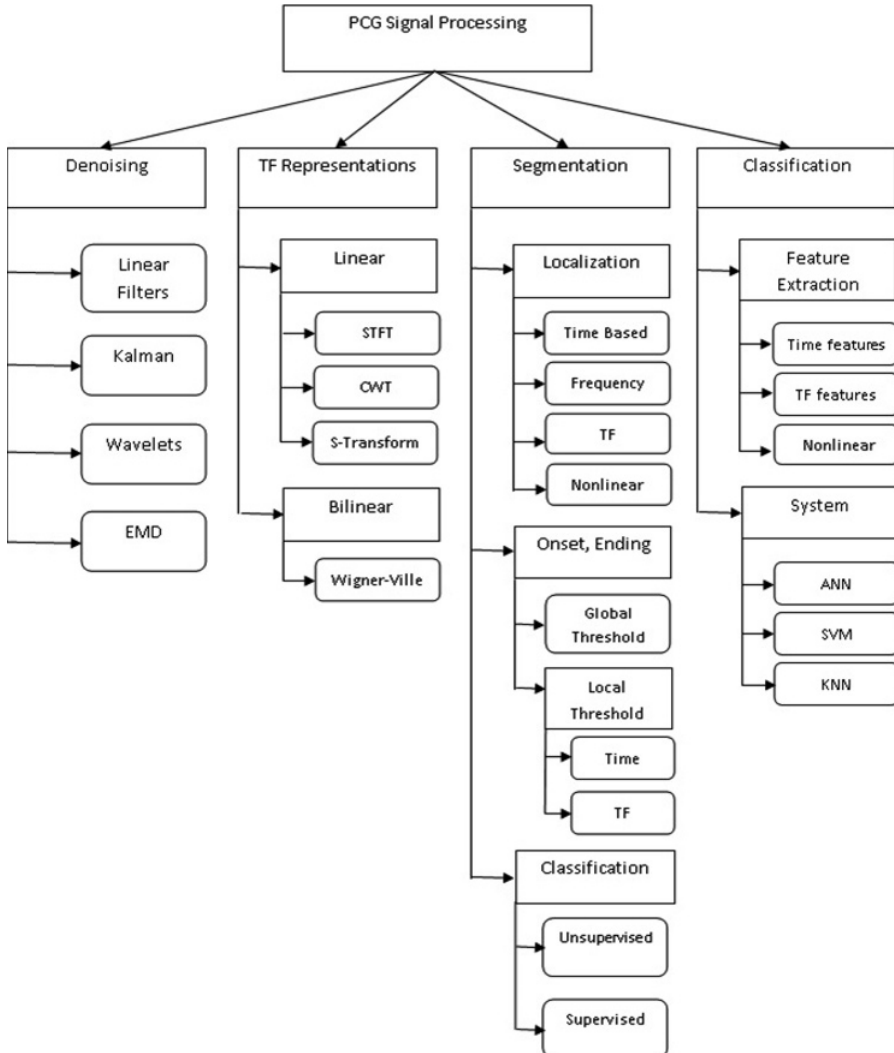


Figure 3.1. An overview of the different contributions existing in the literature concerning the PCG signal processing algorithms and methods

In this chapter, we present a new method for heart sound segmentation based on TF analysis (S-transform) and new features extracted from the TF domain are investigated for the classification of S1 and S2 and for the detection of systolic murmurs.

The aim of this study is to develop a generic tool that is suitable for clinical and home monitoring use, robust to noise and applicable to diverse pathological and normal heart sound signals without the necessity of any previous information about the subject. The proposed methods are evaluated based on databases containing real signals. This study has been conducted under the guidance of an experienced cardiologist, with the aim of validating the results of each method.

This chapter is organized as follows: section 3.2 describes the database used in this study and the different methods proposed for the PCG signal processing. It is followed by section 3.3, which presents the results and discussion. Finally, section 3.4 gives the future research and the conclusion.

3.2. Methods and materials

3.2.1. Data sets

3.2.1.1. Data set 1

Several factors affect the quality of the acquired signal, above all the type of the electronic stethoscope, its mode of use, the patient's position during auscultation and the surrounding noise [AHL 08]. According to the cardiologist's experience, it is preferable that the signals remain unrefined; filtration will only be applied subsequently for the purpose of signal analysis. For this reason, a prototype stethoscope produced by Infral Corporation is used which comprises an acoustic chamber in which a sound sensor is inserted. Electronic devices for signal conditioning and amplification are inserted in a case along with a Bluetooth standard communication module.

Different cardiologists equipped with a prototype electronic stethoscope have contributed to a campaign of measurements at the Hospital of Strasbourg, France. In parallel, two prototypes have been dedicated to the MARS500 project promoted by European space agency (ESA), in order to collect signals from six volunteers (astronauts). The use of prototype electronic stethoscopes by different cardiologists makes the database rich in terms of the qualitative diversity of collected sounds, which in turn makes the heart sound localization more realistic. The sounds are recorded with 16 bit accuracy and a 8,000 Hz sampling frequency in a wave format, using the “Stetho” software developed under an Alcatel-Lucent license.

The data set contains 80 subjects, including 40 cardiac pathology sounds, which contain different systolic murmurs. Each subject corresponds to one recording sound. The length of each sound is 8 s. This data set will be used in this study to validate the proposed segmentation method and to perform a comparison study with the existing methods in the literature.

3.2.1.2. Data set 2

In this chapter, new features to classify the first and second heart sounds are proposed. The challenge is to classify S1 and S2 accurately even in the presence of a high level of noise (ambient, respiratory, acquisition noises, etc.) and when the classic systolic and diastolic duration criteria (S/D-ratio) will no longer be valid due to pathological cases (tachycardia) or cardiac stress tests, for example. To this end, heart sounds are collected from subjects under cardiac stress from healthy subjects from the Department of Health Science and Technology, Aalborg University, Denmark [RØN 11].

Nine healthy subjects were enrolled in the study ($M = 5$, $F = 4$), with a median age of 32 (24–36) years. Informed consent was retrieved from all subjects prior to the exercise test. A Panasonic microphone was incorporated into a coupler, specially designed by the Department of Acoustics at Aalborg University. The microphone detected the mechanical pressure differences in the coupler, caused by alterations of the sound pressure. The microphone recorded with a frequency of 48,000 Hz. The heart sound recordings were synchronized with a three-lead ECG. The microphone was fitted to the third left intercostal space with a specially designed double adhesive plaster. Subsequently, the subject cycled on a Monark Ergometric 894E ergometer bicycle. The workload was increased by 25 W every 2 min with an initial workload of 25 W. The subject cycled until subjective maximum endurance was reached. Afterwards, subjects who did not reach 80% of the maximum heart rate defined as 220 minus age \pm 12 were excluded from the study. Recordings of heart sounds were made for 10 s at the end of each workload level. The Acarix Data Acquisition System was used for recording the heart sounds and ECG [HAN 11].

3.2.2. Localization and segmentation of heart sounds

3.2.2.1. Preprocessing

First, the original signal is decimated by factor 4 from a 8,000 to 2,000 Hz sampling frequency and then the signal is filtered by a high-pass filter with a cutoff frequency of 30 Hz, to eliminate the noise collected by the prototype stethoscope. The filtered signal is refiltered in reverse direction so that there is no time delay in

the resulting signal. Then, the normalization is applied by setting the variance of the signal to a value of 1. The resulting signal is expressed by:

$$x_{norm}(t) = \frac{x(t)}{|\max(x(t))|} \quad [3.1]$$

The localization algorithms operating on PCG data try to emphasize heart sound occurrences with an initial transformation that can be classified into three main categories: frequency-based transformation, morphological transformations and complexity-based transformations [AHL 08].

The transformation tries to maximize the distance between the heart sounds and the background noise, and the result is smoothed and thresholded in order to apply a peak detector algorithm. Here, we note that the main goal of heart sound localization is to locate the first and second heart sounds but without distinguishing the two from each other and without detecting the boundaries of located sounds.

3.2.2.2. *S-transform Shannon envelope (SSE) localization method (SSE envelope)*

A new method for the localization of heart sounds is proposed in this study (SSE). It uses the S-transform of the heart sound in the frequency band 0–100 Hz and calculates the SE of the local spectrum calculated by the S-transform for each sample of the signal $x(t)$. Then, the extracted envelope is smoothed by applying an average filter.

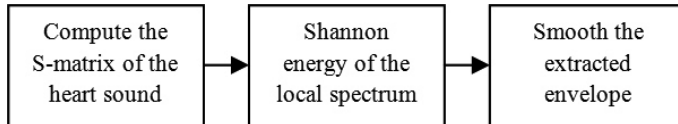


Figure 3.2. Block diagram of SSE method

The proposed SSE method calculates the SE of each column of the extracted S-matrix as follows:

$$SSE(x_i) = - \int_{-\infty}^{+\infty} |S_x(\tau, f)|^n \log(|S_x(\tau, f)|^n) df \quad [3.2]$$

where $S_x(\tau, f)$ is the S-transform of the signal $x(t)$:

$$S_x(\tau, f) = \int_{-\infty}^{+\infty} x(t)w(t - \tau, f)e^{-2\pi jft} dt$$

Each column of the S-matrix $S_x(\tau, f)$ represents the local spectrum at a specific sample. The advantage of the SE transformation is its capacity to emphasize the medium intensities and to attenuate low intensities of the signal, which represents the local spectrum in the case of the SSE method. The SSE envelope can be viewed as a modified (filtered) instantaneous frequency measure.

The parameter n in equation [3.2] is usually fixed to 2, which is the standard coefficient of the SE measure. The parameter n can be fixed to 1.5, for example, to enhance the detection of low-intensity sounds buried in noise. This occurs in heart sounds more often with S2 when the cardiac frequency is high (data set 2). Figure 3.3 shows the compromise of attenuation of low and high intensities, as a function of the value of n . Here, we note that for the SSE method, the intensities are the local spectrum coefficients of the S-transform and not the time sample intensities of the signal.

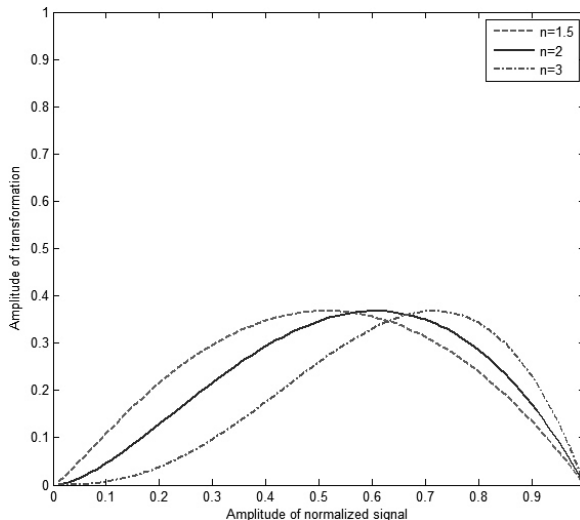


Figure 3.3. The envelope of normalized signal for values of $n = 1.5, 2$ and 3

3.2.2.3. Boundary detection algorithm: an optimized S-transform approach

The boundary detection algorithm aims at estimating the onset and the end point of the located heart sounds. Accurate boundary estimation is a very important step in the heart sound segmentation module and is essential for the extraction of meaningful features from each part of the heart cycle in order to perform an autodiagnosis process.

3.2.2.4. Overview of existing methods

Different boundary detection algorithms are present in the literature; Liang *et al.* [LIA 97] estimated the boundaries by applying a threshold on the extracted envelope of the signal, this may not be accurate for some cardiac cycles, because the envelope threshold level is used based on the average value of the whole recordings periods. The same authors proposed another algorithm that employs the STFT to explore the TF domain of the signal [LIA 98]. The authors quantified the spectrogram at each segment to two values by applying a threshold that reserves 60% of the signal energy; however, it is not clear how the energy of the signal is calculated and the accuracy of the algorithm is not mentioned. Samit *et al.* [SAM 06] used some biomedical features of heart sounds (S1 and S2) such as the maximum duration of S1 and S2 to determine the limit of estimated boundaries; the disadvantage of this method is that the estimation of energy of the signal is based on the time domain only, so in the presence of a high level of noise, the performance of this method will decrease dramatically.

3.2.2.5. The optimized S-transform Shannon envelope (OSSE) algorithm

In this chapter, we propose a new algorithm to estimate the heart sound boundaries. The proposed algorithm tries to optimize the energy concentration of the S-transform at each located sound by using a window width optimization method (see Chapter 2). The envelope of the optimized S-transform is then recalculated by using the SSE approach and an adaptive threshold is applied to determine the onset and ending of each located heart sound. Let us assume that L is the time located sounds after applying the localization method on the heart sound and $S(M,N)$ is the S-matrix of the heart sound where M represents the frequency domain and N is the time domain.

The block diagram of the proposed algorithm (OSSE) is shown in Figure 3.4.

1) Estimate the boundary limit

The boundary limits are estimated on the basis of the fact that the maximum duration of S1 and S2 is 150 ms [SCH 94]. So, a 150 ms window is applied in the proximity of detected S1 and S2 peaks, which covers 75 ms in the backward direction of the S1 or S2 peak and 75 ms in the forward direction.

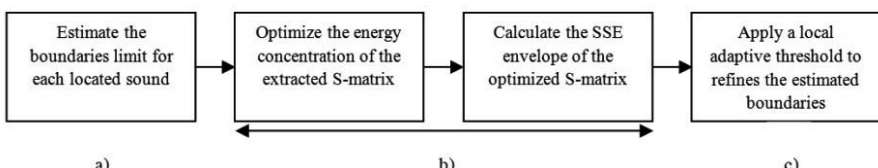


Figure 3.4. The block diagram of the OSSE method

2) Optimized S-transform

In Chapter 2, different Gaussian windows and strategies were proposed to enhance the energy concentration of the S-transform in TF domain. For the sake of simplicity, the window based on the parameter α is used (see Chapter 2):

$$w(\tau-t, f, \alpha) = \frac{|f|}{\alpha\sqrt{2\pi}} e^{\frac{-f^2(\tau-t)}{2\alpha^2}}$$

The concentration energy measure (CM) is calculated for set values chosen from a set; $0.5 < \alpha < 2$, with a step of 0.1 and for all located sounds (S1 and S2). The parameter α that maximized the $CM(\alpha)$ of sound S_i (S1 or S2) can be considered as optimal for this sound.

The energy concentration in the TF domain is a very important parameter for the algorithms that aim to detect the duration of any given events in a signal. Therefore, it should hold the same importance for the boundary detection algorithm of heart sounds based on TF features. However, in some cases, the S-transform suffers from poor energy concentration in the TF domain. Hence, an energy concentration optimization process is needed to improve the boundary estimation of the heart sounds.

3) The adaptive threshold

Performing an optimized S-transform before calculating the SSE envelope makes the choice of threshold less sensitive to the variation of different heart sounds. In this study, a threshold that equals 10% of the maximum value of the SSE envelope is applied to refine the estimated boundaries.

3.2.2.6. Split of the first and the second heart sounds

Optimization of the TFR of heart sounds can lead to more objective and reliable methods and diagnostics [MOU 13]. Figure 3.5 shows the enhancement of the TF concentration in the case of the proposed method applied on the first heart sound with split. This is very important since the split in the first heart sound cannot be detected clearly with the standard S-transform. The S1 heart sound is composed of two valvular sounds denoted as M1 and T1 generated by the closure of the mitral and the tricuspid valves, respectively. The split within the S1 and S2 heart sounds emerged as an indicator of several valvular diseases [DJE 13].

Figure 3.5 can be considered as another example that shows the importance of the representation optimization of the signal in TF domain.

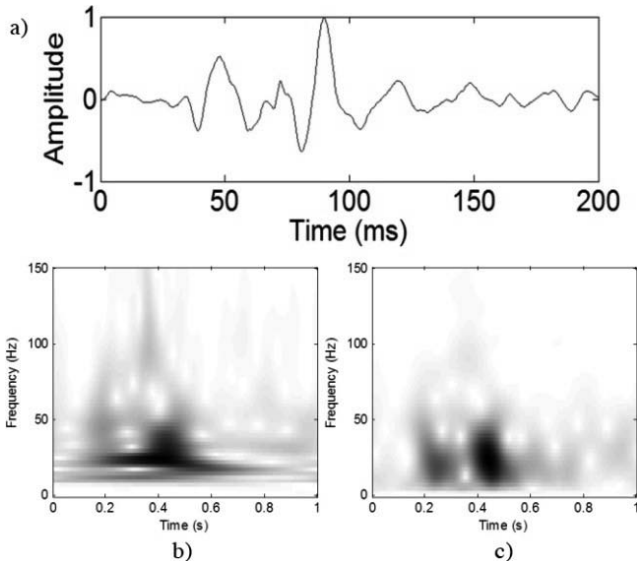


Figure 3.5. a) S1 sound extracted from real heart sound.
b) The standard S-transform. c) The proposed optimized S-transform with the parameters m , p and k (Chapter 2)

3.2.3. Classification of heart sounds

3.2.3.1. S1 and S2 classification

1) The Gaussian parameter α as discriminant feature

A new feature proposed in this chapter to discriminate S1 and S2 is the parameter α_{opt} (equation [3.3]) used to optimize the width of the Gaussian window of the S-transform. It is known from a physiological point of view that S1 is more complicated than S2. These physiological differences will necessarily lead to different TF content behavior, which we will aim to reveal with parameter α_{opt} .

$$\alpha_{opt} = \arg \max_{\alpha} (CM(\alpha)) \quad [3.3]$$

Figure 3.6 shows S1 and S2 signals examples with the corresponding optimized S-transform obtained with $\alpha = 0.8$ and 0.5 , respectively.

The parameters α_{opt} are calculated and compared for each S1 and S2 sounds in the database (2,636 sounds). The results are given in section 3.4.

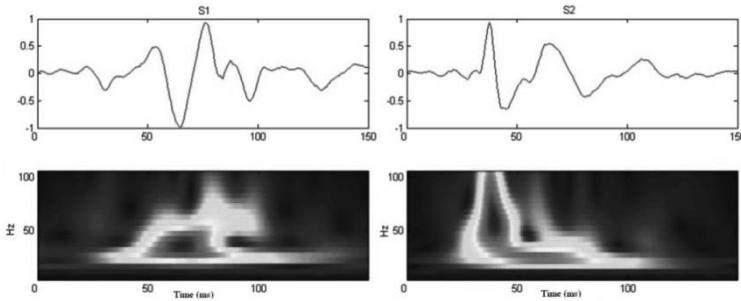


Figure 3.6. S1 and S2 signals (top). Optimized S-transform obtained with $\alpha = 0.8$ for S1 and $\alpha = 0.5$ for S2 (bottom)

2) The SSE envelope feature: β

A second feature investigated in this chapter, named β , aims to integrate the normalized SSE envelope over time and can be given as:

$$\beta = \int_{-\infty}^{+\infty} \left\{ \int_{-\infty}^{+\infty} |S_x(t, f)|^2 \log(|S_x(t, f)|^2) df \right\} dt \quad [3.4]$$

The SSE envelope estimates the frequency energy at the local spectrum of the signal. It can be considered as a modified instantaneous frequency measure. The β feature aims to reveal the frequency contribution of each sound over time. Mathematically, it can be viewed as the integration over time of a modified instantaneous frequency measure. Physically, this feature reveals in some way the shape morphology of the signal. The measure is computed from the normalized SSE envelope to avoid the influence of the amplitude variations.

Figure 3.7 shows an example of the β feature calculated on S1 and S2 sounds from their normalized SSE envelopes.

3.2.3.2. Murmurs detection: normalized Shannon entropy

Heart murmurs usually result from turbulence in blood flow or the vibration of heart tissues, which can occur in a systolic or a diastolic period. The presence of murmurs increases the heart sound complexity. Several recent studies use methods for nonlinear and chaotic signals to estimate the signal complexity and detect murmurs [AHL 08, AHL 06, GOM 12]. These methods are generally based on the reconstructed state space that explores the nonlinear behavior and the non-Gaussian components of the signal. However, even though it seems reasonable to expect the nonlinear and chaotic characteristics of turbulence in blood flow [RUE 71] through a vessel to be reflected in the murmurs, it is well accepted that recorded signals do not necessarily reflect the nonlinear and chaotic behavior of the underlying system

[SCH 00, SCH 11]. Moreover, the application of such methods suited for nonlinear or chaotic signals might be an unnecessary increase in algorithm complexity compared to linear methods based on autocorrelation and power spectrum [SCH 11]. Therefore, we apply the complexity measure on the TFR plane (ST-spectrogram) instead of the reconstructed state space, to detect murmurs in heart sounds.

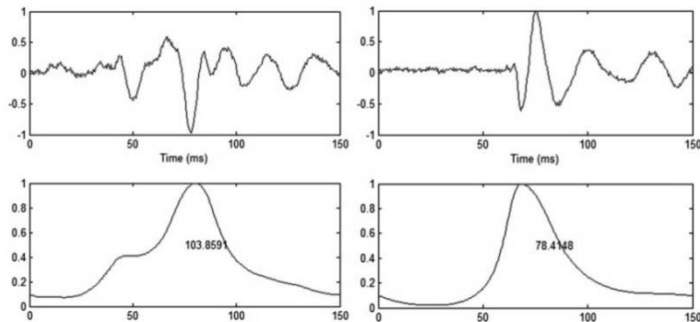


Figure 3.7. S1 (left) and S2 signals (right) and their normalized SSE envelopes with the values of β (bottom)

It has been shown in Chapter 2 how to calculate mathematically the normalized Shannon entropy (NSE) calculated from the ST-spectrogram coefficients (equations [2.47] and [2.48]).

The peaky TFRs of signals comprising small numbers of elementary components would yield small entropy values, while the diffuse TFRs of more complicated signals would yield large entropy values [BAR 01]. Figure 3.9 shows an example of normal and pathologic systolic sounds and their NSEs based on ST-spectrogram. The number of components in pathologic sound with the presence of a murmur is higher than the normal systole, which explains the higher NSE (0.88).

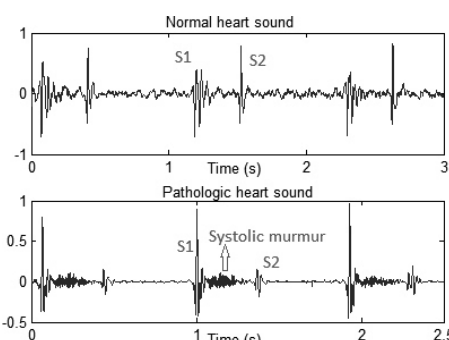


Figure 3.8. Example of a normal heart sound a) and a pathologic heart sound b) with systolic murmur

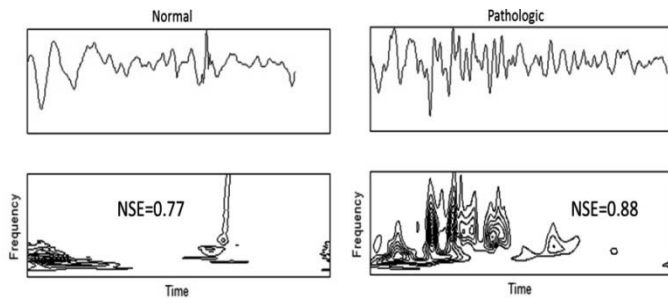


Figure 3.9. NSEs applied on the ST-spectrogram plane for normal and pathologic segmented systolic sounds

3.3. Results and discussion

3.3.1. Localization and segmentation results

The performance of the SSE methods was measured as the methods capacity to locate S1 and S2 correctly. It was measured by sensitivity:

$$\text{Sensitivity} = \frac{TP}{TP + FN} \quad [3.5]$$

and positive predictive value (PPV):

$$PPV = \frac{TP}{TP + FP} \quad [3.6]$$

A sound is true positive (TP) if it is correctly located, all other detected sounds are considered as false positive (FP) and all missed sounds are considered as false negative (FN).

Method	Sensitivity	PPV	Sensitivity (noise)	PPV (noise)
SSE	96%	95%	93%	94%

Table 3.1. Sensitivity and positive predictive values for SSE method applied on the clinical sounds set without and with additive Gaussian noise

The SSE method reaches 96% sensitivity and 95% PPV. In the presence of an additive white Gaussian noise, the performance of the SSE method is 93% for the sensitivity and 94% for the PPV (see Table 3.1). The robustness of the method against noise is very significant. This is due to the advantage of performing a TF analysis that makes the method more robust against noise. Figure 3.10 shows the

envelopes extracted by the SSE method that correspond to a pathologic sound with a systolic murmur. Figure 3.11 shows the robustness of the method against white additive noise.

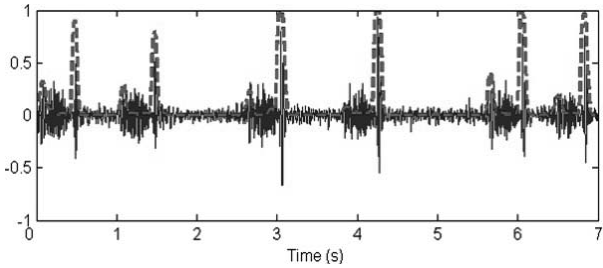


Figure 3.10. The SSE envelope (dashed lines) for a signal with systolic murmur

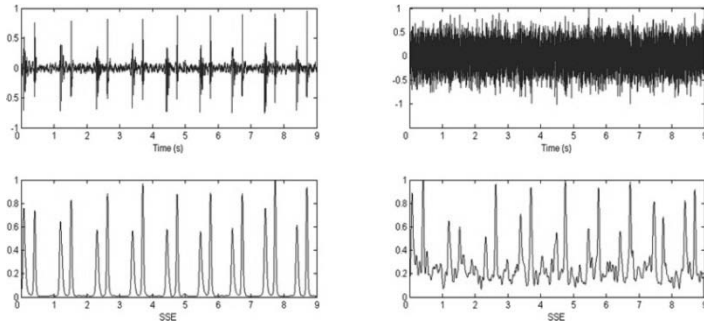


Figure 3.11. (Top) Envelope extraction for two normal PCG signals without and with additive Gaussian noise, and (bottom) their SSE envelopes

3.3.1.1. Boundary detection

The performance measure against parameter α is shown in Table 3.2. The values of α are chosen from a set, $0 < \alpha < 2$ with a step of 0.1, so 20 values in total. The optimal α is reached when $CM(\alpha)$ is maximized. Results from Table 3.2 show an important difference between optimized concentration measure and standard concentration that corresponds to the standard S-transform with $\alpha = 1$. The maximum values of concentration measures $CM(\alpha)$, which correspond to the optimum α , are obtained with $\alpha < 1$. This can be explained by the fact that when $\alpha < 1$, the Gaussian window of the S-transform is narrower, which improves the detection of the sudden changes in the signal, like the onset and the ending of the first and second heart sounds. However, when a window is narrower in the time domain, we lose in terms of frequency resolution. The compromise is performed by the optimization process that operates on the variable that controls the variance of

the Gaussian window, α for example. The criterion of the performance is the concentration energy measure. The enhancement of energy concentration in the TF domain clearly has an influence on the boundary estimation results (Table 3.3).

Heart sounds	Optimal α	$CM(\alpha)$	$CM(\alpha = 1)$
S1	0.82 ± 0.45	0.0185 ± 0.0017	0.0177 ± 0.0015
S2	0.55 ± 0.3	0.0186 ± 0.0015	0.0175 ± 0.0014
Total	0.68 ± 0.37	0.0185 ± 0.0016	0.0176 ± 0.0015

Table 3.2. Performance measure given by the maximum values of $CM(\alpha)$ and $CM(p)$ for a given parameters set of α and p , respectively

Method	S1 (ms)	S1(noise)	S2 (ms)	S2 (noise)
SSE	122.4 ± 7.2	127.8 ± 9.6	95.2 ± 8.3	101.2 ± 7.4
OSSE	110.7 ± 4.32	113.6 ± 6.5	69.1 ± 5.4	77.9 ± 8.2
Reference	105.8 ± 6		74.8 ± 5.65	

Table 3.3. S1 and S2 durations (ms) estimated by the SSE and OSSE methods with and without additive noise

The “Reference” row in Table 3.3 represents the manual measures made by the cardiologists using the “Stetho” software developed under the license of Alcatel-Lucent. Limits of heart sounds were defined with classical phonocardiographic references; mitral closure initiates S1 with high-frequency vibration, the aortic closure generates the high frequencies thus beginning S2 and the end of S1 and S2 is annotated by the end of the high-amplitude vibrations.

Results show the efficiency of optimizing the energy concentration of the S-transform in order to estimate more realistic boundaries for S1 and S2. Measures obtained by the SSE algorithm (without optimizing the S-transform) are always higher than the results given by the OSSE algorithm where an optimization process is performed. This is not surprising since the OSSE algorithm has a better energy concentration in the TF domain, which minimizes the spread of the energy beyond the S1 and the S2. Figure 3.12 shows the boundary detection results, with and without optimization of the S-transform, applied on an S2 example and Figure 3.13 shows the OSSE results applied on the entire heart sound (normal and pathologic).

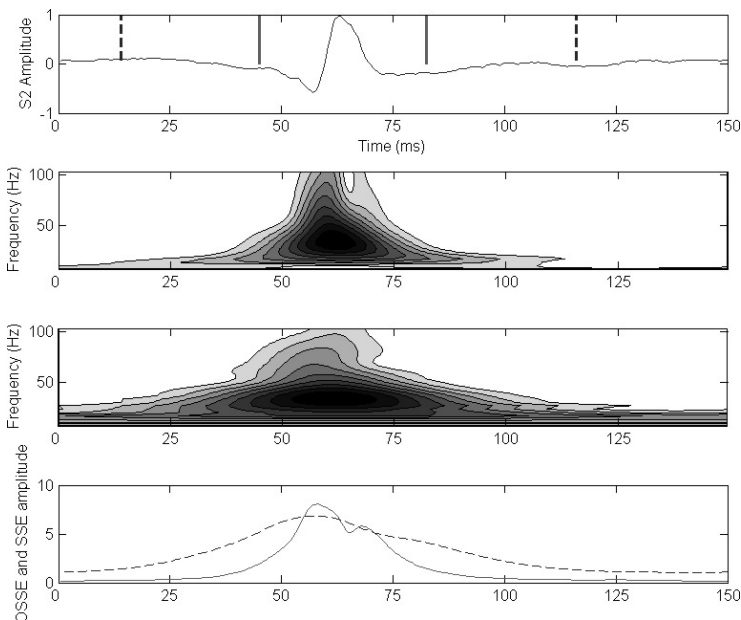


Figure 3.12. (Top) S2 signal with two detected boundaries calculated by the optimized S-transform and the standard S-transform (dashed line), S-transform with the optimum value $\alpha = 0.5$, standard S-transform with $\alpha = 1$; (bottom) SSE envelope for the optimized S-transform and standard S-transform (dashed line)

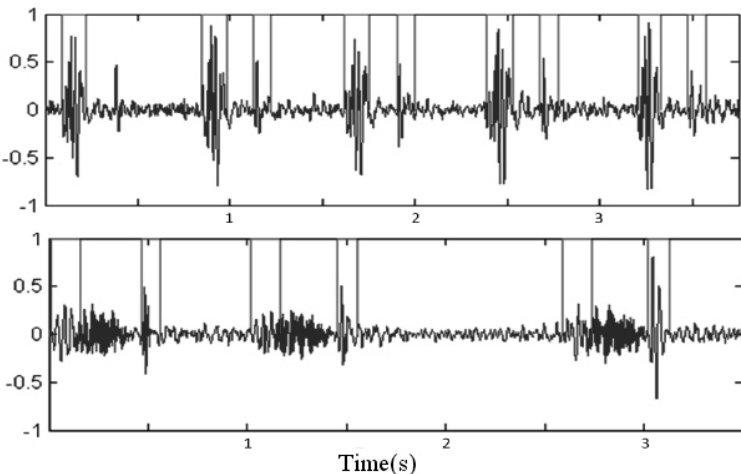


Figure 3.13. OSSE method applied on a normal heart sound a) and a pathological heart sound b)

3.3.2. S1 and S2 classification results

The localization of heart sounds is established by using the modified SSE method proposed in this study. The proposed features α and β are calculated for each segmented sound and the results are summarized in Table 3.4. The total number of S1 and S2 in the database (data set 2) is 2,636 (1,318 S1 and 1,318 S2) sounds that correspond to 62 heart signals and 8 subjects.

3.3.2.1. Results for the feature α_{opt}

Results show that the mean value of α_{opt} is greater for S1 than S2 (0.83 ± 0.13 and 0.59 ± 0.04 , respectively). This means that the width of the Gaussian window obtained with the optimization of the energy concentration is wider for S1 than S2. In other words, the algorithm needs a higher frequency resolution for S1 than S2. The first heart sound has a booming quality and is lower pitched, duller and longer than the second heart sound [FEL 90], the S1 can be considered more complicated than S2 from a physiological point of view and in terms of frequency components, which explains the need for a higher frequency resolution or larger analysis window for S1 than S2.

Subject	1	2	3	4	5	6	7	8	Total
AUC(α)	0.91	0.84	0.82	0.7	0.86	0.88	0.91	0.88	0.85
AUC(β)	0.9	0.84	0.94	0.77	0.89	0.88	0.96	0.8	0.87
S1(α)	0.79 ± 0.05	1.02 ± 0.76	1.03 ± 0.35	0.71 ± 0.07	0.7 ± 0.03	0.8 ± 0.06	0.88 ± 0.37	0.74 ± 0.18	0.83 ± 0.13
S2(α)	0.61 ± 0.01	0.6 ± 0.03	0.66 ± 0.03	0.61 ± 0.01	0.5 ± 0.02	0.6 ± 0.04	0.61 ± 0.03	0.6 ± 0.03	0.59 ± 0.04
S1(β)	0.57 ± 0.15	0.63 ± 0.1	0.6 ± 0.1	0.65 ± 0.21	0.65 ± 0.08	0.63 ± 0.11	0.67 ± 0.11	0.56 ± 0.17	0.62 ± 0.03
S2(β)	0.29 ± 0.07	0.39 ± 0.12	0.26 ± 0.06	0.39 ± 0.14	0.4 ± 0.06	0.32 ± 0.13	0.32 ± 0.05	0.37 ± 0.11	0.34 ± 0.05
HR (bpm)	162	180	170	186	186	192	198	180	

Table 3.4. The area under curve (AUC), mean values and standard deviations of each feature (S1(α), S2(α), S1(β), S2(β)) and the maximum heart rate (HR_{max}) reached for each subject

Figure 3.14 shows the area under curve (AUC) for the α_{opt} feature and for each subject. The lowest AUC corresponds to subject 4 (0.7). The highest AUC is 0.91 and the overall AUC is 0.85.

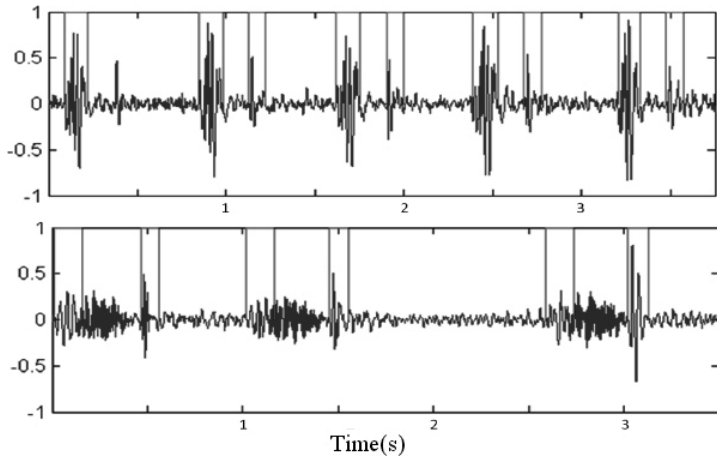


Figure 3.14. Receiver operation characteristic curves for the feature α and for all subjects

The probability that the two groups ($S1(\alpha)$ and $S2(\alpha)$) come from distributions with different medians is calculated by the Mann–Whitney U -test ($p < 0.0001$) (Table 3.5). Significant differences between the two groups, with 95% confidence, are found. The classification results are promising. This is very interesting since this parameter α was also used to refine the boundary detection of $S1$ and $S2$ in the segmentation process.

Feature	<i>p</i> -value	Range (S1)	Range (S2)
α	<0.0001	0.5–2	0.5–0.92
β	<0.0001	0.3–1	0.13–0.88

Table 3.5. Significance values (Mann–Whitney U -test), range and the area under curve (AUC) results obtained for all subjects and for each proposed feature

Figure 3.15 shows an example of a segmented heart sound under stress (level 5) with the different α_{opt} values calculated at each segmented sound ($S1$ and $S2$).

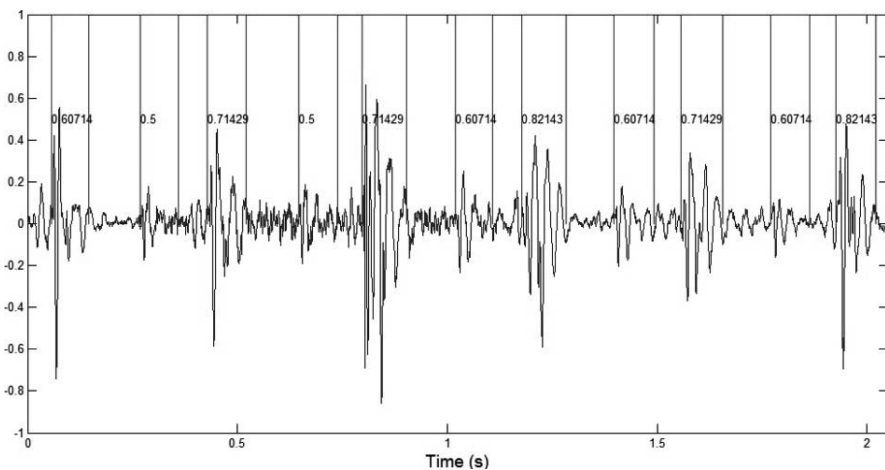


Figure 3.15. Example of a segmented stress test heart sound with the optimal α value calculated for each located sound

Figure 3.16 shows the results of another segmented sound with the different normalized β values.

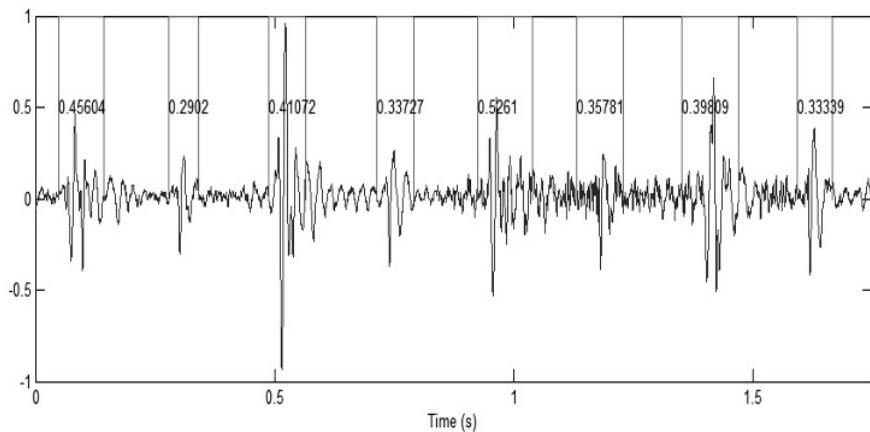


Figure 3.16. Example of a segmented stress test heart sound with the values of the feature β calculated for each located sound (S1 and S2)

Figure 3.17 shows the AUC for the β feature and for each subject. The lowest AUC corresponds to subject 4 (0.77). The highest AUC is 0.96 and the global AUC is 0.87, which is higher than the α_{opt} feature. The low AUC results for subject 4 obtained with α_{opt} and β can be explained by the high noise level in the acquired signal due to the acquisition process.

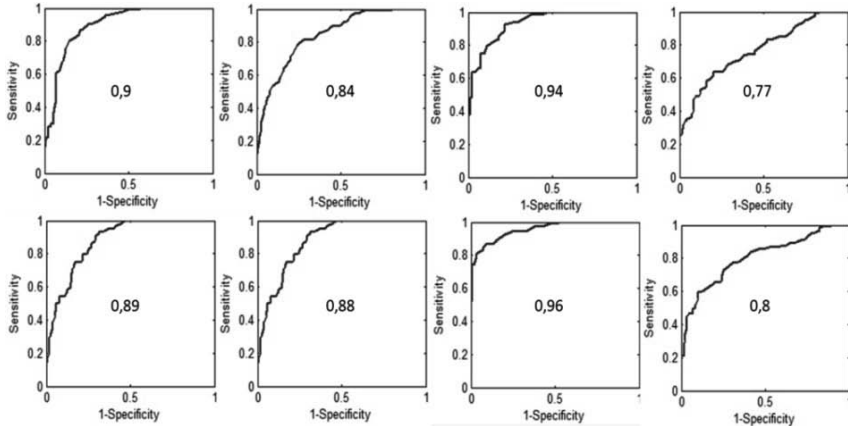


Figure 3.17. Receiver operation characteristic curves for the feature β and for all subjects

3.3.3. Murmur detection results

The NSE feature has been applied on 30 heart sounds from data set 1 separated into two groups: 15 normal sounds and 15 pathologic sounds with systolic murmurs. The sounds are automatically segmented in order to extract systolic periods from heart sounds. Accurate segmentation of heart sounds is essential for the extraction of meaningful features, well oriented, from each part of heart cycles. The segmentation algorithm used is the OSSE algorithm presented above. The feature extraction process extracts an NSE feature value per extracted systolic signal and each of these features is averaged across available systolic signals from each subject. So, from each subject in the database, we obtain one feature that quantifies the complexity of systolic periods in the heart sound. The NSE feature is evaluated by calculating the AUC for ST and STFT (for comparison) for three levels of noise: the first level corresponds to the experimental sounds acquired in clinical conditions (the patient's position during auscultation, the surrounding noise, etc.) and two levels (noise 1 and noise 2) correspond to the two increasing levels of additive white Gaussian noise.

Figure 3.18 shows a comparison between the extracted NSEs based on the ST and the STFT spectrograms. The ST-spectrogram showed the highest AUC (0.98).

The robustness of the ST-spectrogram-based features against additive noise is shown in Figure 3.19. The AUC is 0.88 for the highest level of noise (noise 3), which can be considered as a good classification rate.

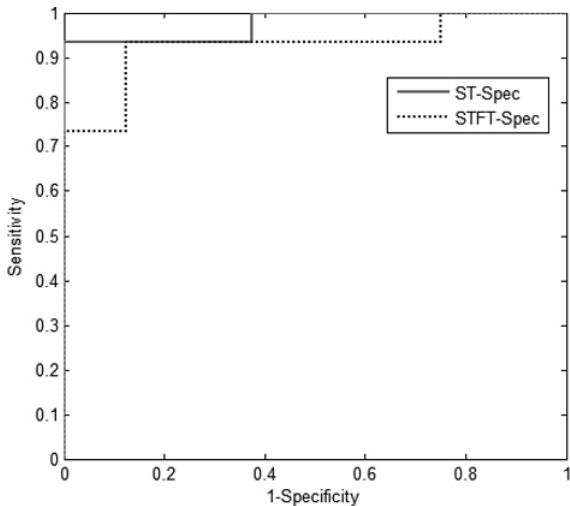


Figure 3.18. ROCs for the NSE applied on the ST-spectrogram (solid line, AUC = 0.98) and the STFT-spectrogram (dashed line, AUC = 0.93)

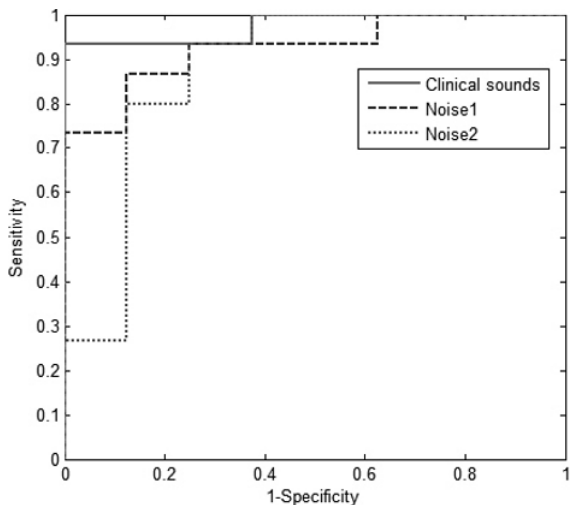


Figure 3.19. Variation of the ROC against white additive Gaussian noise for the ST-spectrogram; clinical sounds without additive noise (AUC = 0.98), noise 1 (medium-level noise, AUC = 0.93) and noise 2 (high-level noise, AUC = 0.88)

Figure 3.20 shows the robustness of the NSE measures based on the STFT-spectrogram against additive noise. For the clinical sounds, the extracted features give a good performance ($AUC = 0.93$) but this is not the case in the presence of additive noise (0.83 and 0.7), where the performance decreases significantly. The NSE based on the ST-spectrogram shows a high performance in the classification of normal and pathologic heart sounds. The results are summarized in Table 3.6.

Spectrogram	AUC 1	AUC 2	AUC 3
ST	0.98	0.93	0.88
STFT	0.93	0.84	0.7

Table 3.6. The variation of AUC against white additive noise for the ST and the STFT spectrograms

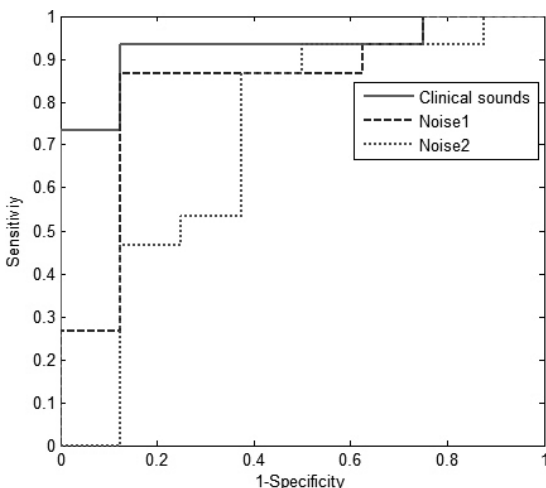


Figure 3.20. Variation of the ROC against white additive Gaussian noise for the STFT-spectrogram; clinical sounds without additive noise ($AUC = 0.93$), noise 1 (medium-level noise, $AUC = 0.84$) and noise 2 (high-level noise, $AUC = 0.7$)

3.4. Conclusion

This chapter presented several algorithms and methods to segment and classify the heart sounds (PCG signal). Heart sounds are accurate for diagnosing some heart diseases. They are non-stationary signals by nature (as most biosignals), which makes the application of TF-based methods intuitive.

This chapter focused on the application of the S-transform on heart sounds. Several theoretical methods proposed in Chapter 2 have been applied on real signals in this chapter. Localization, segmentation, feature extraction and classification schemes of heart sounds have been explored and discussed. The methods have been assessed on databases containing real data.

3.5. Bibliography

- [AHL 06] AHLSTROM C., HULT P., RASK P., *et al.*, “Feature extraction for systolic heart murmur classification”, *Annals of Biomedical Engineering*, vol. 34, no.11, pp. 1666–1677, 2006.
- [AHL 08] AHLSTROM C., Nonlinear phonocardiographic signal processing, Thesis, Linkoping University, Sweden, April 2008.
- [BOU 11] BOUTANA D., BENIDIR M., BARAKAT B., “Segmentation and identification of some pathological phonocardiogram signals using time-frequency analysis”, *IET Signal Process*, vol. 5, no. 6, pp. 527–537, 2011. Doi: 10.1049/iet-spr.2010.0013.
- [BEY 09] BEYA O., BUSHRA J., FAUVET E., *et al.*, Application de l’EMD sur des signaux cardiaques, CNRIUT- Lille, 2009.
- [CHA 97] CHARLESTON S., AZIMI-SADJADI M.R., “Reduced order Kalman filtering for the enhancement of respiratory sounds”, *IEEE Transactions on Biomedical Engineering*, vol. 44, pp. 1006–1019, 1997.
- [CHA 06] CHARLESTON S., ALJAMA A.T., GONZÁLEZ R., “Analysis of simulated heart sounds by intrinsic mode functions”, *Proceedings of the 28th IEEE EMBS Annual International Conference*, New York, 30 August–3 September 2006.
- [CHO 06] CHOI S., JIANG Z., Comparison of envelope extraction algorithms for cardiac sound signal segmentation, Micro-Mechatronics Laboratory, Yamaguchi University, Japan, 2006.
- [DEB 08] DEBBAL S.M., BEREKSI-REGUIG F., “Computerized heart sounds analysis”, *Computers in Biology and Medicine*, vol. 38, pp. 263–280, 2008.
- [DJE 00] DJEBBARI A., BEREKSI R.F., “Short-time Fourier transform analysis of the phonocardiogram signal”, *7th IEEE International Conference on Electronics, Circuits and Systems 2000 (ICECS 2000)*, pp. 844–847, December 2000.
- [DJE 13] DJEBBARI A., BEREKSI-REGUIG F., “Detection of the valvular split within the second heart sound using the reassigned smoothed pseudo Wigner–Ville distribution”, *BioMedical Engineering OnLine*, vol. 12, 2013.
- [DOK 07] DOKUR Z., ÖLMEZ T., “Feature determination for heart sounds based on divergence analysis”, *Digital Signal Process*, vol. 19, pp. 521–531, 2007. Doi:10.1016/j.dsp.2007.11.003.

- [FEL 90] FELNER J.M., “The first heart sound”, in WALKER H.K., HALL W.D., HURST J.W. (eds), *Clinical Methods: The History, Physical, and Laboratory Examinations*, 3rd ed., Chapter 22, Butterworths, Boston, MA, 1990.
- [GRO 01] GROCHENIG K., *Foundations of Time-Frequency Analysis*, Birkhäuser, Boston, MA, 2001.
- [GOM 11] GOMEZ-GARCIA J.A., MARTINEZ-VARGAS J.D., CASTELLANOS-DOMINGUEZ G., “Complexity-based analysis for the detection of heart murmurs.” *Annual International Conference of the IEEE Engineering in Medicine and Biology Society (Embc)*. pp. 2728–31, 2011.
- [GUP 07] GUPTA C.N., PALANIAPPAN R., SWAMINATHAN S., *et al.*, “Neural network classification of homomorphic segmented heart sounds”, *Applied Soft Computing*, vol. 7, pp. 286–297, 2007.
- [HAN 11] HANSEN J., ZIMMERMANN N.H., SCHMIDT S., *et al.*, “System for acquisition of weak murmurs related to coronary artery diseases”, *Computing in Cardiology*, vol. 38, pp. 213–216, 2011.
- [HAS 04] HASSANPOUR H., MESBAH M., BOASHASH B., “Time-frequency feature extraction of newborn EEG seizure using SVD-based techniques”, *EURASIP Journal on Applied Signal Processing*, vol. 16, pp. 2544–2554, 2004.
- [HE 11] HE L., LECH M., MADDAGE C.N., *et al.*, “Study of empirical mode decomposition and spectral analysis for stress and emotion classification in natural speech”, *Biomedical Signal Processing and Control*, vol. 6, pp. 139–146, 2011.
- [KUM 11] KUMAR D., CARVALHO P., ANTUNES M., *et al.*, “An Adaptive Approach to Abnormal Heart Sound Segmentation”, *Proceedings of the IEEE International Conference on Acoustics, Speech, and Signal Processing (ICASSP)*, 2011.
- [LIA 97] LIANG H., LUKKARINEN S., HARTIMO I., “Heart sound segmentation algorithm based on heart sound envelopogram”, *Proceedings of Computers in Cardiology*, Helsinki University of Technology, Espoo, Finland, pp. 105–108, 7–10 September 1997.
- [LIA 98] LIANG H., LUKKARINEN S., HARTIMO I., “A boundary modification method for heart sound segmentation algorithm”, *Proceedings of Computers in Cardiology*, Helsinki University of Technology, Espoo, Finland, pp. 593–595, 13–16 September 1998.
- [LIA 05] LIANG H., LIN Z., MCCALLUM R., “Application of the empirical mode decomposition to the analysis of esophageal manometric data in gastroesophageal reflux disease”, *IEEE Transactions on Biomedical Engineering*, vol. 52, no. 10, pp. 1692–1701, 2005.
- [LIJ 12] LIJUAN J., DANDAN S., LINMI T., YAO L., “Heart sounds classification with a fuzzy neural network method with structure learning”, *Advances in Neural Networks*, Lecture Notes in Computer Science, vol. 7368, pp. 130–140, 2012.
- [LIU 10] LIU L., WANG H., WANG Y., *et al.*, “Feature analysis of heart sound based on the improved Hilbert-Huang transform”, *3rd IEEE International Conference on Computer Science and Information Technology (ICCSIT)*, 2010.

- [MAG 09] MAGLOGIANNIS I., LOUKIS E., ZAFIROPOULOS E., *et al.*, “Support vectors machine-based identification of heart valve diseases using heart sounds”, *Computer Methods and Programs in Biomedicine*, vol. 95, no. 1, pp. 47–61, 2009. Doi: 10.1016/j.cmpb.2009.01.003.
- [MAR 85] MARINOVIC M., EICHMANN G., “Feature extraction and pattern classification in space-spatial frequency domain”, *SPIE Intelligent Robots and Computer Vision*, vol. 0579, pp. 19–25, 1985.
- [MCF 99] MCFADDEN P.D., COOK J.G., FORSTER L.M., “Decomposition of gear vibration signals by the generalized S-transform”, *Mechanical Systems and Signal Processing*, vol. 13, no. 5, pp.691–707, 1999.
- [MES 01] MESSER S.R., AGZARIAN J., ABBOTT D., “Optimal wavelet denoising for phonocardiograms”, *Microelectronics Journal*, vol. 32, no. 12, pp. 931–41, 2001.
- [MOU 04] MOUSSAVI Z., FLORES D., THOMAS G., “Heart sound cancellation based on multiscale products and linear prediction”, *Proceedings of the 26th Annual International Conference of the IEEE EMBS*, San Francisco, CA, 1–5 September 2004.
- [MOU 11a] MOUKADEM A., DIETERLEN A., HUEBER N., BRANDT C., “Localization of heart sounds based on S-transform and radial basis functions”, *15th Nordic-Baltic Conference on Biomedical Engineering and Medical Physics (NBC 2011)*, IFMBE Proceedings, vol. 34, pp. 168–171, 2011. Doi: 10.1007/978-3-642-21683-1_42.
- [MOU 11b] MOUKADEM A., DIETERLEN A., HUEBER N., *et al.*, “Comparative study of heart sounds localization”, *Bioelectronics, Biomedical and Bio-inspired Systems*, SPIE No. 8068A-27, Prague, 2011.
- [MOU 12] MOUKADEM A., DIETERLEN A., BRANDT C., “Study of two feature extraction methods to distinguish between the first and the second heart sounds”, *International Conference on Bio-inspired Systems and Signal Processing*, BIOSIGNALS, Portugal, 2012.
- [MOU 13] MOUKADEM A., DIETERLEN A., BRANDT C., “A robust heart sound segmentation module based on S-transform”, *Biomedical Signal Processing and Control*, vol. 8, pp. 273–281, 2013.
- [PIN 03] PINNEGAR C.R., MANSINHA L., “The S-transform with windows of arbitrary and varying shape”, *Geophysics*, vol. 68, no. 1, pp. 381–385, 2003.
- [RIL 03] RILLING G., FLANDRIN P., GONCALVÈS P., “On empirical mode decomposition and its algorithms”, *Proceedings of the IEEE/EURASIP Workshop on Nonlinear Signal and Image Processing (NSIP)*, Grado, Italy, 2003.
- [ROB 11] ROBERT C., SCHLANT R., WAYNE A., *The Heart Arteries and Veins*, 8th ed., vol. 1, Chapter 11, McGraw Hill Inc., 1994.
- [RØN 11] RØNVED S.M.M., GJERLØV I., BROKJÆR A., *et al.*, “Phonocardiographic recordings of first and second heart sound in determining the systole/diastole-ratio during exercise test”, *Proceedings of the International Federation for Medical and Biological Engineering*, vol. 34, pp. 85–88, 2011.

- [RUE 71] RUELLE D., TAKENS F., “On the nature of turbulence”, *Communications in Mathematical Physics*, vol. 23, no. 4, pp. 343–344, 1971.
- [SAM 06] SAMIT A., KUMAR P., GOUTAM S., “On an algorithm for boundary estimation of commonly occurring heart valve diseases in time domain”, *Annual IEEE India Conference*, 2006.
- [SCH 00] SCHREIBER T., SCHMITZ A., “Surrogate time series”, *Physica D: Nonlinear Phenomena*, vol. 142, no. 3–4, pp. 346–382, 2000.
- [SCH 94] SCHLANT R.C., WAYNE ALEXANDER R. (eds), *The Heart Arteries and Veins*, 8th ed., vol. 1, Chapter 11, McGraw Hill Inc., 1994.
- [SCH 10] SCHMIDT S.E., HOLST-HANSEN C., GRAFF C., et al., “Segmentation of heart sound recordings by a duration-dependent hidden Markov mode”, *Physiological Measurement*, vol. 31, no. 4, pp. 513–529, 2010.
- [SCH 11] SCHMIDT SE, GRAEBE M, TOFT E, et al., “No evidence of nonlinear or chaotic behavior of cardiovascular murmurs”, *Biomedical Signal Processing*, vol. 6, no. 2, pp. 157–63, 2011.
- [SEJ 04] SEJDIC E., JIANG J., “Comparative study of three time-frequency representations with applications to a novel correlation method”, *Proceedings of the IEEE International Conference on Acoustics, Speech and Signal Processing (ICASSP '04)*, vol. 2, Montreal, Quebec, Canada, pp. 633–636, May 2004.
- [SEJ 08] SEJDIC E., DJUROVIC I., JIANG J., “A window width optimized S-transform”, *EURASIP Journal on Advances in Signal Processing*, 2008. Doi:10.1155/672941.
- [SEP 09] SEPEHRI A.A., et al., “A nouvel method for pediatric heart sound segmentation without using the ECG”, *Computer Methods and Programs in Biomedicine*, vol. 99, pp. 43–48, 2009. Doi:10.1016/j.cmpb.2009.10.006.
- [SIN 07] SINHA R.K., AGGARWAL Y., DAS B.N., “Back propagation artificial neural network classifier to detect changes in heart sound due to mitral valve regurgitation”, *Journal of Medical Systems*, vol. 31, no. 3, pp. 205–209, 2007.
- [STA 01] STANKOVIC L.J., “Measure of some time-frequency distributions concentration”, *Signal Processing*, vol. 81, no. 3, pp. 621–631, 2001.
- [STO 96] STOCKWELL R.G., MANSINHA L., LOWE R.P., “Localization of the complex spectrum: the S-transform”, *IEEE Transactions on Signal Processing*, vol. 44, no. 4, pp. 998–1001, 1996.
- [VEP 09] VEPA J., “Classification of heart murmurs using cepstral features and support vector machine”, *Annual International Conference of the IEEE Engineering in Medicine and Biology Society (EMBC)*, 2009.
- [YAN 09] YAN Z., et al., “The moment segmentation analysis of heart sound pattern”, *Computer Methods and Programs in Biomedicine*, vol. 98, pp. 140–150, 2009. Doi:10.1016/j.cmpb.2009.09.008.

Adaline for the Detection of Electrical Events in Electrical Signals

In previous chapters, the S transform was presented and applied to biological signals. In this chapter, we will discuss another method of signal processing called adaptive linear neuron (Adaline), which is the outcome of artificial neural network (ANN) techniques. The field of electrical supply networks will be applied to identify the events of electrical signals, such as current harmonics and voltage unbalance. There are similarities between the electrocardiogram (ECG) signals and the electrical signals for the extraction of events. The increasingly non-stationary character of electric signals requires the use of more sophisticated methods. This chapter will show that the use of decompositions based on the Fourier series enables Adaline to provide a better estimation of the electrical signal parameters.

4.1. Introduction

World energy demand has increased in recent years. For example, European consumption increased by 10.8% between 1999 and 2004 [BER 06]. In contrast to this increase, energy resources are diminishing. Furthermore, the power quality is deteriorating, which causes additional costs for additional consumption.

The most common problems are on the consumer side. Indeed, the widespread use of power electronic components in almost all electrical equipment distorts the voltage and current including the presence of excessive harmonics. The origin of these harmonics includes rectifiers, computer equipment, air conditioning units or lighting-based fluorescent tubes, etc. The resulting disturbances increase costs of consumption resulting in penalties to be applied by the energy supplier.

The various measures that can be done in real time open up a major field to better management of the available energy.

In this chapter, we discuss three major electrical events: frequency variation, voltage unbalance and current harmonics. We develop several methods based on Adaline in order to identify the events in the signal in the case of several conditions. The approach consists of finding new decompositions of electrical signals to make the parameters linearly separable.

4.2. Electric events

4.2.1. Power quality

Since the beginning of the commercialization and use of electricity, the power quality has been related to the availability and continuity of service to continuously provide consumers. Today, the notion of the power quality has evolved with the decentralization of the electricity market and the massive use of equipment based on power electronics. The form and content of the electrical signal is thus affected and requires new solutions to correct the faults.

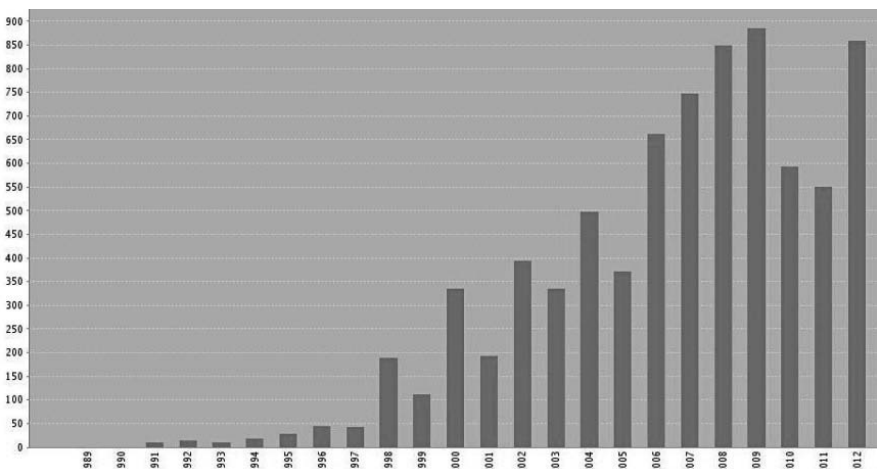


Figure 4.1. Published items in each year containing the term “power quality”

To illustrate the interest of the scientific community in the quality of energy, it is sufficient to note the increasing number of articles containing the word “power quality”. Figure 4.1 shows the number of articles per year, according to the database

“Web of Knowledge”, where the term “power quality” appears in the title, abstract or list of keywords.

It clearly appears that interest in the quality of energy began to develop in the mid-1990s. We note, for example, that the number of articles published in 2012 is 43 times larger than the number of articles published in 1994. This indicates a recent interest in the quality of energy.

4.2.2. Electric events

The power quality is judged by the quality of the voltage and current. The characteristic parameters of these electrical signals are:

- frequency;
- waveform;
- unbalance.

The deterioration of these parameters involves the presence of disturbance in the power grid.

This section focuses on the most common and most harmful phenomena: frequency variation, unbalance, power factor and harmonic current. The knowledge of these events helps us to mitigate them. However, these events are of interest because they are unique to each device and provide their signatures.

1) Frequency variation

Under normal operating conditions, the average value of the fundamental frequency must be in the range 50 ± 1 Hz (in the case of France).

The frequency variations may occur in users connected to non-interconnected grid systems. They are rarely found on the transmission grids but since the decentralization of electricity generation and multiplication of renewable energy sources, the case of variations in the frequency increases. This new situation requires more rigorous monitoring of the frequency.

2) Unbalance

A slow variation in the load may cause a voltage drop for a long period. The faults in the distribution networks and the operation of certain appliances, such as booting machines, can cause voltage dips. The inequality of power demand on each phase is reflected in the inequality of voltage amplitudes and phase shifts, which is called unbalance.

3) Harmonics

Harmonics, often generated by nonlinear loads, circulate in the electric supply network and affect the form of the sine wave current. They are sinusoidal currents having a frequency multiple of the fundamental frequency.

Harmonics are characterized by their amplitudes and frequencies. The current signal is thus the sum of the fundamental frequency and all harmonics. It is possible to characterize the presence of the harmonics in the signal by its spectrum analysis.

4.3. Adaline

In 1960, Widrow and his graduate student, Marcian Hoff, introduced the Adaline network and the Widrow–Hoff learning rule, which they also called the least mean square (LMS) algorithm [WID 96, HAG 96]. Their Adaline network is very similar to the perceptron, except that its transfer function is linear, instead of hard limiting. Both the Adaline and the perceptron suffer from the same inherent limitation because they can only solve linearly separable problems. Adaline has been applied successfully in many power applications, including feature extraction [DAS 00], harmonic estimation [OUL 07a, WIR 07, NGU 09a, NGU 08, NGU 11], frequency deviation estimation [DAS 97] and symmetrical components extraction [OUL 07b, NGU 09b]. In this chapter, Adaline is introduced as an efficient tool for fault identification. The Adaline structure is shown in Figure 4.2; it is a p input, single output, signal processing element. In signal processing applications, the most popular method for adapting the weights is the simple LMS algorithm [WID 60].

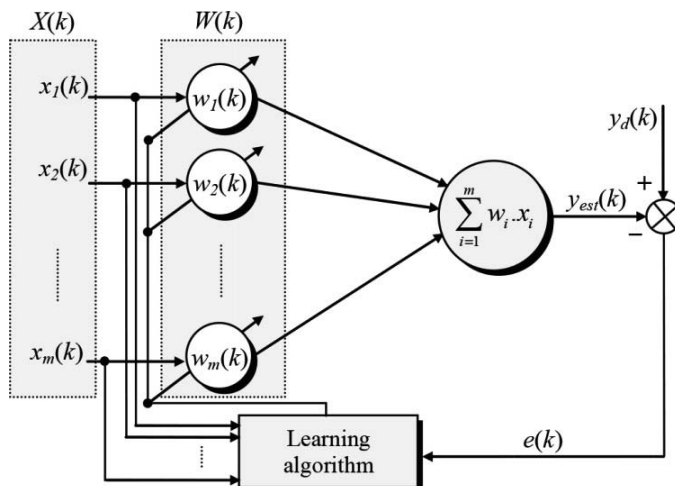


Figure 4.2. Adaline architecture

The weights are updated by the form:

$$W(k+1) = W(k) + \alpha \frac{e(k)X(k)}{|X(k)|^2} \quad [4.1]$$

The time index or adaptation cycle number is k . $W(k+1)$ is the next value of the weight vector, $W(k)$ is the present value of the weight vector and $X(k)$ is the present pattern input vector. The present linear error $e(k)$ is the difference between the desired response $y_d(k)$ and the linear output $y_{es}(k)$, during presentation k before adaptation. This error signal is necessary for adapting the weights: therefore, the error is reduced by a learning rate and the weights are changed while holding the input pattern fixed. Presenting a new input pattern starts the next adaptation cycle. The initial weight vector is usually chosen to be zero and is adapted until convergence. The choice of α controls stability and speed of convergence; its practical range is:

$$0 < \alpha < 1$$

The main advantage of the Adaline is the ability to be trained online, eliminating the need for repetitive offline training. Although most neural networks have the ability of online training, the Adaline is superior because of its simple structure and speed processing. The LMS algorithm is more powerful and has many more practical uses than the perceptron learning rule. For example, most long-distance phone lines use Adaline networks for echo cancellation.

4.4. Adaline for frequency estimation

The required objective is to estimate online the fundamental frequency of a sinusoidal voltage corrupted by noise and harmonic distortions. This estimation is based on the pseudo-square Adaline [HAL 09].

4.4.1. Adaline method

The Adaline has been introduced for frequency estimation. This approach has been used since to identify the parameters of the voltage signal of form:

$$v(k) = \sum_{n=1}^{\infty} A_n \sin(\omega_n k T_e + \varphi_n) \quad [4.2]$$

where A_n is the amplitude of the n th term, ω_n its pulsation and φ_n its phase. T_e is the sampling period. The recursive expression of $v(k)$ can be deduced as follows:

$$\begin{aligned} v(k+1) + v(k-1) &= \sum_{n=1}^{\infty} A_n \sin(\omega_n k T_e + \varphi_n) \cdot 2 \cos(\omega_n T_e) \\ &= 2 \cos(\omega_n T_e) \cdot v(k) \end{aligned} \quad [4.3]$$

If the harmonics are neglected, the voltage signal $v(k)$ can be rewritten as:

$$v(k) = 2 \cos(\omega_1 T_e) \cdot v(k-1) - v(k-2).$$

As shown in Figure 4.3, by taking $v(k-1)$ and $v(k-2)$ as inputs of the Adaline, its weights w_1 and w_2 will adapt and converge toward the values $2\cos(\omega_1 T_e)$ and -1 , respectively. The LMS algorithm with the learning rate η is generally applied for weight training [BEC 12]. Hence, at each iteration, the voltage signal frequency is reconstructed online as:

$$f_1 = \frac{1}{2\pi T_e} \cdot \arccos\left(\frac{w_1}{2}\right) \quad [4.4]$$

The main advantage of this method is its robustness to the voltage signal amplitude and phase. A proof of convergence of weights of an Adaline can be found in [DAS 97].

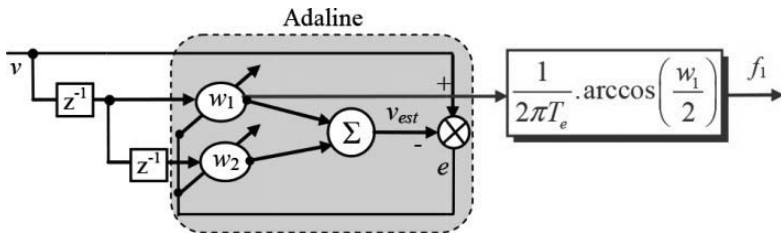


Figure 4.3. Adaline for frequency tracking

However, the sampling period T_e has a great influence on the performances of this approach. Then, it is important to show that the estimated frequency f_1 depends on the sampling period T_e . Indeed, in the presence of the harmonics, the function \arccos in [4.4] is sensitive to the variation of weights. Figure 4.4 shows the weight value w_1 according to T_e for 50 Hz grid frequency. From this figure, we can note that $T_e = 5$ ms represents a good choice in the sense that it corresponds to $w_1 = 0$, which is the center of the range $[+2, -2]$. The selected T_e value gives greater dynamics

compared to a fundamental frequency change. Figure 4.5 shows the relationship between the frequency and the weight w_1 for various T_e values. It can be deduced that the maximum variation of the weight is obtained with an adequate sampling period $T_e = 1/4f_1$ for $w_1 = 0$. In this figure, an example is shown for $f_1 = 50$ Hz. Consequently, the sampling period of $T_e = 1/4f_1$ is chosen in order to maximize the dynamics and to ensure the stability of the system. It should be noted that the choice of $T_e = 1/4f_1$ has as a consequence the part suppression of existing harmonics in the grid voltage. In our case, all the frequencies greater than 100 Hz will be eliminated for $T_e = 5$ ms.

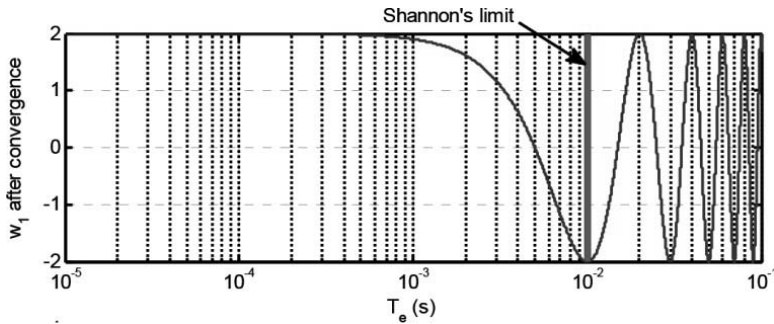


Figure 4.4. T_e influence on the weight w_1 convergence value

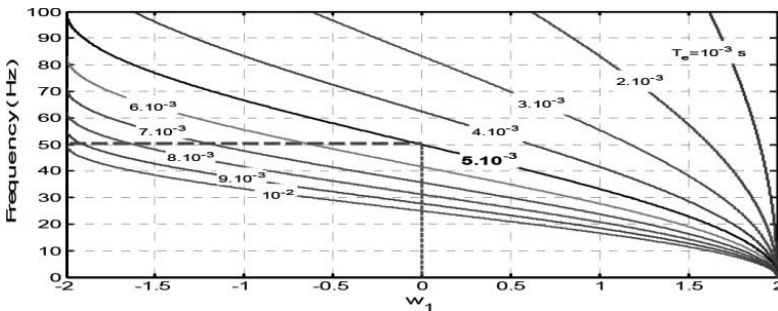


Figure 4.5. Observable frequency as a function of w_1 for different values of T_e

This method is not adequate with respect to the harmonics. To improve the frequency estimation performance in a polluted and distorted voltage signal, an alternative to this approach is proposed. To accentuate the difference between two signals in close frequencies over one period, it is possible to perform a premultiplication of $v(k)$ with $v(k - D)$, where D is the number of delayed sampling

periods, before performing the calculations. Thus, the new voltage signal $V(k)$ at the Adaline input is:

$$\begin{aligned} V(k) &= v(k).v(k-D) \\ &= \frac{A_1^2}{2} \alpha \{1 - \cos(2\omega_1 k T_e + 2\varphi_1)\} - \frac{A_1^2}{2} \beta \sin(2\omega_1 k T_e + 2\varphi_1) \end{aligned} \quad [4.5]$$

with $\alpha = \cos(\omega_1 k T_e)$ and $\beta = \sin(\omega_1 k T_e)$. By choosing $T_e = 1/(4f_1) = 2.5$ ms corresponding to $f_1 = 100$ Hz and by calculating D from $D = d/T_e$, with d selected equal to $T/4 = 5$ ms ($f = 50$ Hz), the α value is negligible compared to the β value for frequencies close to 50 Hz. Thus, the voltage signal $V(k)$ can be written in the form:

$$V(k) = -\frac{A_1^2}{2} \sin(2\omega_1 k T_e + 2\varphi_1) \quad [4.6]$$

By using an Adaline and following the same procedure as shown in Figure 4.3, the polluted and distorted voltage frequency can be estimated from the weight w_1 . The principle scheme is illustrated in Figure 4.6.

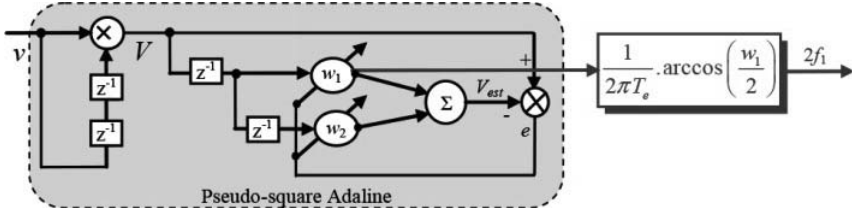


Figure 4.6. Frequency estimator based on the pseudo-square Adaline

4.4.2. Results

To validate and compare the suggested Adaline method performance with the conventional phase-locked loop (PLL), an experiment was set up. A DS1104 dSPACE board based on TMS320F240 floating point digital signal processor (DSP) is used. The proposed AN-PLL and conventional PLL algorithms are implemented under Matlab–Simulink with a sampling period of 0.1 ms. The grid voltages are measured using three Hall effect transducers of LEM Components Company (LV25–P type). The voltages are measured in real time and acquired by means of an analog–digital (A/D) converter in the dSPACE board. All the signals can be visualized and recorded on a PC via the visualization software ControlDesk. The experimental platform scheme is shown in Figure 4.7.

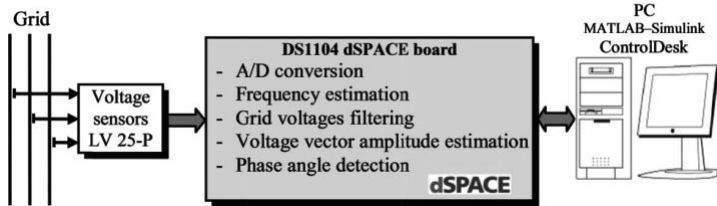


Figure 4.7. Experimental platform scheme

An experimental comparative study between the proposed Adaline method and the conventional PLL is presented. The estimated quantities such as voltage vector amplitude, frequency and phase angle have been taken as comparison quantities. Moreover, the measured grid voltages, filtered voltages and unitary three-phase system are shown in order to analyze better the Adaline method operation. The learning rates of the Adaline networks used, ensuring an optimal speed of convergence of weights, are experimentally adjusted. For the pseudo-square Adaline, the learning rate is set to 0.04, and for the adaptive filtering, the learning rate is set to 0.01. The Proportional Integral (PI) parameters in the PLL are calculated to obtain a response time $t_r = 10$ ms, a damping coefficient $z = 1$ and a natural pulsation $\omega_n = 4.5$ rad/s. Disturbances of two grid voltages, such as voltage sag and two-phase fault, have been considered. The experimental study starts with an analysis of performances of the proposed Adaline method in normal operating conditions (without faults), and ends with an experimental comparative study between the proposed Adaline method and the conventional PLL under severe conditions.

Figure 4.8 shows AN-PLL performances under normal operating conditions. The filtered grid voltages (Figure 4.8(b)) are in phase with the real measured grid voltages (Figure 4.8(a)). Indeed, each filtered voltage represents the positive-sequence of its measured voltage. Then, balanced three-phase voltages are obtained. By dividing each filtered voltage by its detected maximal amplitude, a sinusoidal and balanced three-phase system is obtained with unit amplitude and in phase with the grid voltages (Figure 4.8(c)). Thereafter, the detected maximal amplitudes are exploited to estimate the voltage vector amplitude U_{est} . As shown in Figure 4.8(d), the amplitude U_{est} is estimated with high precision and very low oscillations. The pseudo-square Adaline conceived to estimate the utility frequency in the presence of distortion harmonics shows a good performance (Figure 4.8(e)). The fewer oscillations observed in the estimated frequency are due to the utility frequency variation (± 0.2 Hz). The unitary three-phase system obtained, shown in Figure 4.8(c), is used to detect the phase angle by means of a PLL. The estimated phase angle is shown in Figure 4.8(f). From this result, it is apparent that the phase angle is well estimated and is given in the line form. This result proves the good performance of the proposed Adaline strategy under normal operating conditions.

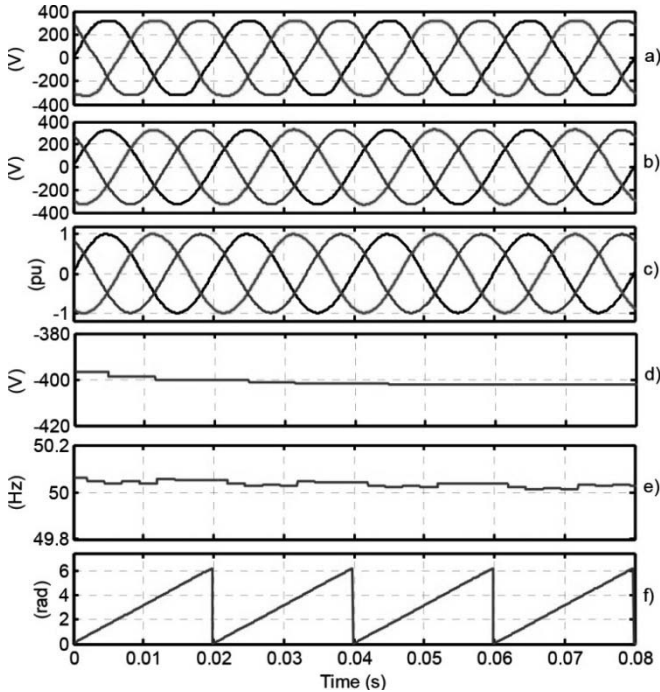


Figure 4.8. Adaline method performances in normal operating conditions:
 a) grid voltages; b) filtered grid voltages; c) unitary three-phase system;
 d) voltage vector amplitude; e) frequency; f) phase angle

Figure 4.9 shows a comparison of performances between the conventional PLL and the proposed Adaline approach under 50% voltage sag in grid voltages. At time $t = 0.63$ s, a voltage sag appears in the measured voltages (Figure 4.9(a)). The adaptive filters based Adaline follows the grid voltages change perfectly and accurately estimates the positive-sequence voltages in 0.1 s after a disturbance appearance (Figure 4.9(b)). The unitary three-phase system has also been reconstructed in 0.1 s after the initiation of disturbance (Figure 4.9(c)). The voltage vector amplitude is estimated with high precision using the Adaline method compared to the conventional PLL (Figure 4.9(d)). Indeed, the signal obtained from the conventional PLL presents considerable fluctuation around its average value. However, in the case of the Adaline method, a transient state is observed in the amplitude estimation, which is due to the adaptation of Adaline weights and the learning process following the change in grid voltages. Similarly, it is also observed that the estimated utility frequency from the conventional PLL, shown in Figure 4.9(e), faces considerable fluctuation compared to the signal obtained from the Adaline method, which remains insensitive to the disturbance. The phase angle

obtained from the two experimented methods is shown in Figure 4.9(f). The estimated phase angle from the Adaline method remains insensitive to the disturbance. However, the estimated phase angle from the conventional PLL is distorted since it is directly calculated from the estimated frequency. Consequently, the proposed Adaline strategy proves its robustness compared to the conventional PLL under voltage sag in grid voltages.

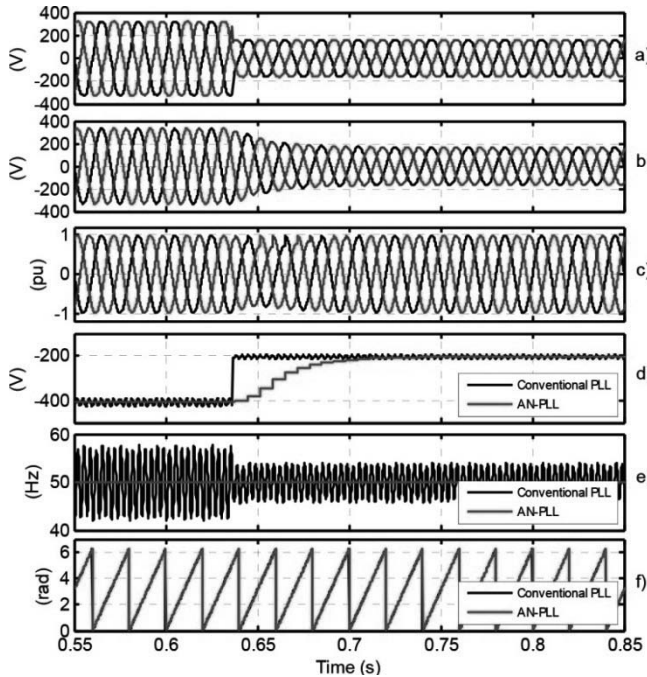


Figure 4.9. Comparison between the conventional PLL and the AN-PLL under 50% voltage sag in grid voltages: a) grid voltages; b) filtered grid voltages; c) unitary three-phase system; d) voltage vector amplitude; e) frequency; f) phase angle

4.5. Adaline for voltage component extraction in unbalanced system

New decomposition of the currents, voltages or powers in power system problems is important in the sense that it changes the point of view of the problem and thus brings new solutions. A new decomposition was also proposed in [OUL 05a] to recover the voltage components, i.e. the direct, inverse and homopolar voltage components. The decomposition is learned with Adaline neural networks and good results were obtained.

4.5.1. Model of the unbalanced voltage system

The three voltages of a three-phase unbalanced power system can also be expressed with the direct, inverse and homopolar voltage components, v_d , v_i and v_o , respectively:

$$v_d = V_d \sqrt{2} \cdot C_{32} \cdot P(\theta_d) \begin{bmatrix} 1 \\ 0 \\ 0 \end{bmatrix} \quad [4.7]$$

$$v_i = V_i \sqrt{2} \cdot C_{32} \cdot P(-\theta_i) \begin{bmatrix} 1 \\ 0 \\ 0 \end{bmatrix} \quad [4.8]$$

$$v_o = \frac{1}{3}(v_1 + v_2 + v_3) \cdot C_{31} \quad [4.9]$$

where V_d , θ_d , V_i , θ_i , V_o and θ_o are, respectively, the amplitude and the phase of the direct, inverse and homopolar voltage components. Equations [4.7]–[4.9] use the general expression of the Clarke and Concordia transforms with the following parameters:

$$P(\theta) = \begin{bmatrix} \cos(\theta) & -\sin(\theta) \\ \sin(\theta) & \cos(\theta) \end{bmatrix}$$

$$C_{32} = \begin{bmatrix} 1 & 0 \\ -1/2 & \sqrt{3}/2 \\ -1/2 & -\sqrt{3}/2 \end{bmatrix}, \quad C_{31} = \begin{bmatrix} 1 \\ 1 \\ 1 \end{bmatrix}, \quad C_{32}^T \cdot C_{31} = \begin{bmatrix} 0 \\ 0 \\ 0 \end{bmatrix}$$

If ω represents the (theoretical) pulsation of the power system, the instantaneous phases of the voltage components, θ_d , θ_i and θ_o , can be expressed through ω and the phases ϕ_d , ϕ_i and ϕ_o , which are due to the unbalancing of the system:

$$\theta_d = \omega t - \phi_d$$

$$\theta_i = \omega t - \phi_i$$

$$\theta_o = \omega t - \phi_o$$

The voltage measured on the nonlinear load, v_L , can be expressed with:

$$v = v_d + v_i + v_o$$

and can be written with v_{L1} , v_{L2} and v_{L3} as follows:

$$v_{L1} = V_d \sqrt{2} \cos(\theta_d) + V_i \sqrt{2} \cos(\theta_i) + V_0 \sqrt{2} \cos(\theta_0)$$

$$\begin{aligned} v_{L2} = & V_d \sqrt{2} \cos(\theta_d - 2\pi/3) + V_i \sqrt{2} \cos(\theta_i - 2\pi/3) \\ & + V_0 \sqrt{2} \cos(\theta_0) \end{aligned}$$

$$\begin{aligned} v_{L3} = & V_d \sqrt{2} \cos(\theta_d + 2\pi/3) + V_i \sqrt{2} \cos(\theta_i + 2\pi/3) \\ & + V_0 \sqrt{2} \cos(\theta_0) \end{aligned}$$

4.5.2. Extraction of the voltage components in the DQ-space

The objective now consists of extracting the amplitudes V_d and V_i and the phases θ_d and θ_i . The amplitude and phase of the homopolar component can then be deduced from [4.9].

As known, the AC component can easily be separated from the DC component in the DQ -space. The voltage of the nonlinear load v_L will thus be expressed in the DQ -space.

The voltages of the power system, represented by the direct and inverse voltage components, are first converted in the $\alpha\beta$ -space with the Concordia transform:

$$\begin{bmatrix} v_\alpha \\ v_\beta \end{bmatrix} = T_{32}^T \cdot v_L = V_d \sqrt{3} \cdot P(\theta_d) \cdot \begin{bmatrix} 1 \\ 0 \end{bmatrix} + V_i \sqrt{3} \cdot P(\theta_i) \cdot \begin{bmatrix} 1 \\ 0 \end{bmatrix} \quad [4.10]$$

The voltages v_α and v_β are then converted in the DQ -space with the Park transform with an angle $-\hat{\theta}_d$. The direct components on the DQ -voltages are thus given by:

$$\begin{bmatrix} v_D^d \\ v_Q^d \end{bmatrix} = P(-\hat{\theta}_d) \cdot \begin{bmatrix} v_\alpha \\ v_\beta \end{bmatrix} = \begin{bmatrix} V_d \sqrt{3} \cos(\theta_d - \hat{\theta}_d) + V_i \sqrt{3} \cos(-\theta_i - \hat{\theta}_d) \\ V_d \sqrt{3} \sin(\theta_d - \hat{\theta}_d) + V_i \sqrt{3} \sin(-\theta_i - \hat{\theta}_d) \end{bmatrix} \quad [4.11]$$

The inverse components on the DQ -voltages are calculated with the Park transform with an angle $\hat{\theta}_i$, and thus:

$$\begin{bmatrix} v_D^i \\ v_Q^i \end{bmatrix} = P(\hat{\theta}_i) \cdot \begin{bmatrix} v_\alpha \\ v_\beta \end{bmatrix} = \begin{bmatrix} V_d \sqrt{3} \cos(\theta_d + \hat{\theta}_i) + V_d \sqrt{3} \cos(-\theta_i + \hat{\theta}_i) \\ V_i \sqrt{3} \sin(\theta_d + \hat{\theta}_i) + V_i \sqrt{3} \sin(-\theta_i + \hat{\theta}_i) \end{bmatrix} \quad [4.12]$$

The instantaneous phases $\hat{\theta}_d$ and $\hat{\theta}_i$ are estimated online with a voltage-controlled oscillator (VCO) block. We can see that an estimation $\hat{\theta}_d$ very close to θ_d leads to:

$$\begin{bmatrix} v_D^d \\ v_Q^d \end{bmatrix} \approx \begin{bmatrix} V_d \sqrt{3} + V_i \sqrt{3} \cos(-\theta_i - \hat{\theta}_d) \\ V_i \sqrt{3} \sin(-\theta_i - \hat{\theta}_d) \end{bmatrix} \quad [4.13]$$

In the same way, if $\hat{\theta}_i$ is very close to θ_i , then:

$$\begin{bmatrix} v_D^i \\ v_Q^i \end{bmatrix} = \begin{bmatrix} V_d \sqrt{3} \cos(\theta_d + \hat{\theta}_i) + V_d \sqrt{3} \\ V_i \sqrt{3} \sin(\theta_d + \hat{\theta}_i) \end{bmatrix} \quad [4.14]$$

In [4.13], the terms depending on $(-\theta_i - \hat{\theta}_d)$ are time-varying and represent the AC components of the direct voltages v_D^d and v_Q^d in the DQ -space. On the other side, $V_d \sqrt{3}$ that is present in v_D^d is a DC component. Thus, by separating the AC component from the DC component of v_D^d , we can extract the real value of V_d .

In [4.14], the terms depending on $(\theta_d + \hat{\theta}_i)$ are time-varying and represent the AC components of the direct voltages v_D^i and v_Q^i in the DQ -space. $V_i \sqrt{3}$ is present in v_D^i and is a DC component. Thus, by separating the AC component from the DC component of v_D^i , we can extract the real value of V_i .

The complete Adaline-based decomposition, which is used to estimate the amplitudes V_d and V_i , is shown in detail in Figure 4.10. This block diagram needs online estimates of the instantaneous phases θ_d and θ_i .

4.5.3. Online estimation of the instantaneous phases θ_d and θ_i

The design of the estimation of the instantaneous phases θ_d and θ_i relies on well-known clock extraction circuitry. Indeed, a VCO is phase locked to the incoming data stream and runs at the same rate as the input signal. If the data rate fluctuates,

the error voltage from the phase detector will cause the oscillator to shift in frequency and “follow” the data. Adjustment of the loop gain in the PLL structure will control how fast and how far the incoming data can deviate from its nominal rate without preventing the VCO from tracking. Clock extraction circuits are often based on a PLL architecture, which includes a phase detector and a VCO. Conventional and enhanced PLL can be used [ALA 01] and we have also shown that neural networks can be used [OUL 05a].

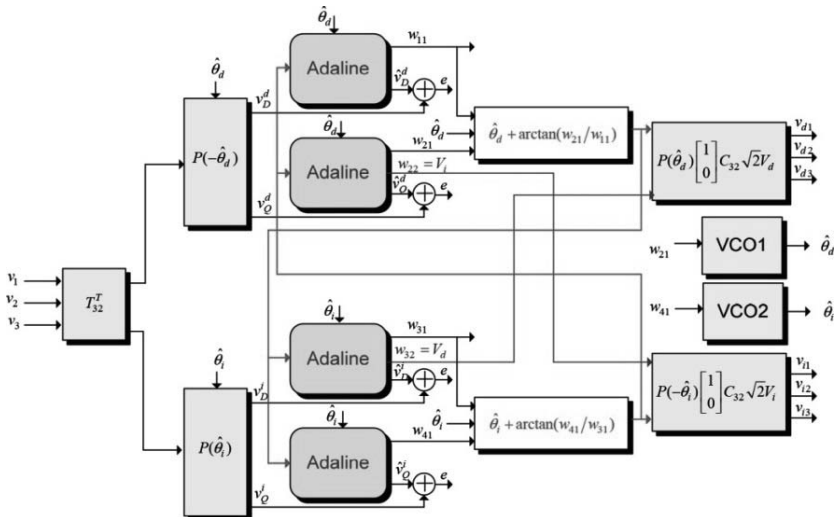


Figure 4.10. Block diagram of the extraction of the direct and inverse voltage components with the Adaline-based approach

A VCO compatible with the real-time constraint is used to deliver online the values $\hat{\theta}_d$ and $\hat{\theta}_i$ at different level as shown in Figure 4.10.

4.5.4. Filtering the AC components in the DQ-space

Separation of the AC component from the DC component can be done with conventional low-pass filters. We also propose to use Adaline neural networks for different reasons: their self-adjustment capabilities and their robustness. Moreover, we also want an active power filter (APF) based on a homogeneous computational structure composed of only neural units working in parallel, i.e. with Adalines. We first introduce the use of low-pass filters and then detail the Adaline-based filtering scheme.

1) *Filtering with low-pass filters*

Signals from [4.13] and [4.14] are filtered with four power low-pass filters in order to separate the AC-voltage component from the DC-voltage component. The order of the filters determines the dynamics and the efficiency of the whole method. We choose second-order filters to achieve the best compromise between total performance and computational cost. Indeed, higher order filters represent computational costs not compatible with a hardware implementation for an online application. The cutoff frequency, $f_0 = \omega_0/2\pi$, is chosen to separate the terms $V_d\sqrt{3}$ and $V_i\sqrt{3}$ from the AC-voltage components.

2) *Filtering with Adalines*

In this neural approach, both expressions [4.13] and [4.14] are proposed to be learned with Adalines. If we consider the DQ -space, the two direct voltage components given by [4.13] can be written with vectorial notations as follows:

$$\begin{bmatrix} v_D^d \\ v_Q^d \end{bmatrix} = \begin{bmatrix} W_D^{d^T} X_D^d(t) \\ W_Q^{d^T} X_Q^d(t) \end{bmatrix} \quad [4.15]$$

The two inverse voltage components given by [4.14] can be written in the DQ -space with vectorial notations as follows:

$$\begin{bmatrix} v_D^i \\ v_Q^i \end{bmatrix} = \begin{bmatrix} W_D^{i^T} X_D^i(t) \\ W_Q^{i^T} X_Q^i(t) \end{bmatrix} \quad [4.16]$$

The two previous expressions use the following vectors:

$$W_D^{d^T} = \begin{bmatrix} V_d \sqrt{3} \cos(\theta_d - \hat{\theta}_d) & v_i \end{bmatrix} \quad [4.17]$$

$$W_Q^{d^T} = \begin{bmatrix} V_d \sqrt{3} \sin(\theta_d - \hat{\theta}_d) & v_i \end{bmatrix} \quad [4.18]$$

$$X_D^d(t) = \begin{bmatrix} 1 \\ \sqrt{3} \cos(-\theta_i - \hat{\theta}_d) \end{bmatrix} \quad [4.19]$$

$$X_Q^d(t) = \begin{bmatrix} 1 \\ \sqrt{3} \sin(-\theta_i - \hat{\theta}_d) \end{bmatrix} \quad [4.20]$$

Each component, v_D^d , v_Q^d , v_D^i and v_Q^i , is learned with an Adaline. Vectors \mathbf{W}_D^d , \mathbf{W}_Q^d , \mathbf{W}_D^i and \mathbf{W}_Q^i represent the weights, while $\mathbf{X}_D^d(t)$, $\mathbf{X}_Q^d(t)$, $\mathbf{X}_D^i(t)$ and $\mathbf{X}_Q^i(t)$ are the inputs of the Adalines.

We learn the resulting linear expressions, [4.15] and [4.16], by the Adalines. The Adalines are trained by an online learning process based on the LMS learning rule. We used the modified LMS learning rule given by [4.21] to update the weight $\mathbf{W}(k)$, where the index k corresponds to the instant kT (T is the sampling period), α is the learning rate of the neuron, e is the error between the output of the neuron and the desired output ($e = y_d - y$) and $\mathbf{X}(k)$ is the input vector:

$$\mathbf{W}(k+1) = \begin{cases} \mathbf{W}(k) + \frac{\alpha e(k) \mathbf{Y}(k)}{\lambda + \mathbf{X}^T(k) \mathbf{Y}(k)}, & \text{if } \mathbf{X}^T(k) \mathbf{Y}(k) \neq 0 \\ \mathbf{W}(k) & \text{if } \mathbf{X}^T(k) \mathbf{Y}(k) = 0 \end{cases} \quad [4.21]$$

where $\mathbf{Y}(k) = 1/2 (\text{sgn}(\mathbf{X}(k)) + \mathbf{X}(k))$ and λ is an appropriate not-null constant to ensure [4.21] avoids a division by zero. Adalines are thus very simple and powerful neural networks. Online learning can be achieved to estimate V_d , V_i , θ_d and θ_i , and this neural architecture is well suited for a real-time hardware implementation.

3) Discussion

Finally, the homopolar voltage component v_o defined by V_o and θ_o can be deduced from the estimated values of V_d , V_i , θ_d and θ_i through expression [4.9].

This neural method is different with the one proposed in [OUL 05a]. If both methods are based on Adaline neural networks and online learning, each neural method relies on a different original decomposition of the voltages. Moreover, the new neural method is able to estimate the frequency online and, on the other hand, the approach in [OUL 05] needs an online frequency estimation. This can be done by either estimating the frequency with a VCO/PLL or estimating the frequency with a neural approach as proposed in [OUL 05b].

This neural method has numerous advantages over a conventional PLL and also over the PLL enhanced with an pole placement with R, S and T (RST) controller and proposed in [ALA 01]. While PLLs can only compensate for some small deviations from a nominal frequency, the new neural method is able to compensate for and follow every frequency fluctuation, even sudden changes. While PLLs can only

estimate the direct voltage component, the new neural method is able to estimate the direct, inverse and homopolar voltage components.

4.5.5. Results

1) Simulation results

The direct, inverse and homopolar voltage components are first extracted in simulation. An electrical network with a three-phase power supply is simulated with a frequency of 50 Hz and a sample period $T = 0.5$ ms. A nonlinear load with resistive and capacitive parts is also simulated ($R_L = 2\Omega$ and $C_L = 45$ mF). The new neural method is used to estimate online the different voltage components even while the nonlinear load is changed or even while the frequency suddenly changes. We also propose to compare the results with those obtained with a PLL enhanced with an RST controller as proposed in [ALA 01] and with those obtained with the neural approach introduced in [OUL 05a]. The PLL method will serve as a reference in terms of performance. We used a constant learning rate $\mu = 0.008$ and $\lambda = 0.01$ for the proposed neural approach.

At first, the three-phase power system is balanced with only a direct voltage component, i.e. with a null inverse voltage component. After 1.4 s, the power supply is disturbed by the nonlinear load, the direct voltage component is reduced from 25% and a non-zero inverse voltage component is introduced, thus resulting in a non-zero homopolar voltage component and in an unbalanced system. After this instant, the electrical network parameters are: $V_d = 0.75 \times 230\sqrt{2}$ V, $V_i = 0.25 \times 230\sqrt{2}$ V, $V_o = 50$ V and $\theta_d = \pi/2$ rds, $\theta_i = \pi/3$ rds and $\theta_o = \pi/5$ rds. We can note that these conditions are very improper and unfavorable.

The parameters of the direct and inverse voltage components, V_d , V_i , θ_d and θ_i , are estimated online with the new neural method and the results are shown by Figure 4.11. It can be seen that the method is able to compensate for the changes due to the variation of the nonlinear load. The estimation of V_d , V_i , θ_d and θ_i is used to estimate online V_o and ϕ_o , and also v_d , v_i and v_o . These voltage components are shown in Figure 4.12. The proposed Adaline strategy succeeded in detecting the transient and in identifying the effects resulting from the nonlinear load changes. The proposed Adaline strategy can be considered as fast. Figure 4.13 shows the online estimation of the direct component V_d with the different methods. We can clearly see that the proposed neural method is the faster one. Indeed, the estimation of the direct voltage component is done after 3.3 ms with the new Adaline strategy against 20.6 ms with the neural approach given in [OUL 05a] and 46.6 ms with the enhanced PLL.

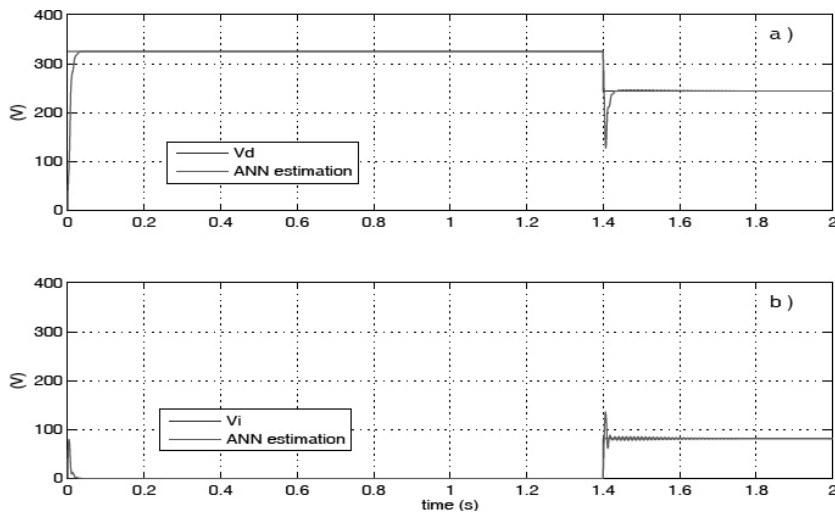


Figure 4.11. Online estimation of the voltage components with the new Adaline-based approach: a) the direct component and b) the inverse component

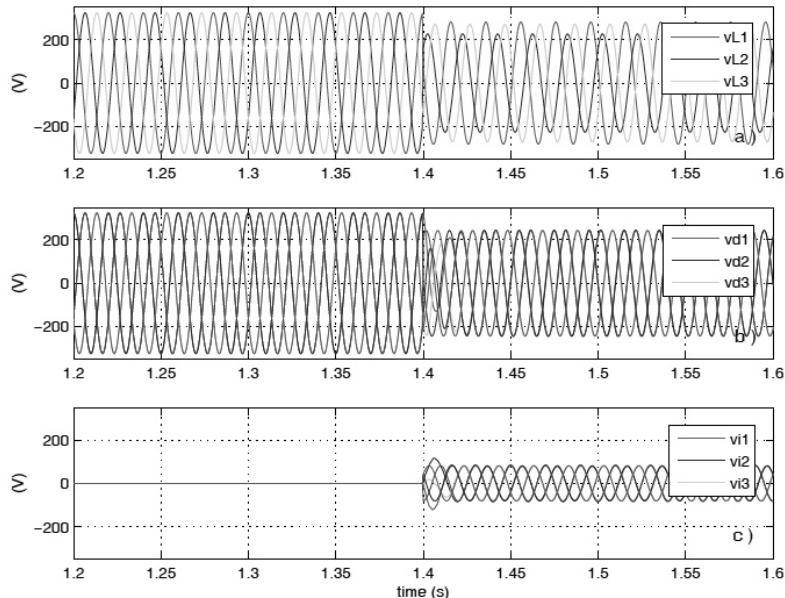


Figure 4.12. Waveforms of the voltage components estimated online by the new neural approach: a) direct component, b) inverse component and c) homopolar component

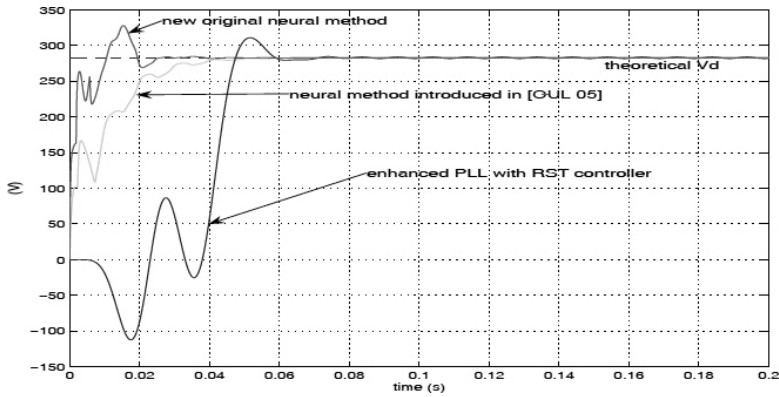


Figure 4.13. Comparison in estimating the direct voltage component V_d with several methods

The proposed neural approach is able to compensate not only for the variation of the nonlinear load but also for other changing parameters. We now propose to estimate the voltage components when the frequency suddenly changes. Figure 4.14 shows the frequency of the previous unbalanced system, which suddenly increases from 50 to 51 Hz at 1.4 s. This figure also shows the estimated frequency that is deduced from the proposed neural approach. Indeed, ω is obtained with the estimated value of θ_a . We can clearly note that the proposed neural approach instantaneously follows the sudden change of the frequency.

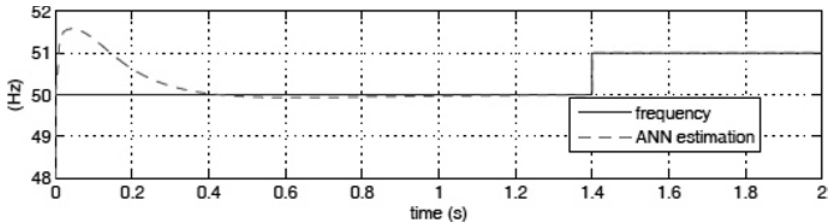


Figure 4.14. Online estimation of the frequency with the new Adaline-based approach

2) Experimental results

Experimental results are now given to illustrate the performance of the Adaline-based method to extract the voltage components online from an electrical three-phase power system. The experimental setup is composed of a three-phase power supply with low voltages (100 V) and a nonlinear load, i.e. a Graetz bridge of six valve functions and an RL-circuit and a power variator. The voltage component extractor is implemented on a DS 1104 DSPACE board, the sample period in all the

experiments is $T = 0.5$ ms. This experimental platform thus reproduces exact industrial conditions. Several experiments have been conducted in order to evaluate the proposed neural architecture. Results are shown in Figure 4.15. We can see the voltage v_L measured at the nonlinear load under an unbalanced condition and the direct voltage component v_d estimated with the proposed neural approach. The Adalines succeeded well in estimating the voltage component parameters.

The new neural approach has been evaluated in more severe cases; for example, when the nonlinear load changes during time or when important distortion harmonics are present. This second case is illustrated in Figure 4.16, which shows the voltage v_L measured at the nonlinear load and the estimated direct voltage v_d . We can see the voltage of the unbalanced system disturbed by distortion harmonics up to rank 11 and the efficiency of the neural approach to estimate online the voltage components.

The experiments demonstrate the efficiency and robustness of the Adaline approach to estimate online the voltage components, i.e. the direct, inverse and homopolar components. All the experiments also prove that the neural approach is well suited to a hardware real-time application.

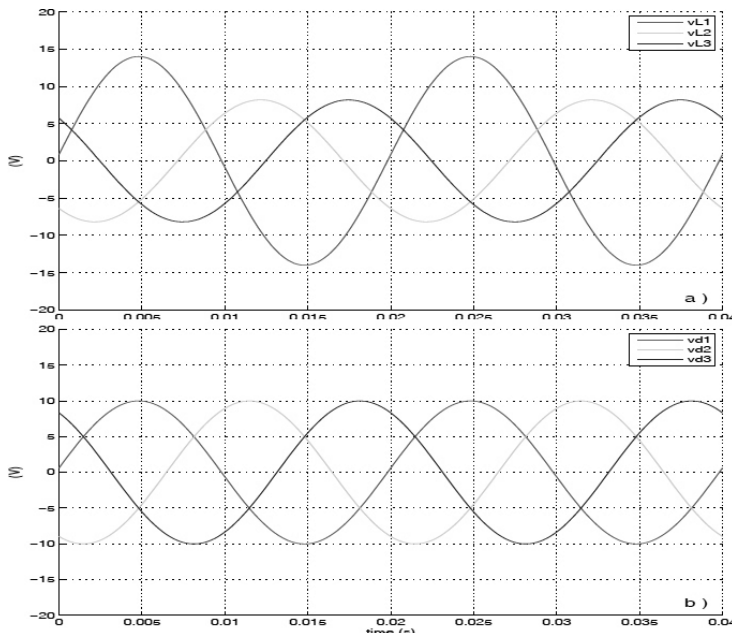


Figure 4.15. Experimental voltage waveforms of a three-phase system under an unbalanced load condition: a) v_L measured on the nonlinear load, b) direct voltage v_d estimated with the proposed Adaline-based approach

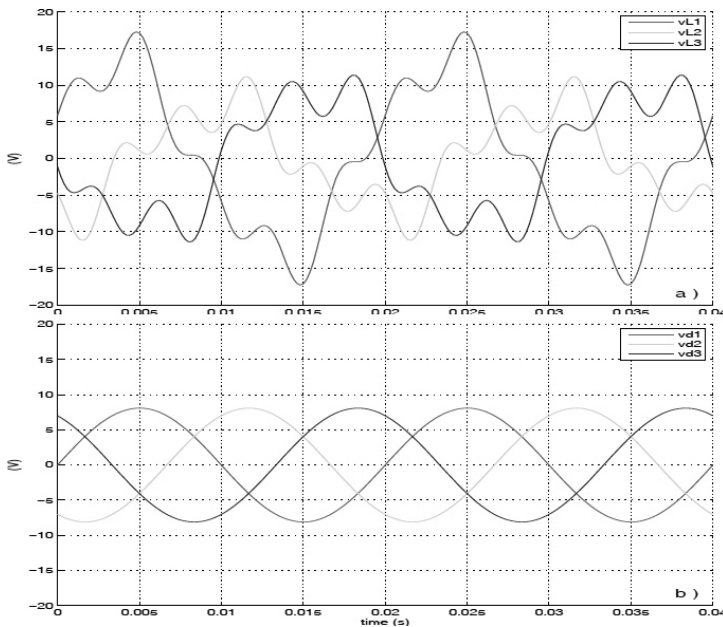


Figure 4.16. Experimental voltage waveforms of a three-phase system disturbed with harmonics and under an unbalanced load condition: a) v_L measured on the nonlinear load, b) direct voltage v_d estimated with the proposed Adaline-based approach

4.6. Adaline for harmonic current identification and compensation

For a few years, the cognitive sciences have hoped to improve the abilities and performances of systems using ANNs. In this work, ANNs are used to identify and compensate harmonics distortions in electrical power systems. Indeed, many harmonics distortions are present in electrical power systems due to time-varying nonlinear loads (rectifiers, variable speed transmissions, lighting, etc.).

Harmonics distortions are compensated for by the use of advanced techniques [ALA 00] such as APFs. These techniques can be favorably inserted into existing power systems to compensate for harmonics distortions.

The performances in terms of harmonic compensation strongly depend on the selected identification method. Indeed, an efficient control device will not be able to make the sufficient corrections if the harmonic currents are incorrectly identified. For this reason, we tested and used three different methods to identify these harmonics. The originality of this work consists of finding an adequate decomposition of the signal for the input of our neural network.

The first method uses the Fourier signal decomposition of the currents, measured on each phase. This decomposition can be used directly as inputs of an Adaline neural network. The second method represents an original approach of identification valid for three-phase and single-phase applications [TEP 96]. It uses two Adalines for each phase in order to separate the harmonics from the fundamental signal. A Fourier series decomposition of our signal makes it possible to define the neural network inputs. An LMS algorithm carries out the weights training. The facility of use, as well as the parallel unfolding of computations, makes this approach fast and effective. The third method exploits the instantaneous real and imaginary powers technique that is largely used in active filtering systems. In [OUL 04], we replaced the low-pass filter by two Adalines. Significant improvements were obtained in simulations and on real applications, but the method is applicable only for the three-phase systems.

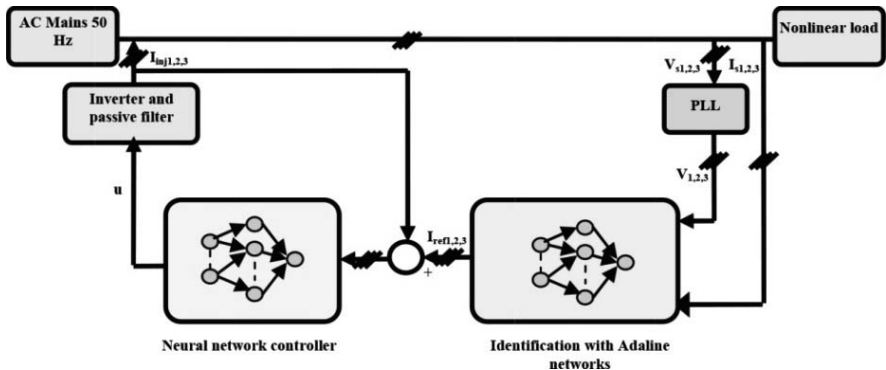


Figure 4.17. Neural APFs general structure

The harmonics compensation in the electrical supply network is done in two stages (Figure 4.17). The first stage uses an identifying module to find out the harmonics of the currents and the second stage injects these harmonics in the electrical supply network. The second stage strongly depends on the first stage. Indeed, if the harmonic currents are badly identified, this inevitably involves a lower quality of the compensation. We use a neural control scheme [OUL 05c] to inject the harmonics into the electrical supply network and a PLL to compute the instantaneous real and imaginary powers.

Traditional technical tools for harmonic distortion analysis using either fast Fourier transform (FFT) or discrete Fourier transform (DFT) are, however, susceptible to compensate for the presence of noise or subharmonics in the distorted signals. Harmonic detection by using the Fourier transformation also requires input

data for one more cycle of the current waveform and requires time for the analysis in the next coming cycle. As an alternative, methods using ANNs achieve satisfactory results for fast and precise harmonic detection in noisy environments [LIN 05].

4.6.1. Adaline method

The simple structure of Adaline neural networks allows us to physically interpret the weights and thus makes them very powerful in the field of adaptive filtering. In harmonics distortions compensation, Adaline neural networks are used to identify and estimate the harmonics components of the currents in electrical supply networks. Each harmonics component of the current can be estimated with one Adaline's weight. We use this principle and propose three different techniques.

1) The “direct” method

In this technique, the identification and filtering are carried out in the space of the currents (the three-phase space). By measuring the current of the three phases of the electrical supply network, each phase can be decomposed into Fourier series in the following way:

$$I_s(t) = I_{sf}(t) + I_{sh}(t) = I_{11} \cos(\omega t - \alpha) + I_{12} \sin(\omega t - \alpha) + \sum_{n=2,\dots,N} [I_{n1} \cos n(\omega t - \alpha) + I_{n2} \sin n(\omega t - \alpha)] \quad [4.22]$$

where

$$I_{sf}(t) = I_{11} \cos(\omega t - \alpha) + I_{12} \sin(\omega t - \alpha), \text{ and}$$

$$I_{sh}(t) = \sum_{n=2,\dots,N} [I_{n1} \cos n(\omega t - \alpha) + I_{n2} \sin n(\omega t - \alpha)]$$

In the previous equations, ω is the fundamental frequency, α is the phase between current and load voltages, I_{11} and I_{12} are the cosine and sine frequency components of fundamental current, and I_{n1} and I_{n2} are the cosine and sine frequency components of the harmonic current.

The identification of the harmonics components is done with an Adaline for each phase. As shown in Figure 4.18, the Adaline takes cosine and sine terms resulting from the decomposition into Fourier series of the measured current as the inputs (except for a constant term corresponding to a bias). The expression of the current, i.e. [4.22], can thus be written as a linear combination that can be learned by an Adaline network:

$$I_s(t) = W^T \cdot x(t) \quad [4.23]$$

In this expression, W^T is the Adaline weight vector and $x(t)$ is the network input vector composed of the cosine and sine components of the harmonics of different orders:

$$W^T = [I_{11} \quad I_{12} \quad \dots \quad I_{n1} \quad I_{n2}], \text{ and}$$

$$x(t) = [\cos(\omega t - \alpha) \quad \sin(\omega t - \alpha) \quad \dots \quad \cos n(\omega t - \alpha) \quad \sin n(\omega t - \alpha)]$$

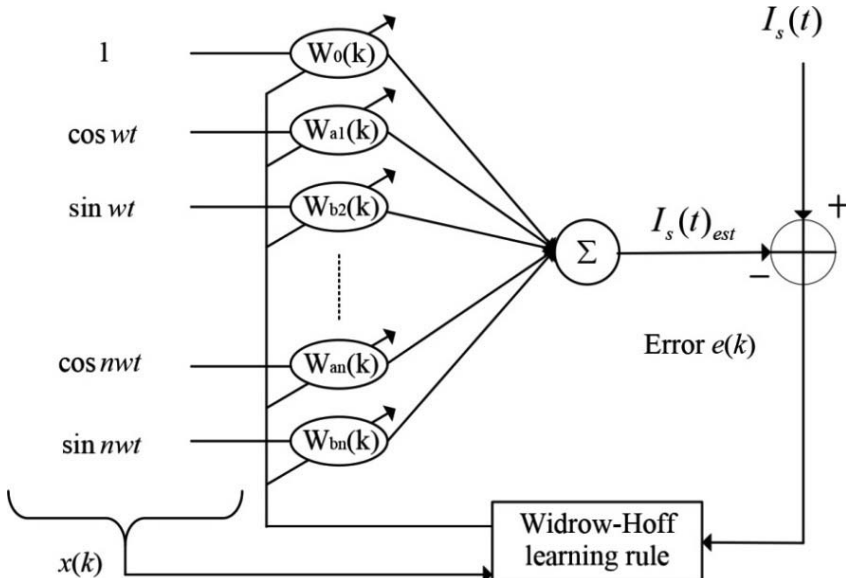


Figure 4.18. Design of the Adaline network for harmonic distortion identification ("direct" method)

The estimated fundamental current is then recovered as follows: $I_{sf}(t) = W_{a1} \cos \omega t + W_{b1} \sin \omega t$, where W_{a1} and W_{b1} represent the weights of the Adaline associated with the cosine and sine terms of the fundamental current. The difference between this estimated current and the measured current gives the sum of the different harmonics components, and a reference current can thus be provided. We propose to apply this method with a modified Widrow–Hoff learning rule to adapt the weights of the Adalines.

2) The three-monophase method

The three-monophase method works directly in the currents space and uses two Adalines to identify the harmonics for each phase. The details of the decomposition of the current $I_s(t)$ can be found in [OUL 05d].

Let us consider the current $I_s(t)$ of equation [4.22] absorbed by the nonlinear load on the first phase (for $\alpha = 0$). By multiplying equation [4.22], respectively, with $\sin \omega t$ and $\cos \omega t$, we obtain the following expressions:

$$I_s(t) \sin \omega t = \frac{1}{2} \left[I_{12} - I_{12} \cos 2\omega t + I_{11} \sin 2\omega t + \sum_{n=2 \dots N} \left(\frac{I_{n2}}{I_{n1}} \cos(n-1)\omega t - \frac{I_{n2}}{I_{n1}} \cos(n+1)\omega t + \frac{I_{n1}}{I_{n2}} \sin(n+1)\omega t - \frac{I_{n1}}{I_{n2}} \sin(n-1)\omega t \right) \right] \quad [4.24]$$

$$I_s(t) \cos \omega t = \frac{1}{2} \left[I_{11} - I_{12} \sin 2\omega t + I_{11} \cos 2\omega t + \sum_{n=2 \dots N} \left(\frac{I_{n2}}{I_{n1}} \sin(n+1)\omega t - \frac{I_{n2}}{I_{n1}} \sin(n-1)\omega t + \frac{I_{n1}}{I_{n2}} \cos(n-1)\omega t - \frac{I_{n1}}{I_{n2}} \cos(n+1)\omega t \right) \right] \quad [4.25]$$

In these relations, only terms representing the continuous components are proportional, respectively, to the amplitude of the fundamental active current I_{12} and to the amplitude of the fundamental reactive current I_{11} . Expressions [4.24] and [4.25] can both be written as a linear combination that can be learned separately by two Adaline networks: $I_s(t) \sin \omega t = W^T \cdot x(t)$ and $I_s(t) \cos \omega t = W^T \cdot x(t)$.

In these two expressions, W^T represents the weight vector and $x(t)$ is the input vector composed of the cosine and sine components of the harmonics of different orders. For $I_s(t) \sin \omega t = W^T \cdot x(t)$, we have:

$$W^T = [I_{12} \quad -I_{12} \quad I_{11} \quad \dots \quad I_{n2} \quad -I_{n2} \quad I_{n1} \quad -I_{n1} \quad \dots], \text{ and}$$

$$x(t)^T = 1/2 [1 \quad \cos 2\omega t \quad \sin 2\omega t \quad \dots \quad \cos(n-1)\omega t \quad \cos(n+1)\omega t \quad \sin(n+1)\omega t \quad \sin(n-1)\omega t \quad \dots]$$

For the second relation, i.e. $I_s(t) \cos \omega t = W^T \cdot x(t)$, we have:

$$W^T = [I_{11} \quad -I_{12} \quad I_{11} \quad \dots \quad I_{n2} \quad -I_{n2} \quad I_{n1} \quad -I_{n1} \quad \dots]$$

$$\begin{aligned}x(t)^T = 1/2[1 & \sin 2\omega t & \cos 2\omega t & \dots \\& \dots & \sin(n+1)\omega t & \sin(n-1)\omega t & \cos(n-1)\omega t & \cos(n+1)\omega t & \dots]\end{aligned}$$

The amplitude of the continuous component of the fundamental active current will be determined by the weight $W_0(k)$ of the first Adaline neural network. The continuous component of the reactive current will also be calculated by the weight $W_0(k)$ of the second Adaline neural network. The reconstituted fundamental current is obtained by multiplying, respectively, I_{11} and I_{12} with $\cos \omega t$ and $\sin \omega t$:

$$I_{sf}(t) = I_{11} \cos \omega t + I_{12} \sin \omega t.$$

The harmonic current of each phase is given by the relation:
 $I_{sh}(t) = I_s(t) - I_{sf}(t).$

The complete scheme of the estimation of the fundamental current $I_{sf}(t)$ and of the harmonic current $I_{sh}(t)$ for one phase is shown in Figure 4.19.

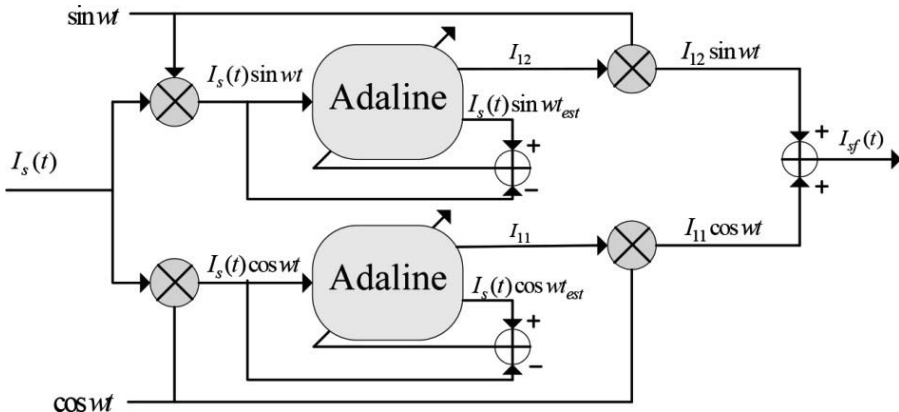


Figure 4.19. Basic principle of the three-monophase method

3) The active and reactive powers method

Conversion of the measured currents into the active and reactive powers is conventionally achieved by the direct Concordia transform. We propose to use this

transform in a new method, the active and reactive powers method, which decomposes the powers as follows [OUL 04]:

$$p(t) = \underbrace{p_1 \cos \beta + p_5 \cos(6\omega t - 5\beta)}_{\tilde{p}} - \underbrace{p_7 \cos(6\omega t - 7\beta)}_{\tilde{p}} - \dots \quad [4.26]$$

$$q(t) = \underbrace{-q_1 \sin \beta - q_5 \sin(6\omega t - 5\beta)}_{\tilde{q}} - \underbrace{q_7 \sin(6\omega t - 7\beta)}_{\tilde{q}} + \dots \quad [4.27]$$

Both signals given in equations [4.26] and [4.27] can be written with the vector notation in the following discrete general form:

$$A_0 + \sum_{n=1,\dots,N} \begin{pmatrix} A_{1n} \cos(n\omega t - (n-1)\beta) \\ + A_{2n} \cos(n\omega t - (n+1)\beta) \\ + B_{1n} \sin(n\omega t - (n-1)\beta) \\ + B_{2n} (\sin(n\omega t - (n+1)\beta)) \end{pmatrix} = W^T x(t) \quad [4.28]$$

In [4.28], A_0 and the terms A_{1n} , A_{2n} , B_{1n} and B_{2n} are the amplitudes of the cosine and sine components of the n -order harmonics. Thus, the Adaline weight vector is (see Figure 4.20):

$$W^T = [I_{12} \quad -I_{12} \quad I_{11} \quad \dots \quad I_{n2} \quad -I_{n2} \quad I_{n1} \quad -I_{n1} \quad \dots]$$

The Adaline network input vector is then composed of the cosine and sine components of the n -order harmonics:

$$\begin{aligned} x(t)^T = & [1 \quad \cos(6\omega t - 5\beta) \quad \sin(6\omega t - 5\beta) \quad \cos(6\omega t - 7\beta) \quad \sin(6\omega t - 7\beta) \quad \dots \\ & \dots \quad \cos(n\omega t - (n-1)\beta) \quad \sin(n\omega t - (n-1)\beta) \quad \cos(n\omega t - (n+1)\beta) \\ & \quad \sin(n\omega t - (n+1)\beta)] \end{aligned}$$

Two Adalines are thus employed to identify and separate the alternative components \tilde{p} and \tilde{q} from the continuous components \bar{p} and \bar{q} [TEP 96]. The biases of the two neural networks identify the continuous components of the active and reactive powers. An inverse Concordia transform enables then to find out the harmonic currents from the power alternative components. This method should give better results than the direct method due to the precision to obtain the continuous components.

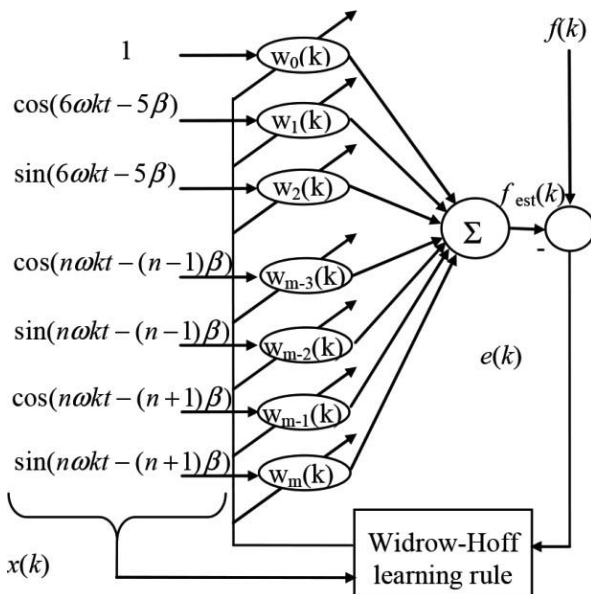


Figure 4.20. Basic principle of the active and reactive powers method

4.6.2. Results

To evaluate the proposed methods, a practical case that is representative of the most common power quality environment was created and simulated in Matlab–Simulink. In the considered power system, the three-phase source has the following characteristics: $R_s = 1,269 \text{ mΩ}$, $L_s = 46.49 \mu\text{H}$, $V_s = 230 \text{ V}$ and $f_c = 50 \text{ Hz}$. To create harmonics distortions, a nonlinear load (a Graetz bridge with RC branches) has been introduced with the following parameters: 100 kVA, $\alpha = 0$, $R_c = 2 \Omega$ and $C_c = 45 \text{ mF}$.

1) Steady-state behavior

To compare these three neural identification methods, we kept the same control device for the three cases. The total harmonic distortion (THD) is measured to show the performances of each technique. We also compared these results with the results obtained with a conventional low-pass filter. The performances of all methods are given in Table 4.1.

From Table 4.1 we can see that the three identification techniques using Adalines give good results compared to the low-pass filter method. The direct method is the simplest in terms of implementation because it does not require any PLL and current transformations. The compensation performances are not the best. On the other

hand, the THD is reduced to 0.79% with the three-monophase method that does not require a PLL but needs current transformations.

Filtering methods	Need for PLL	Need for current transforms	THD in the power supply (for a THD of 24% in the load) (%)
Conventional low-pass filter	Yes	Yes	1.2
“Direct” method	No	No	0.95
Three-monophase method	No	Yes	0.79
Active and reactive powers method	Yes	Yes	0.84

Table 4.1. Comparison of the performances of the different compensation techniques

2) Transient behavior

To evaluate the transient behavior of each method, the nonlinear load is changed at time 0.28 s by adding a resistance in parallel (the global resistance is then changed from 2 to 1 Ω). The performances of each method are evaluated by representing the online corresponding THD in Figure 4.21. This figure shows that the active and reactive powers method is the faster and accurate method to compensate for harmonics distortions when the nonlinear load changes online.

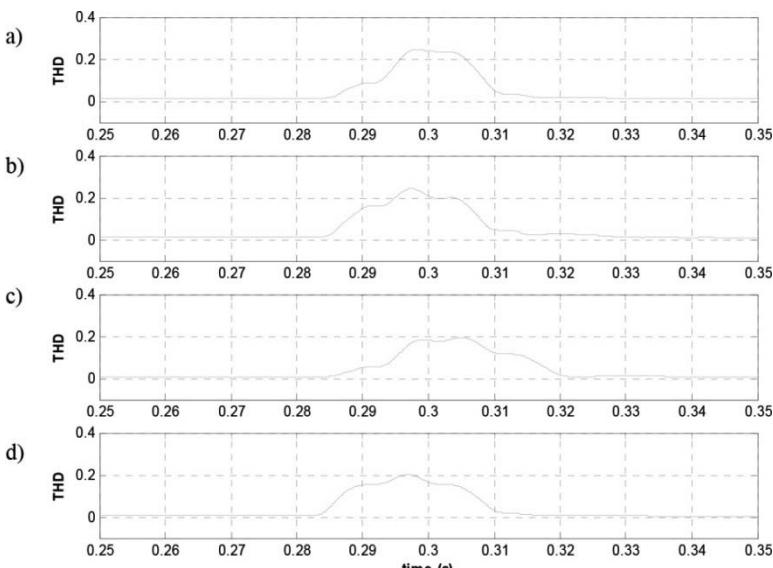


Figure 4.21. Simulation results of using the proposed neural APFs with a time-varying nonlinear load. a) THD with the conventional low-pass filter, b) THD with the “direct” method, c) THD with the three-monophase method and d) THD with the active and reactive powers method

The current of the power system is shown in Figure 4.22 with the active and reactive powers method to compensate for the harmonics distortions. The figure shows the current wave form before and after the compensation and also shows the current resulting from the harmonics distortions while the nonlinear load is online changed at time 0.28 s.

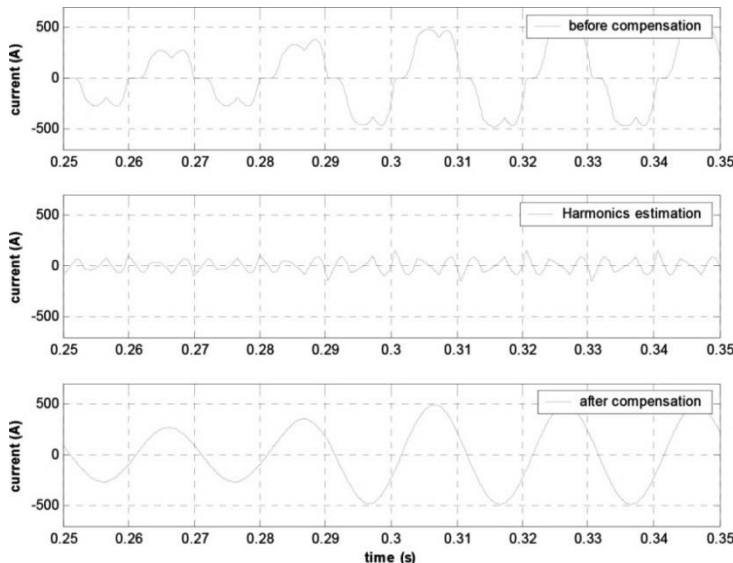


Figure 4.22. Dynamic response of the neural APF using the active and reactive powers method to compensate for the harmonics distortions with a nonlinear load online changed at time 0.28 s

4.7. Conclusion

This chapter has presented and analyzed different methods based on ANNs to identify three electrical events: frequency variation, voltage unbalance and current harmonics in electrical power systems. Each method is different because it is based on a specific decomposition of the current or the voltage signals.

For the first event, a new AN-PLL based on Adaline for grid-connected converter synchronization has been presented for the frequency and phase angle estimation as an alternative to the conventional PLL. The whole AN-PLL architecture is implemented under the dSPACE board and applied to a real power supply in order to prove its efficiency. Thereafter, a comparative experimental study between the proposed AN-PLL and the conventional PLL is also carried out. Compared to the conventional PLL and according to the obtained experimental results, the proposed AN-PLL improves the dynamic and steady-state estimation

performances. Hence, it is a very suitable synchronization system under severe utility conditions.

For the second event related to the voltage unbalance, a neural disturbance detection and identification approach is developed. The approach detects voltage components from unbalanced and perturbed power systems. It is thus well suited for active power filter schemes. On the basis of a new decomposition of the voltages in the DQ -space, linear expressions explicitly separating the AC component from the DC component are learned with Adaline neural networks. By their simplicity and their online learning capabilities, the Adalines allow the proposed approach to be significantly faster and more precise in detecting and discriminating the disturbance events than conventional approaches and other neural approaches. This method was studied and successfully implemented in simulation and in experiments both under stationary and non-stationary conditions. Comparisons demonstrate the effectiveness of the proposed method, especially in the presence of uncertainties, parameter changes and noise perturbations.

Finally, three methods based on Adaline for current harmonics identification have been discussed. The “direct” method simply uses an Adaline to directly estimate the fundamental harmonics of the measured current. A three-monophase method uses two Adalines for each phase to estimate the fundamental harmonics of the measured current. The active and reactive powers method uses an Adaline to estimate the fundamental harmonics of the active and reactive powers. Performances are evaluated and compared with results from the simulations. The effectiveness of these methods and the comparison with other related methods (a conventional low-pass filter) are discussed. We can see that neural compensation methods are more efficient than other conventional methods to compensate for the harmonics distortions in electrical power systems.

4.8. Bibliography

- [ALA 00] ALALI M.A.E., SAADATE S., CHAPUIS Y.A., *et al.*, “Control and analysis of series and shunt active filters with SABER”, *International Power Electronics Conference (IPEC '00)*, Tokyo, Japan, 2000.
- [ALA 01] ALALI M.A.E., SAADATE S., CHAPUIS Y.-A., *et al.*, “Advanced corrector with FPGA-based PLL to improve performance of series active filter compensating all voltage disturbances”, *European Conference on Power Electronics and Applications*, Graz, Austria, 2001.
- [BEC 12] BECHOUCHE A., *et al.*, “A novel method for identifying parameters of induction motors at standstill using ADALINE”, *IEEE Transactions on Energy Conversion*, vol. 27, no. 1, pp. 105–116, March 2012.

- [BER 06] BERTOLDI P., ATANASIU B., Electricity consumption and efficiencytrends in the enlarged European Union, Report, Institute for Environment and Sustainability: JRC European Commission, 2006.
- [DAS 97] DASH P.K., SWAIN D.P., ROUTRAY A., *et al.*, “An adaptive neural network approach for the estimation of power system frequency”, *Electric Power Systems Research*, vol. 41, no. 3, pp. 203–210, 1997.
- [DAS 00] DASH P.K., MISHRA S., SALAMA M.M.A., *et al.*, “Classification of power system disturbances using a fuzzy expert system and a Fourier linear combiner”, *IEEE Transactions on Power Delivery*, vol. 2, no. 15, pp. 472–477, 2000.
- [HAG 96] HAGAN M.T., DEMUTH H.B., BEALE M., *Neural Network Design*, PWS Publishing Company, 1996.
- [HAL 09] HALBWACHS D., WIRA P., MERCKELÉ J., “Adaline-based approaches for time-varying frequency estimation in power systems”, *2nd IFAC International Conference on Intelligent Control Systems and Signal Processing (ICONS '09)*, Istanbul, Turkey, 2009.
- [LIN 05] LIN H.C., “Fast power system harmonic detection using intelligent neural network”, *International Conference on Systems and Signals (ICSS '05)*, Kaohsiung, Taiwan, 2005.
- [NGU 08] NGUYEN N.K., OULD ABDESLAM D., WIRA P., *et al.*, “Artificial neural networks for harmonics currents identification in active power filtering schemes”, *34th Annual Conference of the IEEE Industrial Electronics Society (IECON 2008)*, Orlando, FL, pp. 2696–2701, 2008.
- [NGU 09a] NGUYEN N., WIRA P., FLEILLER D., *et al.*, “Two harmonics identification schemes based on adaline neural networks for active power filtering”, *4th International Forum on Strategic Technologies (IFOST 2009)*, Ho Chi Minh City, Vietnam, pp. 324–329, 2009.
- [NGU 09b] NGUYEN N., FLEILLER D., WIRA P., *et al.*, “Neural networks for phase and symmetrical components estimation in power systems”, *35th Annual Conference of the IEEE Industrial Electronics Society (IECON '09)*, Porto, Portugal, pp. 1743–1749, 2009.
- [NGU 11] NGUYEN N., WIRA P., FLEILLER D., *et al.*, “Harmonics identification with artificial neural networks: application to active power filtering”, *International Journal of Emerging Electric Power Systems*, vol. 12, no. 4, 2011.
- [OUL 04] OULD ABDESLAM D., MERCKLÉ J., NGWANYI R., *et al.*, “Artificial neural networks for harmonic estimation in low-voltage power systems”, *4th International ICSC Symposium on Engineering of Intelligent Systems (EIS 2004)*, Island of Madeira, Portugal, 2004.
- [OUL 05a] OULD ABDESLAM D., FLEILLER D., WIRA P., *et al.*, “Adaline neural networks for online extracting the direct, inverse and homopolar voltage components from a composite voltage”, *31st Annual Conference of the IEEE Industrial Electronics Society*, Raleigh, NC, pp. 1000–1005, 2005.

- [OUL 05b] OULD ABDESLAM D., WIRA P., MERCKLÉ J., *et al.*, “A neural learning approach for time-varying frequency estimation of distorted harmonic signals in power systems”, *1st International ICSC Symposium on Industrial Application of Soft Computing*, Istanbul, Turkey, 2005.
- [OUL 05c] OULD ABDESLAM D., WIRA P., MERCKLÉ J., *et al.*, “A neural approach for the control of an active power filter”, *5th International Power Electronics Conference (IPEC '05)*, Niigata, Japan, 2005.
- [OUL 05d] OULD ABDESLAM D., MERCKLÉ J., WIRA P., “Adaline-based estimation of power harmonics”, *13th European Symposium on Artificial Neural Networks (ESANN '05)*, Bruges, Belgium, 2005.
- [OUL 07a] OULD ABDESLAM D., WIRA P., MERCKLÉ J., *et al.*, “A unified artificial neural network architecture for active power filters”, *IEEE Transactions on Industrial Electronics*, vol. 54, no. 1, pp. 61–76, 2007.
- [OUL 07b] OULD ABDESLAM D., FLIELLER D., WIRA P., *et al.*, “Distortions identification with artificial neural networks based on symmetrical components”, *IEEE International Symposium on Industrial Electronics (ISIE 2007)*, Vigo, Spain, pp. 2853–2858, 2007.
- [TEP 96] TEPPER S., DIXON J., VENEGAS G., *et al.*, “A simple frequency-independent method for calculating the reactive and harmonic current in a nonlinear load”, *IEEE Transactions on Industrial Electronics*, vol. 43, pp. 647–654, 1996.
- [WID 60] WIDROW B., HOFF M.E., “Adaptive switching circuits”, *IRE Western Electric Show and Convention Record*, Part 4, pp. 96–104, 1960.
- [WID 96] WIDROW B., WALACH E., *Adaptive Inverse Control*, Information and System Sciences Series, Prentice Hall Press, Upper Saddle River, NJ, 1996.
- [WIR 07] WIRA P., OULD ABDESLAM D., MERCKLÉ J., “A comparative study of learning and adaptive algorithms for harmonics compensation,” *IAR Annual Meeting*, Grenoble, France, 2007.

FPGA Implementation of the Adaline

In Chapter 4, the performance of the adaptive linear neuron (Adaline) for the identification of network supply parameters was examined. Now, we will show how to implement an Adaline on a field programmable gate array (FPGA) target. The parallel architecture of Adaline is suitable for implementation. A novel multiplexing technique applied on a neural harmonics extraction method is presented in this chapter. This structure can be used in nonlinear loads compensation with active power filters (APFs). The approach is composed of a neural phase-locked loop (PLL) and a neural reference current generator based on an efficient formulation of the instantaneous reactive power theory. To suppress harmonics and compensate reactive power, the whole architecture is composed of three Adaline neural networks whose structure leads to an important consumption of FPGA resources during implementation.

5.1. Introduction

Implementing complex algorithms on reprogrammable devices allows a fast time-to-market and enables easy prototyping through a hardware description language. Since artificial neural networks, in general, are inherently parallel architectures, implementing artificial neural networks on FPGA seems to be an excellent choice due to their performances for parallel processing [WON 07, OMO 06].

APFs are proposed to compensate for harmonics in existing power systems. APFs are able to correct the power factor and the harmonics without any additional equipment. The work discussed in this chapter concerns the introduction of a multiplexing technique to obtain a simpler artificial neural network based architecture for generating reference currents in the APF. The proposed technique, applied on a neural PLL and a neural reference current generator inspired from instantaneous power theory (IPT), leads to the so-called multiplexed p - q (mp - q) method. Its objective is to minimize the FPGA resource consumption during implementation.

This method uses artificial neural networks to compute the instantaneous real and imaginary powers as described in [ALA 00], thus allowing a precise selection of the harmonics and the voltage distortion. The proposed method replaces the conventional Concordia transformations (direct and inverse) and the computation of the instantaneous real and imaginary powers, with multilayer feed-forward networks. The harmonics identification itself is implemented with an Adaline neural network.

We introduce artificial neural networks in harmonic estimation methods by considering two aims [NAO 10]. First, the adaptability of artificial neural networks must lead to similar or better performances than conventional methods for varying loads. Second, the structure must be suited for hardware implementation.

5.2. Instantaneous power theory (IPT) in the APF

The principle of harmonic compensation in power systems is shown in Figure 5.1. The presence of the nonlinear load introduces harmonics distortions into the source current I_S and transforms it into a load current I_L . The APF has to identify the harmonics distortions to restore the initial form of the current.

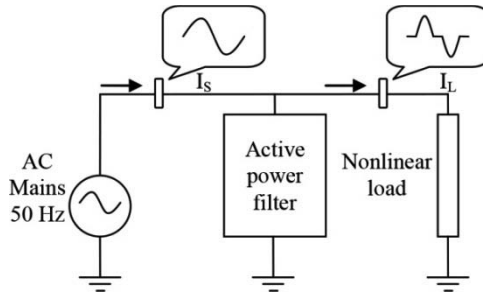


Figure 5.1. The APF's principle in a power system

Active power compensation schemes have two main parts: the first generates the reference signals and the second carries out the control signals. The identification strategy is decomposed into several blocks. At first, a PLL is introduced to allow the computation of the instantaneous real and imaginary powers, whatever the environment, condition or load. Indeed, the instantaneous real and imaginary power computation is only possible if the input of the identifier is a phase-equilibrated system where voltage waveforms are sinusoids. The next step consists of transforming the phase voltages and load currents into an α - β orthogonal coordinates system according to the direct Concordia transformation (DCT). This transformation, from a three-phase system to a two-phase system, simplifies the

mathematical expressions and reduces the computational costs. In this chapter, we focus on the implementation of the PLL bases on Adaline.

5.3. Adaline for the computing of the IPT in the PLL

Figure 5.2 shows the general principle of a reference current generation system composed of a PLL and a reference current generator.

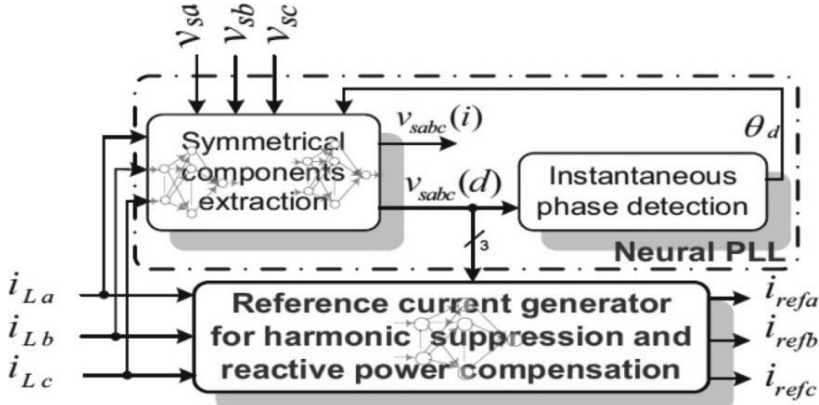


Figure 5.2. Basic principle of the whole reference current generation system

5.3.1. Adaline-based PLL

An accurate and fast detection of the utility voltage phase angle is essential to ensure the correct generation of reference signals. Moreover, the PLL used in this application has to handle voltages distorted by both harmonics and noises and therefore requires a robust, fast and efficient control algorithm. A three-phase PLL is developed for estimating the system frequency and the phase angle of the direct sequence component. This approach has been successfully used in APF schemes under highly distorted voltages.

According to the IPT, the p - q powers are calculated and their AC and DC terms are instantaneously separated. Hence, in the neural approach proposed in [OUL 07] and [NGU 09], DC terms are converted in the current reference frame, as shown in Figure 5.3, to compute the direct voltage components.

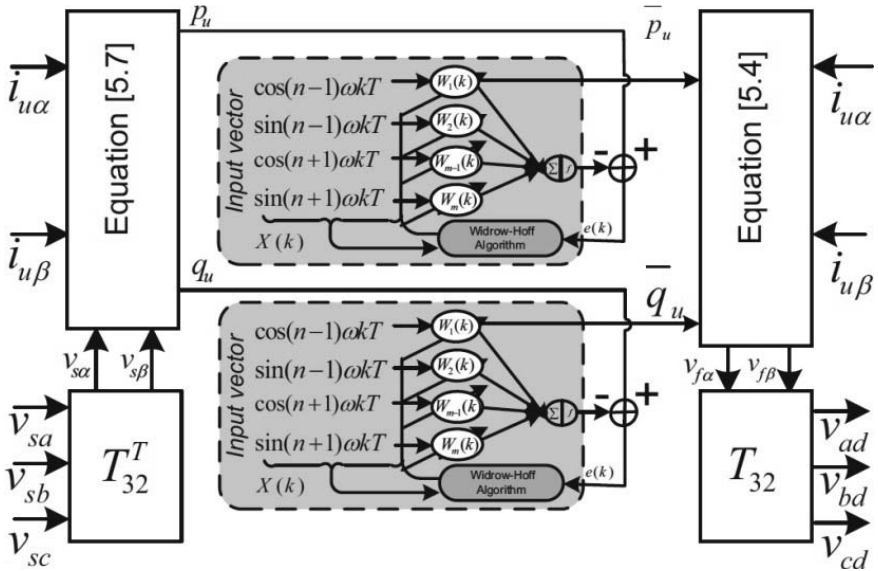


Figure 5.3. Symmetrical components extraction system

The first step in the IPT method consists of transforming the phase voltages and load currents into an $\alpha\beta$ orthogonal coordinates system according to the DCT. This transformation, from a three-phase system to a two-phase system, simplifies the mathematical expressions and reduces the computational costs:

$$\begin{bmatrix} v_0 \\ v_\alpha \\ v_\beta \end{bmatrix} = \sqrt{\frac{2}{3}} \cdot \begin{bmatrix} \frac{1}{\sqrt{2}} & \frac{1}{\sqrt{2}} & \frac{1}{\sqrt{2}} \\ 1 & \frac{1}{2} & -\frac{1}{2} \\ 0 & \frac{\sqrt{3}}{2} & -\frac{\sqrt{3}}{2} \end{bmatrix} \begin{bmatrix} v_a \\ v_b \\ v_c \end{bmatrix} \quad [5.1]$$

$$\begin{bmatrix} i_0 \\ i_\alpha \\ i_\beta \end{bmatrix} = \sqrt{\frac{2}{3}} \cdot \begin{bmatrix} \frac{1}{\sqrt{2}} & \frac{1}{\sqrt{2}} & \frac{1}{\sqrt{2}} \\ 1 & \frac{1}{2} & -\frac{1}{2} \\ 0 & \frac{\sqrt{3}}{2} & -\frac{\sqrt{3}}{2} \end{bmatrix} \begin{bmatrix} i_a \\ i_b \\ i_c \end{bmatrix} \quad [5.2]$$

The instantaneous powers are calculated from the $\alpha\beta$ -frame with:

$$\begin{bmatrix} p \\ q \end{bmatrix} = \begin{bmatrix} V_\alpha & V_\beta \\ -V_\beta & V_\alpha \end{bmatrix} \cdot \begin{bmatrix} I_\alpha \\ I_\beta \end{bmatrix} \quad [5.3]$$

The supply voltage in the $\alpha\beta$ -frame can be deduced by the general formulation:

$$\begin{bmatrix} v_{s\alpha} \\ v_{s\beta} \end{bmatrix} = \frac{1}{i_\alpha^2 + i_\beta^2} \begin{bmatrix} i_\alpha & -i_\beta \\ i_\beta & i_\alpha \end{bmatrix} \begin{bmatrix} p \\ q \end{bmatrix} \quad [5.4]$$

The fundamental direct voltage components can also be obtained from [5.4] by using unit amplitude currents of [5.5], issued from a direct fundamental system and DC terms of the associated fictitious powers:

$$\begin{bmatrix} i_{u\alpha} \\ i_{u\beta} \end{bmatrix} = \begin{bmatrix} \cos \omega t \\ \sin \omega t \end{bmatrix} \quad [5.5]$$

With [5.3], the fictitious powers ${}_u p$ and ${}_u q$ are computed from these currents and $\alpha\beta$ -space voltages related in [5.6]

$$\begin{bmatrix} v_{s\alpha} & v_{s\beta} \end{bmatrix}^T = T_{32}^T v_{sabc} \quad [5.6]$$

where T_{32}^T is the Concordia matrix.

$$p_u = v_{s\alpha} i_{u\alpha} + v_{s\beta} i_{u\beta} \quad [5.7]$$

In detail, expression [5.7] of p_u is the sum of harmonics components that can be rewritten with the linearly separable equation [5.8] so as to be approximated by an Adaline:

$$y = X^T W \quad [5.8]$$

where X and W are, respectively, the inputs and weights vectors and y is the output of the Adaline, based on a supervised learning. X is constituted from sinusoidal signals multiple of the fundamental component. At iteration k , y_k is compared to a desired value, i.e. p_u . The error $e = p_u - y$ is used by an optimal least mean square (LMS) learning algorithm, called the Widrow–Hoff algorithm, to correct Adaline weights w_k for the next sampling time toward convergence. After training, the elements w_k of W represent power amplitudes resulting from direct voltages at frequency $n\omega$ and the currents given by [5.5]. Finally, the fundamental direct

voltages $v_{sabc}(d)$ of the three-phase system are obtained by converting the first two elements of \mathbf{W} , i.e the DC parts of the instantaneous powers p_u and q_u , in the $\alpha\beta$ -voltage space with [5.4] and by multiplying them with T_{32} . The fictitious reactive power q_u is developed in the same way. The fundamental direct voltage components $v_{sabc}(d)$ can also be used by a phase detection algorithm in order to estimate the power system frequency in real time.

By applying this approach, the neural PLL is able to operate under unbalanced and distorted conditions. In addition, there is no delayed response caused by the low pass filter (LPF) and the proportional integral (PI) regulator classically used within the voltage-controlled oscillator (VCO) of the PLL. The reason for this is the association of the proposed neural symmetrical components extraction method and a fast and simple neural adaptive phase detection algorithm [FLI 09]. The reference current generation will be computed similarly to the active and reactive powers method described in the Chapter 4.

5.3.2. A multiplexing approach for hardware consumption reduction

Figure 5.4 shows three identical Adaline inside the whole reference current generation architecture. Instantaneous powers are the inputs and the estimated DC components are the outputs. To use only one Adaline with the proposed structure, one multiplexer is needed to deliver inputs by time division multiplexing to the Adaline.

Let z_k be at iteration k one of the desired instantaneous powers to be learned by the Adaline. After a training process, the neural network will estimate its value, i.e. \hat{z}_k with [5.8]. The corresponding error $e = z_k - \hat{z}_k$ should be stored in memory at address a_k . In the same time, it should be used by the learning algorithm to update for any Adaline input x_j and the weight w_{kj} . The Widrow–Hoff algorithm of expression [5.9] can be chosen as in [WID 96]:

$$\mathbf{W}_{(k+3)j} = \mathbf{W}_{kj} + \frac{\mu e_k X_j}{\lambda + X_j^T X_j}; \quad j = 1, \dots, N \quad [5.9]$$

where μ is the learning rate ($0 < \mu < 1$), λ is an appropriate constant to ensure a non-zero denominator and N is the number of Adaline inputs. A modified version of [5.9] was proposed in [OUL 07] to accelerate the training. In our work, we propose a very simple learning rule version derived from the Widrow–Hoff algorithm as follows:

$$\mathbf{W}_{(k+3)j} = \mathbf{W}_{kj} + \mu e_k X_j; \quad j = 1, \dots, N \quad [5.10]$$

By applying this learning rule on a neural harmonics detection scheme, the design is simplified for area-efficient implementation. Each weight w_{kj} obtained at iteration k and stored in memory at address b_k will then be replaced by the new one, i.e. $w_{(k+3)j}$. Finally, the estimated DC component \hat{z}_k of z_k is obtained by using the first two elements of the weight vector w_k .

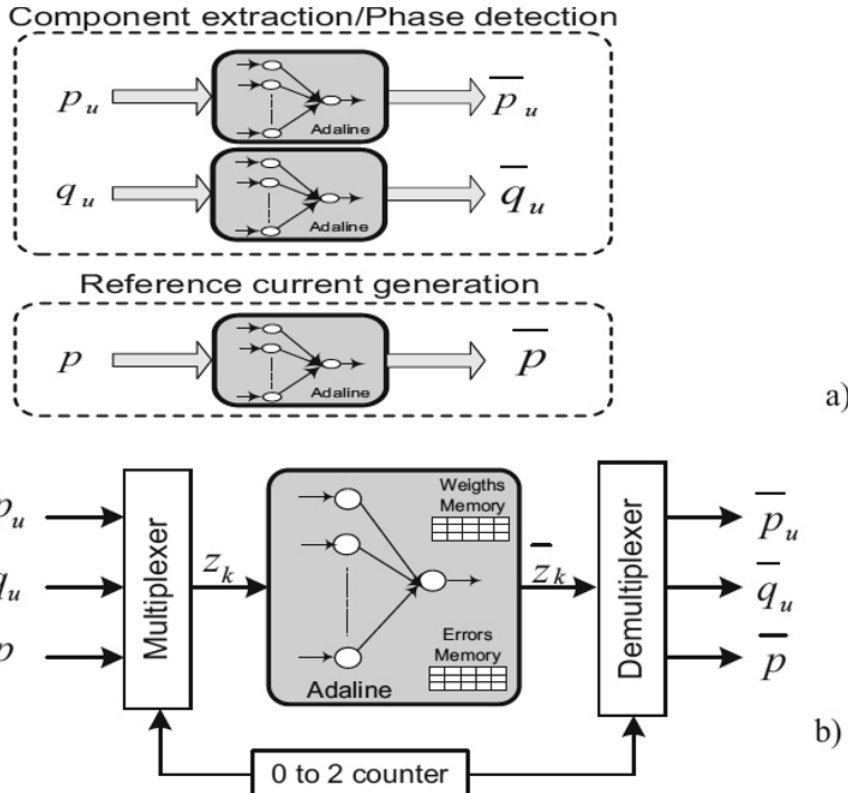


Figure 5.4. Application of the multiplexing technique on the entire reference current generation system. a) Illustration of the training process with three Adalines.
b) A multiplexing approach to use only one Adaline

Let p_u be from the symmetrical component extraction block, the instantaneous power learned at the first iteration k to obtain its DC component \bar{p}_u . \bar{q}_u , the second fictitious power generated inside the same block will be the one used at the next iteration $k + 1$ to deliver the DC component \bar{q}_u . For the iteration $k + 2$, the DC part \bar{p} will be obtained from the instantaneous active power p of the reference current generation block. The next iteration $k + 3$ will again concern the learning process for

p_u as the beginning of a new tristate cycle. To achieve this cycle, a 0–2 counter is needed to synchronize the whole process. On the other hand, a demultiplexer should be used to determine the continuous DC components of \bar{p}_u , \bar{q}_u and p_u , respectively, as shown in Figure 5.4(b).

However, doing this does not guarantee obtaining good results. It is also important to consider the time delay needed for the Adaline to estimate a desired value for any iteration. Its value should be a multiple of three, i.e. the number of desired inputs, and so the Adaline on which we are applying the multiplexing technique. For the parallel structure used on this model, the Adaline needs two delays to generate an output value. To obtain a time delay of three, we added a delay block for any Adaline input and then obtain the expected results.

Figure 5.5 shows how estimation errors and weights are dispatched inside FPGA-embedded memories. For any iteration, error e_k and weight w_{kj} , which correspond to the training of an instantaneous power z_k , are written inside a memory. The estimated DC value \bar{z}_k will be generated three periods later at the Adaline output. The demultiplexer will then allow us to obtain each DC power component continuous signal. As a result, DC power iteration is three times slower. So, to avoid degradations on the results, the learning rate parameter of the Adaline is modified.

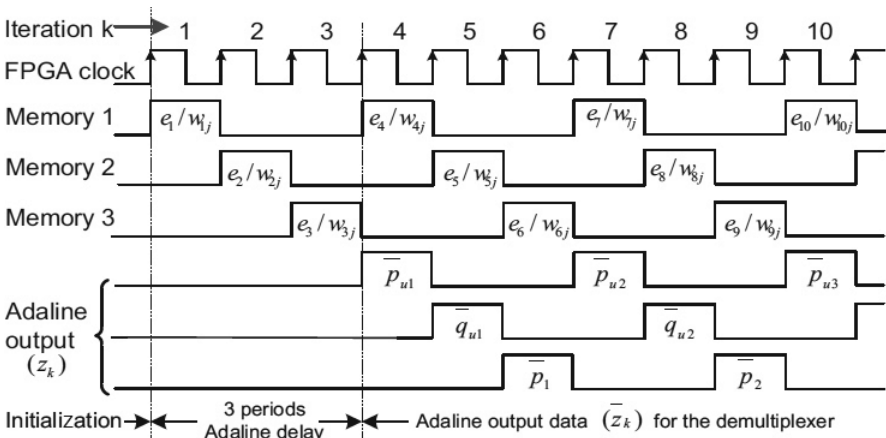


Figure 5.5. Data flow inside memories and at the Adaline output when applying the mp-q method

5.4. Results

5.4.1. Simulation

Neural reference currents generation associated with a three-phase neural approach for symmetrical components estimation was developed in Altera Dsp Builder™. The instantaneous phase estimation block was added to deal with changing parameter in power grid by obtaining real-time reference currents. To evaluate compensation performances, the whole model was connected to a control block based on a bandless hysteresis approach [RAD 09]. This allows us to generate phase-opposite the three-phase reference current on the grid to suppress harmonic and compensate reactive power. In general, simulation results obtained with the proposed $mp-q$ method were similar to those obtained from the presented neural $p-q$ method.

Figure 5.6(a) shows simulation results under the 20% unbalanced source voltage. The distorted load current is shown in Figure 5.6(b).The corresponding fundamental component after harmonics extraction is shown in Figure 5.6(c), whereas the source current after compensation is shown in Figure 5.6(d). This current reveals a total harmonic distortion (THD) of 1.92% for a sampling time of 10 μ s.

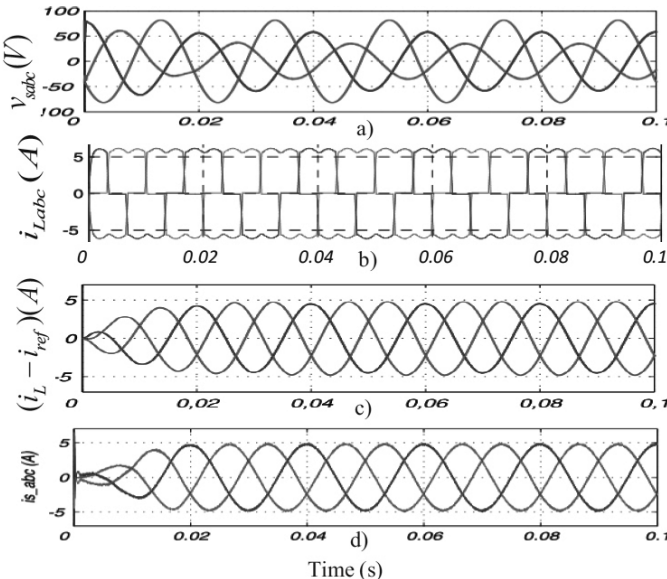


Figure 5.6. Results under unbalanced and sinusoidal voltage source with balanced load.
 a) Unbalanced source voltage, b) three-phase distorted load current, c) fundamental component obtained after harmonics extraction and d) source current after compensation

5.4.2. FPGA implementation results

For this step, an Altera Stratix II development kit is used with onboard 100 MHz oscillator, as a rapid prototyping system. This system is shown in Figure 5.7 where an auxiliary card is used to acquire low-frequency analog inputs and eventually generates pulse width modulation (PWM) signals to control the inverter of the APF power circuit. To evaluate the feasibility of FPGA implementation of the mp - q method in real experimental conditions, we used a source voltage and load current measured on a real APF test bench. The results obtained are shown in Figure 5.8. First, the unbalanced source voltage is shown in Figure 5.8(a). Next, the distorted load current waveforms are also shown in Figure 5.8(b) with a THD of 22%. By loading the inherent values on a Matlab workspace before the FPGA implementation of the design, we obtain the fundamental component in Figure 5.8(c) with a THD of approximately 0.6%. This identification result shows that harmonics are well detected and their separation from the load current leads to a sinusoidal waveform of the fundamental component. These results confirm that the mp - q method gives results very close to those obtained with the neural p - q formulation.

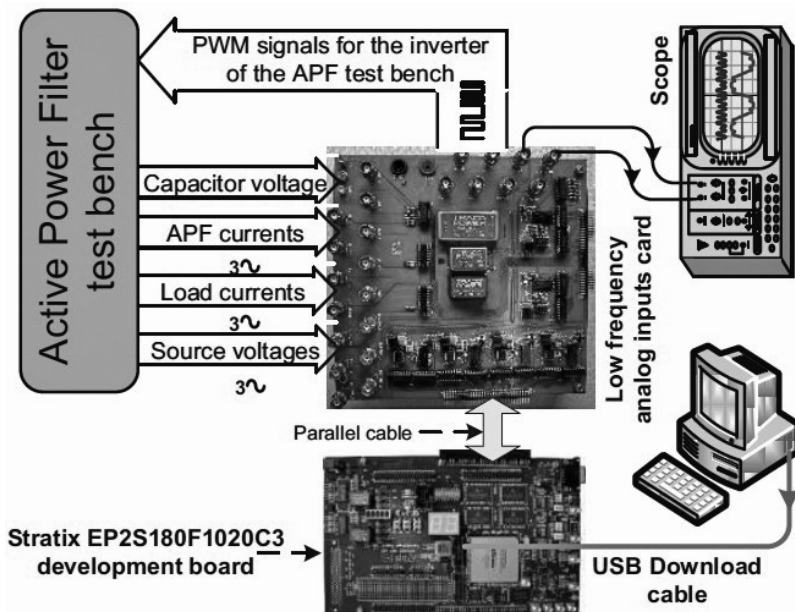


Figure 5.7. Principle of the prototyping system

However, hardware implementation requirement of the neural reference currents generation system by means of the mp - q method has been evaluated and compared

to that of the p - q method. As presented in Table 5.1, the comparisons have been extended to the *tri-monophase* and *improved tri-monophase* (ITM) methods discussed in [DZO 09]. From there, the average resource consumption of the prototyping target, i.e. the FPGA Stratix EP2S180F1020C3, is only 23.9% for the mp - q method compared to 26.2% for the p - q method. In any way, an effective comparison has only to take into account particular resources used for calculations. We can mention embedded 9 bit DSP blocks used to implement multipliers and arithmetic look-up tables (ALUTs), the basic cell used in the Quartus® II software for logic synthesis.

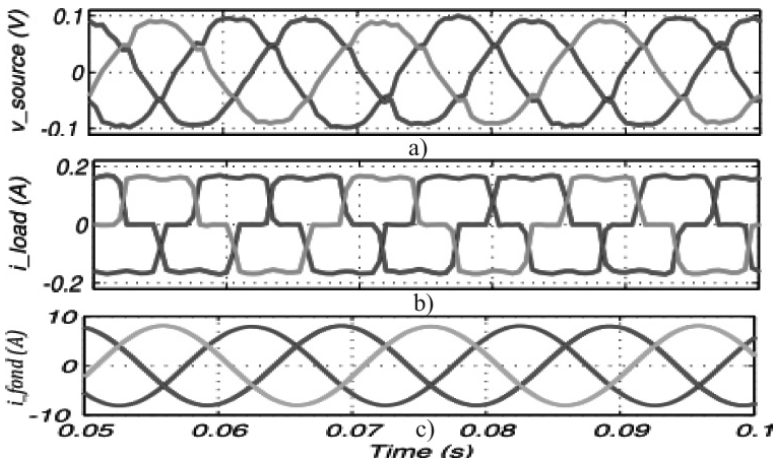


Figure 5.8. Harmonics separation from experimental measurement of distorted current:
a) source voltage, b) load current and c) fundamental component
obtained after harmonics separation

Resources	Available	FPGA resources consumption in %			
		Tri-monophase	ITM	P-Q	MP-Q
ALUT	143,520	92.8	32	37	17
Register blocks	147,818	4.75	2.6	2.25	0.50
Memory (RAM)	9,383,040	24	24	0	8
Pins	783	11	11	11	11
9-bits DSP	768	100	100	99	99
PLL	12	8	8	8	8
Total consumption		N/A	29.6	26.2	23.9

Table 5.1. Evaluation of resource consumption for the p - q and mp - q methods

In this way, because all the DSP blocks are used in both cases, the remaining calculation blocks are implemented using ALUTs blocks. As we can see, only 24,398 blocks, i.e. 17% of the ALUT blocks, are used while implementing the mp - q method for 53,102 blocks, i.e. 37% of the same blocks for the p - q method. This result shows that by multiplexing the Adalines, the technique allows us to reduce ALUT blocks by 54% without any degradation on harmonics detection performances. Furthermore, if the objectives were only to suppress harmonics instead of compensating for the reactive power, the system would have been composed of four similar Adalines. In this case, applying the multiplexing technique on the system would have implied better results in terms of FPGA resource reduction. In fact, 48% of available ALUTs would have been used instead of 37% for the p - q technique leading to a reduction rate of 64%, i.e. an economy of 44,491 blocks by means of the mp - q technique.

On the other hand, an attempt to implement the compensation system by means of the *tri-monophase method* failed because the design was unable to fit into the device. For this purpose, the Quartus® II Fitter requires 12,275 logics array blocks (LABs), but the FPGA contains only 8,970 LABs. In a Stratix II, a LAB consists of eight adaptive logic modules (ALMs) and an ALM contains two ALUTs. Hence, by applying a similar optimization technique on this method, the designs can fit into the hardware target and the consequent ITM method uses only 29.6% of the available resources.

5.5. Conclusion

In an attempt to minimize the consumption of FPGA resources during the implementation of neural harmonics extraction algorithms, a multiplexing technique has been applied to reduce the number of Adalines. The compensation strategy consists of extracting harmonics and obtaining a unity power factor. For this purpose, three Adalines are used to build an adaptive system, whose performance is known underbalanced and unbalanced source voltage. The presented system is made up of a neural PLL for the extraction of phase and symmetrical components and a generator of neural reference currents. For such a system based on the IPT, the major part of resources used during implementation is due to the structure and the number of Adalines. Thus, the optimization approach, called the mp - q method, derived from a recent neural p - q formulation, leads to a simpler system based on a unique Adaline. In particular, the proposed multiplexing technique allows us to reduce the ALUT blocks of the FPGA StratixII by 64% for harmonics compensation. Furthermore, these architectural modifications do not change the performance of the system.

5.6. Bibliography

- [ALA 00] ALALI M.A.E., SAADATE S., CHAPUIS Y.A., *et al.*, “Control and analysis of series and shunt active filters with SABER”, *International Power Electronics Conference (IPEC '2000)*, Tokyo, Japan, 2000.
- [DZO 09] DZONDE S.R.N., BERVILLER H., BLONDE J.-P., *et al.*, “FPGA implementation of harmonic currents detection methods using neural networks”, *Proceedings of the 13th European Conference on Power Electronics and Applications (EPE '09)*, CDROM, Barcelona, Spain, 8–10 September 2009.
- [FLI 09] FLIELLER D., OULD ABDESLAM D., WIRA P., *et al.*, “Distortions identification and compensation based on artificial neural networks using symmetrical components of the voltages and the currents”, *Electric Power Systems Research*, vol. 79, no. 7, pp. 1145–1154, 2009.
- [NAO 10] NAOUSSI S., NGUYEN N.K., BERVILLER H., *et al.*, “FPGA resources reduction with multiplexing technique for implementation of ANN-based harmonics extraction by mp-q method”, *36th Annual Conference of the IEEE Industrial Electronics Society (IECON '10)*, Glendale, AZ, pp. 2043–2048, 2010.
- [NGU 09] NGUYEN N., FLIELLER D., WIRA P., *et al.*, “Neural networks for phase and symmetrical components estimation in power systems,” *35th Annual Conference of the IEEE Industrial Electronics Society (IECON '09)*, Porto, Portugal, pp. 1743–1749, 2009.
- [OMO 06] OMONDI A.R., RAJAPAKSE J.C., *FPGA Implementations of Neural Networks*, Springer, 2006.
- [OUL 07] OULD ABDESLAM D., WIRA P., MERCKLÉ J., *et al.*, “A unified artificial neural network architecture for active power filters”, *IEEE Transactions on Industrial Electronics*, vol. 54, no. 1, pp. 61–76, 2007.
- [RAD 09] RADZI M.A.M., RAHIM N.A., “Neural network and bandless hysteresis approach to control switched capacitor active power filter for reduction of harmonics”, *IEEE Transactions on Industrial Electronics*, vol. 56, no. 5, pp. 1477–1484, May 2009.
- [WID 96] WIDROW B., WALACH E., *Adaptive Inverse Control*, Information and System Sciences Series, Prentice Hall Press, Upper Saddle River, NJ, 1996.
- [WON 07] WON E., “A hardware implementation of artificial neural networks using field programmable gate arrays”, *Nuclear Instruments and Methods in Physics Research A*, vol. 581, pp. 816–820, 2007.

Index

A, C

active power filtering, 101, 118, 121
Adaline, 90–91
artificial neural networks, 62, 87, 121, 122
complexity measure, 21, 22, 52, 54–55, 61, 72
computational cost reduction, 123, 124
current harmonics, 87, 88, 117, 118

E, F, G

energy concentration, 21, 41–51,
feature extraction, 27, 36, 80, 83, 90
FPGA target, 121
frequency representation, 2, 6–12, 15–18, 43
Gaussian windows, 69

H, I

hardware implementation, 102, 103, 122, 130
harmonic estimation, 90, 122
instantaneous power theory, 121–123

M, N, P

multiplexing technique, 121, 127, 128, 132
murmur detection, 80–82
non-stationarity, 4–5
phase lock-loop, 94
power quality, 2, 87, 88–89, 115

S, T

Shannon energy, 61
signal processing, 12, 25, 29, 61–64, 87, 90
SSE method, 66, 67, 73, 74, 77
ST-spectrogram, 51–55, 72, 73, 80–82
stationarity, 2–4
Stockwell transforms, 18, 21, 29–55
time representation, 38, 43

U, V, W

unbalance, 89–90
uncertainty principle, 12–15
wavelet transform, 21
Wigner-Ville transform, 22
windows width optimization, 68